

***Proceeding Book of
First Conference for Engineering
Sciences and Technology (CEST-2018)
(Part 2)***

Electrical and Electronics Engineering

25-27 September 2018

Garaboulli - Libya

Table of Contents

Micro Gas Turbine Simulation And Control	141
Optimal Power Loss Minimization using Optimal Size and Location of Shunt Capacitors, and DG	156
Experimental Investigation on the Performance Evaluation of Solar Tracking Photovoltaic System	163
Comparative Analysis of Electric Field and Potential Distributions over Porcelain and Glass Insulators Using Finite Element Method	173
Long Term Peak Load Forecasting for the Libyan Network	182
THD Investigation of Hybrid Cascaded Multilevel Inverter.....	191
Impact of Wind Generation Location on Power System Losses.....	200
Antenna Elevation Control using Multiple Switched Self-Tuning Controllers Design	207
Control of a Three-phase Off-Grid Inverter for Photovoltaic Systems Applications	218
Excimer Laser Processing of IGZO Thin Films for Transparent TFTs.....	228
Loss of Load Expectation of Alkhoms Generating Units	238

Micro Gas Turbine Simulation And Control

Ibrahim Ahmed El-Sharif¹, Mahmoud Mansour El- Fandi²

¹Ssssharif2004@yahoo.com ,²M_elfandi@hotmail.com

¹Instrument department, General electrical company of Libya, GECOL, Khoms, Libya

²Electricalandelectronicengineer, Facultyofengineering, Tripoli-university, Tripoli, Libya

ABSTRACT

Gas turbines are widely used in power generation plants due to their compactness, fast start-stop sequences, and their applications, and...etc. A split shaft micro-turbine mechanical model is used. Three main controllers for three different loops have been designed and discussed. MATLAB/Simulink environment is used to represent the mechanical model for Micro-turbine spilt shaft. A speed PID controller, exhaust temperature PI controller, and mechanical & electrical power PID controller all have been designed with MATLAB/Simulink. Compensators have also been used instead of PI and PID controllers which had been used for three systems. A comparison between PI, PID controllers, and its corresponding compensator have been done through this research. At last a supervisory controller for three systems has been done. A MIMO system - Multi-Input Multi-Output - will be reduced to a SISO system - Single-Input Single-Output - during system design.

Keyword— MGT: Micro-Gas turbine, LVG: Least Value Gate, MIMO: Multi Input Multi Output

1. Introduction

Single-shaft MGT models are designed to operate at high speeds (some in excess of 100,000 revolutions per minute [RPM]) and generate electric power as high-frequency alternating current (AC). The generator output is rectified to direct current (DC) and then inverted to 60 hertz (Hz) AC for commercial use in the United States, or 50 Hz for use in countries with a 50 Hz supply. Two-shaft MGT micro-gas turbines have a turbine-driven compressor on one shaft and a separated “free” power turbine on a second shaft to power the generator. (In conventional gas turbines, this arrangement is generally used in mechanical drive service, as the free power turbine, generally via a gear box, then runs other turbo-machinery, such as compressors or pumps.) With the expansion pressure ratio split between two turbines, the power turbine on a two-shaft machine can be designed to run at lower speed with high efficiency. Split-shaft design uses a power turbine rotating at 3000 rpm and a conventional generator connected via a gearbox for speed multiplication [1]. The figure (1) illustrate a split-shaft micro-turbine as was have been chosen in this paper which consists of two main turbines one for compressor driving and the other for driving conventional generator which connected with a gearbox [2].

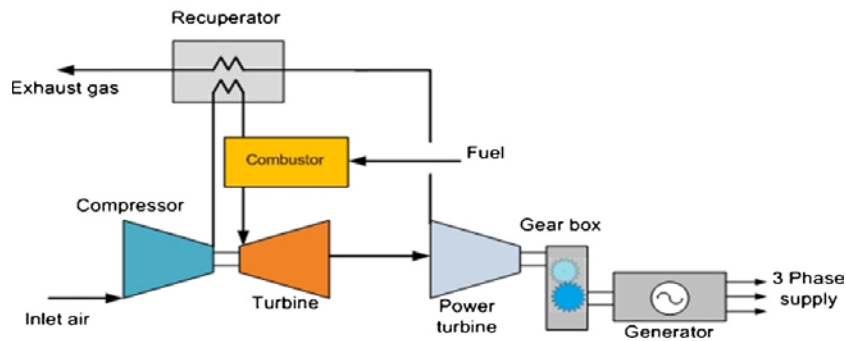


Figure1: Two-shaft MGT via a gearbox to generator

2. MIMO MGT Model with PID controller:

There are a large literature on the modelling of gas turbines, with varying level of complexity depending on the intended application. The concept of gas turbine system presented in this section is based on the paper presented by Rowen [3]. He proposed a single-shaft design, generator driven gas turbine model which includes speed control, temperature control and fuel system. This model was successfully adopted by the several authors for gas turbine simulations as well as for micro-turbine simulations with smaller time constants [4]. The three control functions of the micro-turbine are: speed control acting under part load conditions, temperature control acting as an upper output power limit, and acceleration control to prevent over speeding. The output of these control function blocks with (P_c) mechanical power control are all inserted to a least value gate (LVG), whose output is the lowest of the four inputs and results in the least amount of fuel to the compressor-turbine as shown in figure (2). This figure shows the per-unit presentation of a micro-turbine, along with its control systems [4]. Each subsystem of the micro-turbine is discussed in the following subsections.

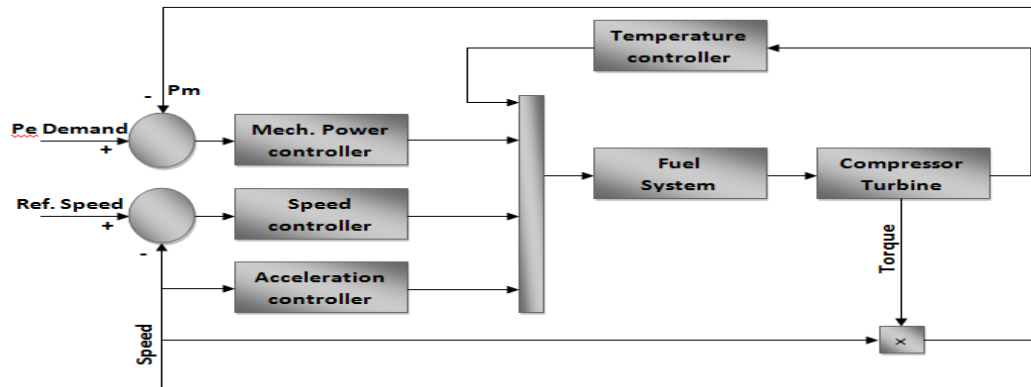


Figure 2: Micro-turbine system and its controllers

3. Speed and acceleration loop controllers.

The speed control operates on the speed error formed between a reference (one per-unit) speed and the MTG system rotor speed. It is the primary means of control for the micro-turbine under part load conditions. Speed control is usually modelled by using a lead-lag transfer function, or by a PID

controller [4]. A PID controller has been used to present the speed controller, as shown in figure (3). In this figure the PID controller which has been used is maintained by changing the P,I and D parameters of the controller to reach the acceptable response on output using trial and error method as will discuss later. Acceleration control is used primarily during turbine start-up to limit the rate of the rotor acceleration prior to reaching operating speed. If the operating speed of the system is close to its rated speed, the acceleration control could be eliminated in the modelling, which is the case in this study.

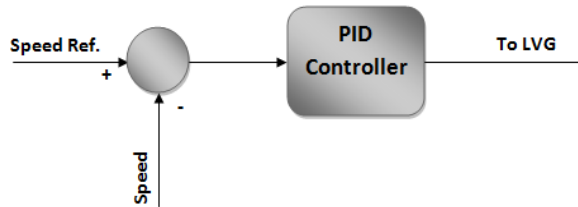


Figure 3: PID speed controller

4. Fuel system.

The fuel system consists of the fuel valve and actuator. The fuel flow comes out from the fuel system results from the inertia of the fuel system actuator and the valve positioner [3]

The valve positioner transfer function is:

$$E_1 = \frac{K_{vv}}{T_v s + c} F_d \quad (1)$$

and the fuel system actuator transfer function is:

$$W_f = \frac{K_f}{T_f s + c} E_1 \quad (2)$$

In equation (1) and (2), K_{vv} and (K_f) is the valve positioner (fuel system actuator) gain, T_v , T_f are the valve positioner and fuel system actuator time constants, c is a constant, F_d and E_1 are the input and outputs of the valve positioner and W_f is the fuel demand signal in p.u. The output of the LVG, V_{ce} , represents the least amount of fuel needed for that particular operating point and is an input to the fuel system. Another input to the fuel system is the per-unit turbine speed N (limited by the acceleration control). The per-unit value for V_{ce} corresponds directly to the per-unit value of the mechanical power on turbine at steady-state. The fuel flow control as a function of V_{ce} is shown below in figure (4).

The value of V_{ce} is scaled by the gain $K_3(K_3 = (1 - K_6))$, then delayed and offset by the minimum amount of fuel flow K_6 to ensure continuous combustion process in the combustion chamber. K_6 is essentially the minimum amount of fuel flow at no-load, rated speed [4].

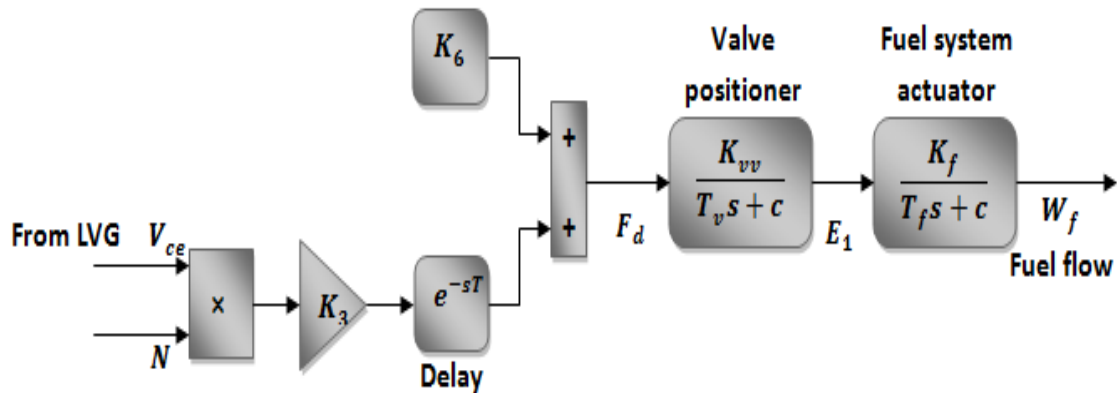


Figure 4: Block diagram of the fuel system

5. Compressor-Turbine system.

The compressor-turbine is the heart of the micro-turbine and is essentially a linear, non-dynamic device (with the exception of the rotor time constant) [4]. There is a small transport delay T_{CR} , associated with the combustion reaction time, a time lag T_{CD} , associated with the compressor discharge volume and a transport delay T_{TD} , for transport of gas from the combustion system through the turbine. The block diagram of the compressor-turbine package is shown in figure (5). In this figure both the torque and the exhaust temperature characteristics of the gas turbine are essentially linear with respect to fuel flow and turbine speed and are given by the following equations [4]:

$$\text{Torque} = K_{HHV}(W_{f_2} - 0.23) + 0.5(1 - N)(Nm) \quad (3)$$

$$\text{Ext. } T_x = T_R - 700(1 - W_{f_1}) + 550(1 - N) \text{ (}^\circ\text{F)} \quad (4)$$

where K_{HHV} is a coefficient which depends on the enthalpy or higher heating value of the gas stream in the combustion chamber and T_R is the reference temperature. The K_{HHV} and the constant 0.23 in the torque expression cater for the typical power/fuel rate characteristic, which rises linearly from zero power at 23% fuel rate to the rated output at

100% fuel rate. The input to this subsystem is the p.u. fuel demand signal W_f and outputs are the p.u. turbine torque (N.M) which multiplied by the rotor speed to result the mechanical power and exhaust temperature ($^\circ\text{F}$). Both mechanical power and temperature signals are controlled and inserted again into the LVG.

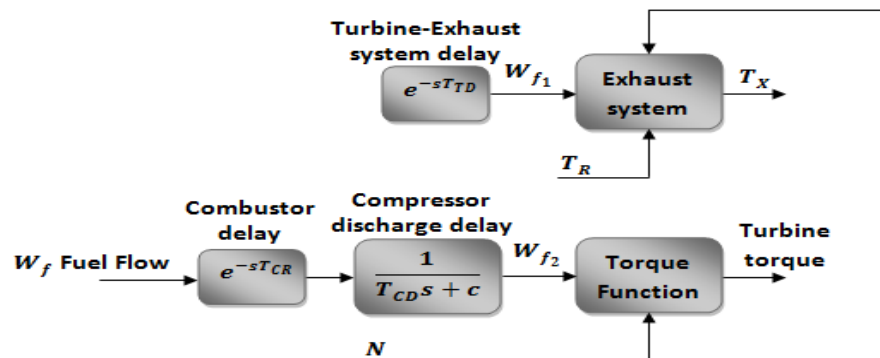


Figure 5: Compressor-Turbine package of MGT

6. Temperature loop and PI controller.

Temperature control is the normal means of limiting the gas turbine output power at a predetermined firing temperature, independent of variation in ambient temperature or fuel characteristics. The fuel burned in the combustor results in turbine torque and in exhaust gas temperature. The exhaust temperature is measured using a series of thermocouples incorporating radiation shields as shown in the block diagram of the temperature controller Figure (6). In this figure, T_t is the temperature controller integration rate and T_3 , T_4 are time constants associated with the radiation shield and thermocouple, respectively. K_4 and K_5 are constants associated with radiation shield and T_5 is the time constant associated with temperature controller. The output from the thermocouple is compared with a reference temperature, which is normally higher than the thermocouple output. This forces the output of the temperature control to stay on the maximum limit permitting the dominance of speed control through the LVG figure (3). When the thermocouple output exceeds the reference temperature, the difference becomes negative, and the temperature control output starts decreasing. When this signal Figure (3) becomes lower than the speed controller output, the former value will pass through the LVG to limit the turbine's output, and the turbine operates on temperature control. The input to the temperature controller is the exhaust temperature T_x and the output is the temperature control signal to the LVG [4].

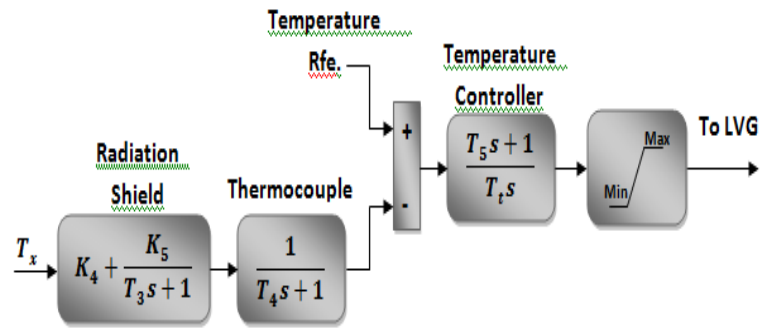


Figure6: Block diagram of temperature control system

7. The generator.

A conventional generator has been used in this study because of low speed generator to avoid the interface circuits (power electronic circuit) which used as have been said before in case of high speed generator, and also conventional generator is useful and suitable in countries where 50 Hz is mainly used. The electrical generator was modelled based on a generator swing differential equation. The swing differential equation is ascertained in terms of power [5].

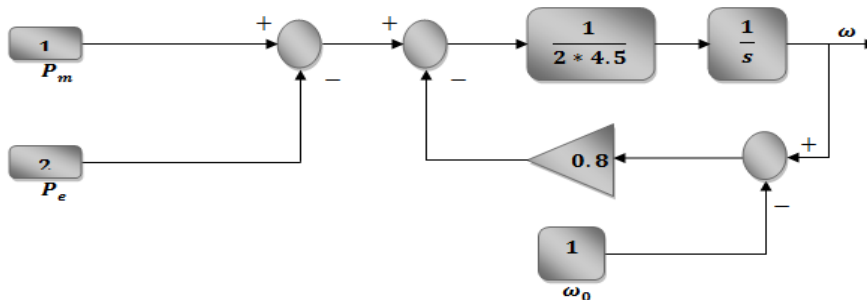


Figure7: Conventional generator

$$\frac{d\omega}{dt} = \frac{\omega_0}{2H_{eq}} [P_m - P_e - D_{eq}(\omega - \omega_0)] \quad (5)$$

Generator equation was modelled based on the assumption that losses, due to the shaft rotation are ignored [5]. The SIMULINK model representation of the electrical generator is shown in figure (7).

The input as has been illustrated in figure (7) are the Mechanical power (P_m) and Electrical power (P_e) and the output was the rotor speed ω of the generator which has been inserted into the turbine as a feedback.

8. MGT loops, PID tuning, and simulation tests.

A step function has been applied as input of electrical power as set point (from zero to 0.2) p.u (Per Unit). The reference rotor speed was 1 p.u. in all simulation. The reference exhaust temperature also fixed at 950 °F. The output response results after parameters of PID maintained using trial & error method and Ziegler-Nichols method were applied. The figure (8) shows the output response of electrical power demand (P_e) and mechanical power (P_m) outputs after applying the Ziegler-Nichols method on PID controller of P_e & P_m . The parameters in figure (8) were as following :

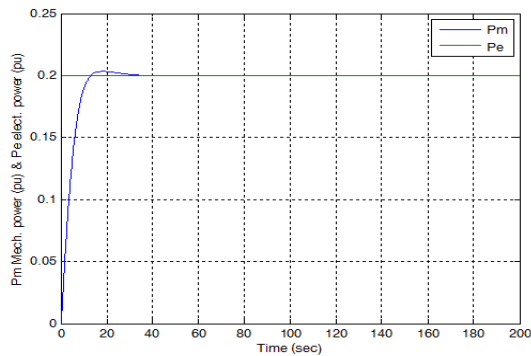


Figure 8: Relationship between P_e & P_m with Ziegler-Nichols method
 $T_u = 0.5$, $K_c = 12$, $K_p = 0.2 \cdot 12$, $K_i = 0.5/2 = 0.25$ and $K_d = 0.5/8 = 0.0625$

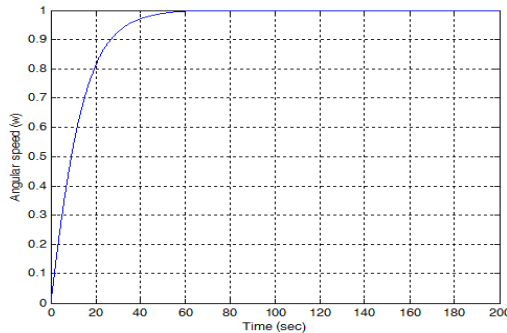


Figure 9: Speed (ω) with Trial & error method.

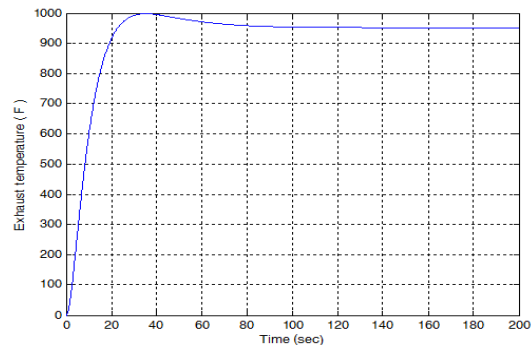


Figure 10: Exhaust temperature ($^{\circ}$ F)

Ziegler-Nichols method was applied and found suitable parameter for mechanical power PID controller, whereas could not be applied with Angular speed PID controller and also in temperature PI controller. Trial & error method is the perfect method for both angular speed PID controller and temperature PI controller . Figure (9) shows the response of Angular speed PID controller using Trial & Error method. Angular speed ω (pu) PID controller using Trial & error method. PID parameter of: $K_p=1, K_i=21$ and $K_d=0.5$ $N=2$

Exhaust temperature is illustrated in figure (10) with parameter of PI controller using Trial & Error where : $P= 1$ and $I= 2$. Figure (11) illustrate the main structure of Micro-turbine using MATLAB/Simulink, power demand (P_e), feedback of angular speed (ω), and (TR) exhaust temperature set-point. All are represent the inputs of the Micro-turbine itself. The output of the

Micro-turbine obviously are the mechanical power (P_m), rotor speed (ω), and measured exhaust temperature.

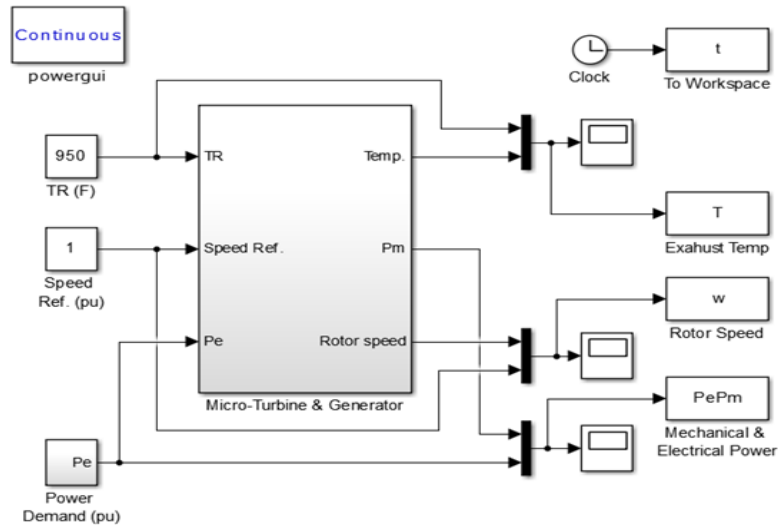


Figure 11: Main structure of MGT on MATLAB/Simulink

9. Identification and model reduction of MIMO MGT with PID controller.

• Mechanical & electrical power loop.

Estimation and validation of the output signal could be represented for mechanical power PID controller, angular speed PID as well and also for PI controller exhaust temperature by do several calculations the transfer function of speed loop with PID controller was as follows.

$$G_{T1} = \frac{0.08}{s^2 + 0.45s + 0.08} \quad (10)$$

To validate the response of mechanical power PID controller, figure (12) shows the actual and estimated values of that. With the same step input of both and we could obviously compare the two values to each other. The blue curve for (P_m) actual value and the red curve for (P_m) estimated value were approximately the same:

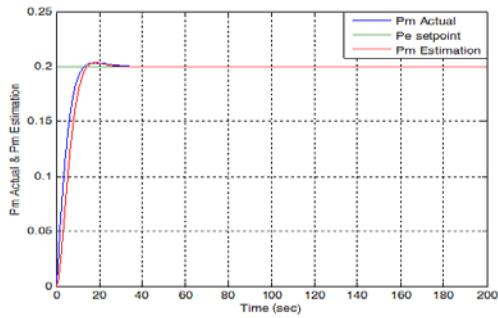


Figure 12: Actual and estimation values of mech. power response.

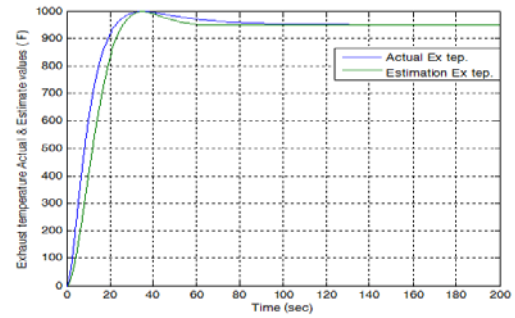


Figure13: Actual and estimation values of Exh.Tem.(°F)response.

- **Exhaust temperature loop.**

In the same way exhaust temperature has been estimated and validated $y_{max} = 995.3$, $y_{ss} = 950$ $t_p = 35$ sec. After several calculations has been done as above a results found were $\zeta = 0.696$ $\omega_n^2 = 0.0156$. The transfer function of G_{T2} will be as follows:

$$G_{T2} = \frac{0.0156}{s^2 + 0.174s + 0.0156} \quad (11)$$

Figure (13) illustrate the actual (blue curve) and estimation values (green curve) of Exhaust temperature. As we can see the output response of the actual and the estimation value are approximately the same.

- **Rotor speed loop.**

By getting values of $y = 0.6318$, $y_{ss} = 1$ $\tau = 12.56$ sec from the rotor speed PID controller and substituting these values in the following first order transfer function equation which represent the rotor speed as follows:

$$G_{T3} = \frac{1}{12.56s + 1} \quad (12)$$

The figure (14) shows the actual and estimated values of rotor speed (ω) pu output response and as we could see are the same.

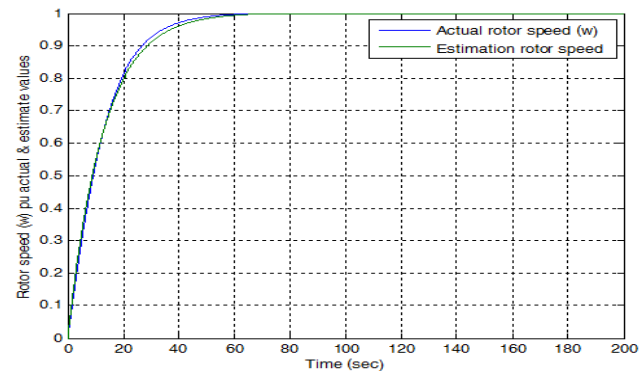


Figure14: Actual & estimated values of rotor speed(ω)output response

10. Compensators design instead of PID and PI controllers.

The design of feedback control system in industry is probably accomplished using frequency-domain more often than other method. The primary reason for the popularity of frequency-domain design is that the effects of disturbances, sensor noise, and plant uncertainties are relatively easy to visualize

and assess in the frequency domain [6]. In this section PID controller in power and speed controller, also temperature PI controller will be replaced with lag compensator.

- **Lag Compensation For MGT Speed Controller**

Mathematical model of speed controller PID for the micro-turbine which we have been discussed in chapter four, as follows :

$$P + I \left(\frac{1}{s} \right) + D \left(\frac{N}{1 + N \left(\frac{1}{s} \right)} \right) \quad (13)$$

By getting the values of P, I, D, and N from MATLAB/Simulink speed PID controller shown in figure (10) the equation (14) will be as follow:

$$PID_{(speed)} = 1 + 2 \left(\frac{1}{s} \right) + \frac{1}{2} \left(\frac{2}{1 + \frac{2}{s}} \right)$$

$$PID_{(speed)} = \frac{4 \left(\frac{1}{4}s + 1 \right) (s + 1)}{s \left(\frac{1}{2}s + 1 \right)} \quad (14)$$

By rearrange the equation to show the crossover frequencies of speed PID controller:

To replace $PID_{(speed)}$ by a appropriate compensator we must use Bode plot of speed PID controller which could be seen in the figure (15):

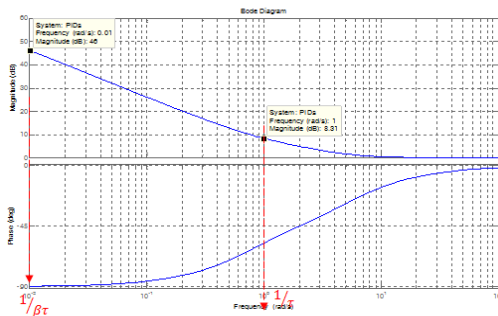


Figure 15: Bode plot speed PID controller.

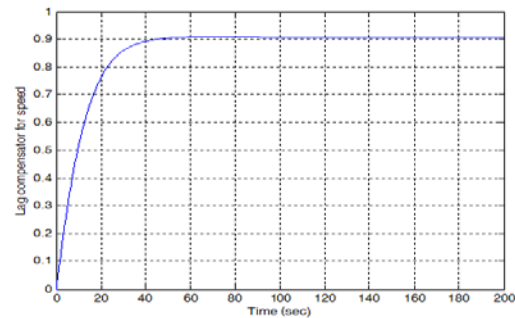


Figure 16: Lag compensator response for speed loop.

As we could see the $PID_{(speed)}$ shape looks like a lag compensator with upper and lower gain crossover frequencies $\left(\frac{1}{\beta\tau} \right)$ and $\left(\frac{1}{\tau} \right)$ respectively:

$$D(s) = \frac{\tau s + 1}{\beta \tau s + 1}$$

$$= \frac{s + 1}{100s + 1} \quad (15)$$

as we could see the speed lag compensator response shown in figure (16) corresponding to equation (15) is acceptable except the gain which need to be increased. After increasing the lag compensator gain, equation (15) will be as follows and speed lag compensator response is then shown in figure

(17). Bode plot of both PID speed controller and Lag compensator shown in figure (17) illustrate that the gain crossover frequency are nearly the same (lower is 0.01 rad/sec and the upper is 0.1 rad/sec).

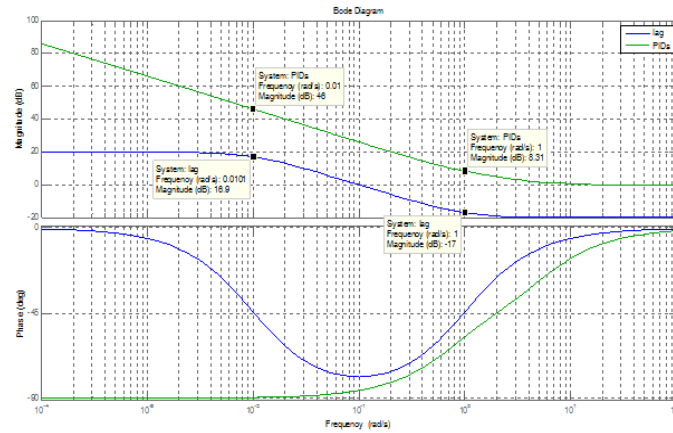


Figure 17: Bode plot of lag compensator and PID for speed.

$$D(s) = \frac{10s + 10}{100s + 1} \quad (16)$$

• **Lag Compensation For MGT Mechanical Power:**

As we have been done in PID speed controller a lag compensator for mechanical power is shown in figure (18)

$$D(s) = \frac{\tau s + 1}{\beta \tau s + 1} = \frac{10s + 1}{100s + 1} \quad (17)$$

As we could see the mechanical power lag compensator response shown in figure (18) corresponding to equation (17) is acceptable except the gain which need to be increased. After increasing the lag compensator gain, equation (17) will be as follows and mechanical power lag compensator response is then shown in figure (19):

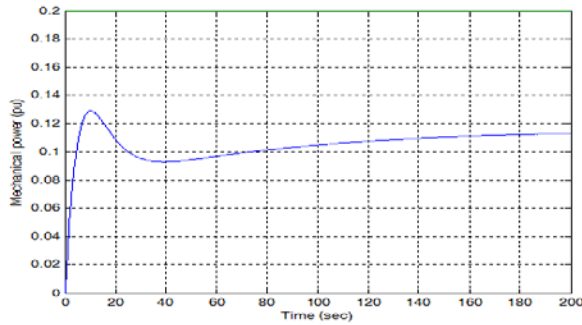


Figure 18: Lag compensator response for Mech. power

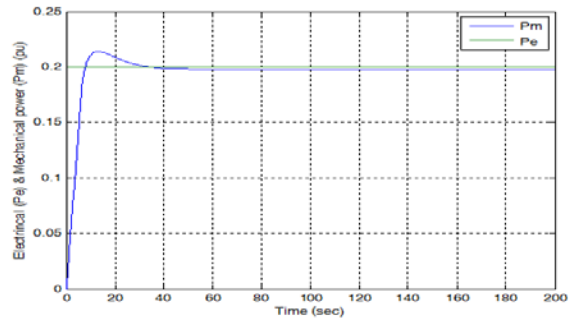


Figure 19: Lag compensator response for mech. power

after

maintaining

$$D(s) = \frac{600s + 60}{100s + 1} \quad (18)$$

Figure (20) shows the comparison between Bode plot of the both mechanical power PID and mechanical power lag compensator which we have been gotten according to eq. (18). Bode plot of both PID mechanical power controller and Lag compensator shown in figure (20) illustrate that the gain crossover frequency are nearly the same (lower is 0.001 rad/sec and the upper is 0.1 rad/sec).

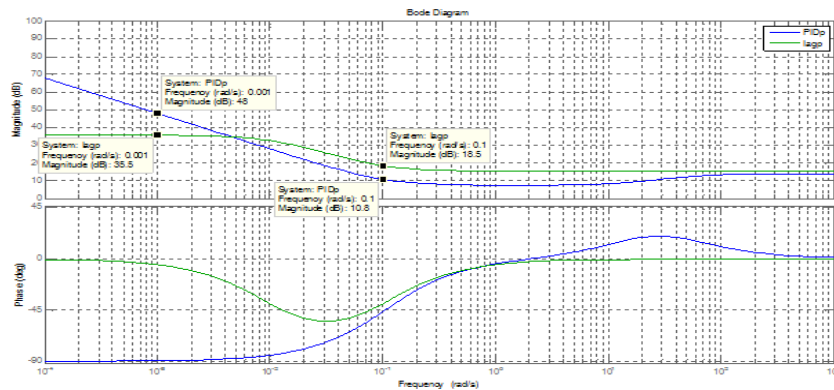


Figure 20: Lag compensator response for Mech. Power

• **Lag compensation for MGT temperature controller:**

The mathematical model of Exhaust temperature PI controller for the micro-turbine which we have been discussed in section 9, as follows :

$$P + I \left(\frac{1}{s} \right) \quad (19)$$

By getting the values of (P) and (I) from MATLAB/Simulink Exhaust temperature PI controller shown in figure (11) the equation (19) will be as follow:

$$PI_{(Tem)} = 1 + 2 \left(\frac{1}{s} \right)$$

After getting the upper and lower gain cross over frequencies of the PI exhaust temperature controller bode plot, it was replaced with a lag compensator as in equation (20) and its response is shown in figure (21)

$$D(s) = \frac{0.5s + 1}{s + 1} = \frac{s + 2}{10s + 1} \tag{20}$$

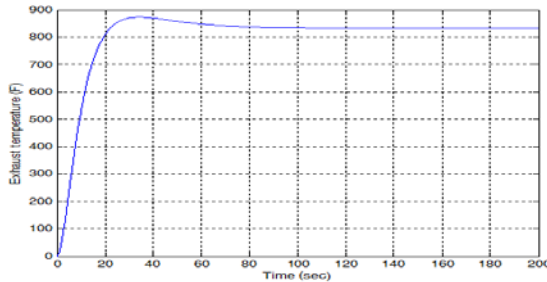


Figure 21: Exh. temperature lag compensator response after

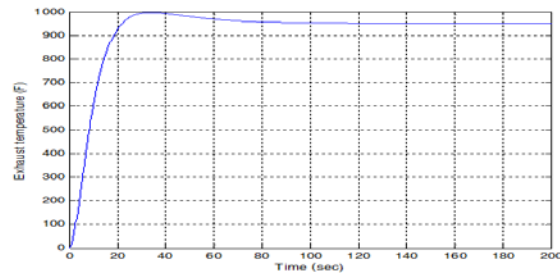


Figure 22: Exh. temperature lag compensator response after maintaining

According to fact which has (usually, as a general guideline, the upper corner frequency, $1/\tau$, of the compensator should be approximately one octave to one decade below the new gain crossover frequency ω'_g .) Taking:

$$\frac{1}{\tau} = \frac{\omega'_g}{10} = \frac{2}{10} \rightarrow \tau = 5$$

thus, the required lag compensator is:

$$D(s) = \frac{5s + 1}{100s + 1} \tag{21}$$

equation(20) will be as follows and Exhaust temperature lag compensator response is then shown in figure (22).

Bode plot of both PI Exhaust temperature controller and Lag compensator shown in figure (23) illustrate that both plots are nearly the same, Notice that the sample Exh. = Exhaust and Tem. = Temperature.

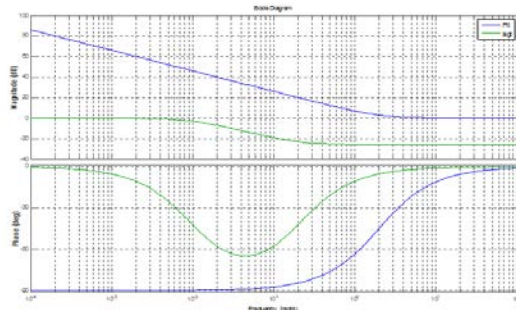


Figure 23: Bode plot of lag compensator and PI for Exh. Tem. temp. systems

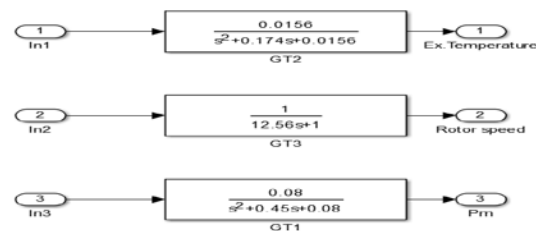


Figure 24: Transfer function of power, speed and temp. systems

We could notice here that there is no interaction between the three controllers, which supervisor controller is allowable to design. The whole system is stable and could be used in industrial. Figure (24) shows the collection of three PID controllers -exhaust temperature, mechanical & electrical

power and rotor speed- to build what is known of supervisor controller. The whole systems and supervisor controller itself all are shown in figure (25).

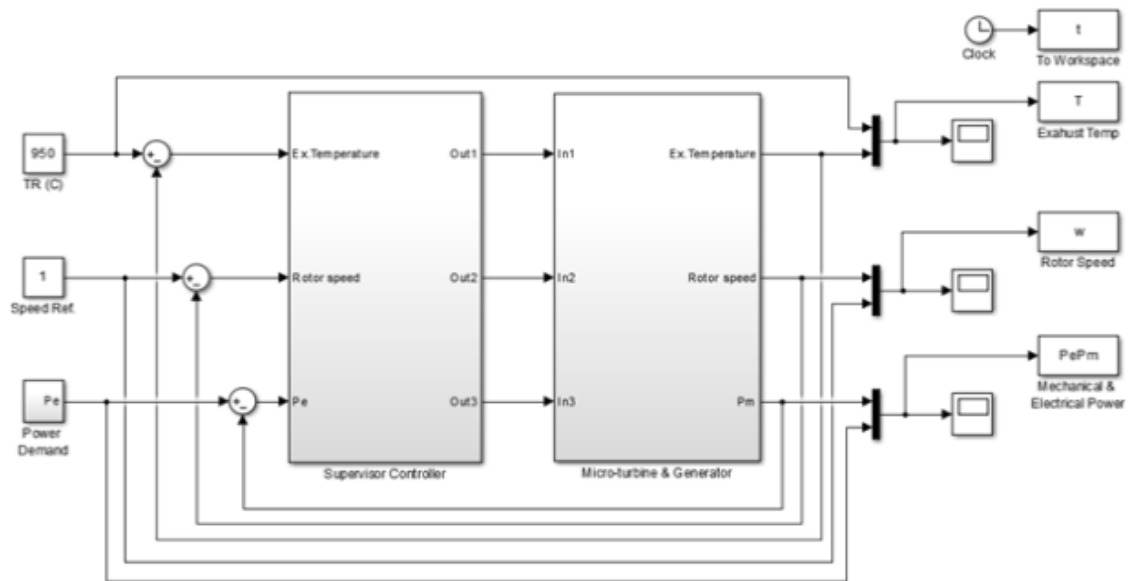


Figure 25: The plant of Micro-Turbine and generator.

11. Conclusion:

The main purpose of this paper is to model, simulate, and control design of the Micro-turbine which mainly used to maintain the continuously of electrical power of the grid. The simulation model is used to investigate the output response as well. Local controller was designed for Micro-turbine using PID controllers for both rotor speed and mechanical & electrical power systems, and a PI controller for exhaust temperature. The PID, and PI controllers tuned using Ziegler-Nichols method for Mechanical & electrical power PID controller and have been found suitable whereas, using trial & error was better for rotor speed and exhaust temperature systems, to reach an acceptable and particular output of the Micro-turbine systems. A compensators were designed for three systems - rotor speed, mechanical & electrical power, and exhaust temperature systems- instead of PID and PI controllers which have been designed before, using frequency domain with help of Bode plot reshaping. Interaction hasn't been detected between three systems. System reduction was resulted due to a MIMO (Multi-Input Multi-Output) system becomes a SISO (Single-Input Single -Output) system. Estimation and validation were both done for the PID and PI controllers. A supervisor control system was designed by collected the three IMC-based controllers and applied to the Micro-turbine. The time constant parameters were chosen to get the acceptable output responses.

References:

- [1]. P. RajaSekhar, L.S Enhancement of Micro Turbine-Generator Output Voltage Quality through Application of Matrix Converter Interface uresh, “, IOSR Journal of Engineering (IOSRJEN) PP 43-49 , (2013).
- [2]. Larry Goldstein, Bruce Hedman, Dave Knowles, Steven I. Freedman, Richard Woods and Tom Schweizer., “Gas-fired distributed energy resource technology characterizations,” National Renewable Energy Laboratory, NREL/TP-620-34783, Nov.(2003).
- [3]. W. I. Rowen, ‘Simplified mathematical representations of heavy duty gas turbines’,l Journal of Engineering for Power, Trans. ASME, vol. 105, no. 4,pp. 865-869, October (1983).
- [4]. GodswillOfualagba, ‘The Modelling and Simulation of a Micro-turbine Generation System’, IJSER International Journal of Scientific & Engineering Research Volume 2, Issue 2, ISSN 2229-5518, (2012).
- [5]. Emekausebiusomeife, ‘The impact of compressor cleaning in gas turbine engines used for oil and gas applications’, Msc. in communication, control and digital signal processing, (2010).
- [6]. M. Gopal, ‘Control system principle and design’, McGraw-Hill companies, (2008).

Optimal Power Loss Minimization using Optimal Size and Location of Shunt Capacitors, and DG

Hesain Milad Alfrd

hussein.alfared@elmergib.edu.ly

Department of Electrical & Computer Engineering, College of Engineering, Elmergib University, Libya

ABSTRACT

One of the biggest problems that face the electric distribution network is the power losses, which could be reduced for obtaining a good voltage improvement. Two effective case studies have been used to minimize the power losses; a conventional case study which could be represented by installing Shunt Capacitors, and a modern case study which could be represented by installing Distributed generators (DG). This paper presents effective approaches, to obtain the optimal size and location of each of Shunt Capacitors, and DG, based on Newton Raphson Numerical Method. The first approach proposes load flow, and the second approach proposes optimal load flow. A Libyan distribution network was chosen for the discussion and analysis.

Keyword— Loss formula, Shunt capacitor, Distributed generation.

1. Introduction

Installation of shunt capacitors in the electrical distribution system, has many advantages for many purposes. Inductive loads such as transformers and motors cause lagging power factor which leads to a reduction in capacity, voltage levels, and increasing power losses. Optimal capacitor placement provides a network with the necessary reactive power using Tabu Search method [1]. Various techniques have been applied using capacitor allocation, and every technique has its own advantages, and defects [2]. Shunt capacitors enhance the reactive power control in addition to the system reliability and security in the distribution network. For the compensated and uncompensated networks a state-space method is used to study the reliability index [3]. Minimizing the power and energy losses using a genetic algorithm where the major objective function is to decrease the cost depending on capacitor location and reactive power support [4]. Optimal capacitor location and size to supply with the necessary compensation for the better investment required to satisfy appropriate reactive constraints based on deterministic and genetic algorithm together [5]. The improvement of the Distributed Generation technologies has a large impact on power system operation. The renewable energy sources such as solar, wind, hydro, biomass, etc., is the most important motivation for the studies including the integration of DG to the electric grid. Voltage profile improvement and reducing power losses can be obtained by the installation of DG in the distribution network [6]. Essential definitions of DG and their operating constraints as well as their types, classification, and technologies [7]. DG on electric power system contributes to good power quality, voltage profile improvement, and loss reduction [8]. Hybrid PSO & HBMO algorithm is implemented in optimal placement and sizing of DG in the distribution network in order to decrease the total power losses

and obtaining voltage profile enhancement [9]. Genetic Algorithm is also used for optimal size and location of DG with the purpose of supplying necessary real and reactive power to a distribution network whereas the main objective is to minimize system losses and to enhance system reliability and voltage profile [10]. Power Loss Minimization and Voltage Profile Improvement of a Distribution System Using Optimal Size and Location of DG utilized on 11 (KV) real Libyan distribution system [11]. In this paper, the optimum size and location of the shunt capacitor, and DG connected to distribution system is studied by using an optimal control theory with an excellent solution approach (Newton Raphson).

2. Materials and Methods

The Newton–Raphson (NR) method has outstanding convergence characteristics for solving non-linear algebraic systems. In comparison with the Gauss-Seidel method, a lesser range of iterations is necessary for convergence provided that, the initial values are not far away from the final solution [12].

3. Theory and Calculation

Two case studies were applied to find the optimal size and location of a shunt capacitor, and DG separately using Newton Raphson method on a power distribution system, the following Computational procedure should be done as follows:

- Step 1: Run normal load flow to find the losses before the installation of the capacitor & DG.
- Step 2: Run normal load flow after installing unknown shunt capacitor size on each bus.
- Step 3: Find the optimal size of the shunt capacitor for each bus using Eq.(4).
- Step 4: Compute the total loss using Eq. (1) after placing a shunt capacitor of the optimal size obtained in step 3.
- Step 5: Run optimal load flow after installing unknown DG size on each bus.
- Step 6: Find the optimal size of DG for each bus using Eq. (3).
- Step 7: Compute the total loss using Eq. (1) for each bus by placing DG of optimal size obtained.
- Step 8: Locate each of shunt capacitors and DG on the bus at which the loss is minimum. This is the optimum location for a shunt capacitor or DG.
- Step 9: Run load flow with each of shunt capacitor and DG to get the final result.
- Step 10: The voltage profile has improved after connecting a shunt capacitor and a distributed generator on the optimal location using Eq. (6).

3.1. Mathematical Expressions and Symbols

Location and size of shunt capacitor & DG units are decided in such a way that minimum system power loss and desired voltage profile are obtained. Therefore, there is a need to define the system power loss as a function of each of shunt capacitor and DG size and system bus voltages. Hence:

$$P_{loss} = \sum_{i \neq j}^m P_{line} \quad (1)$$

Where P_{loss} : is the real power loss, and m : is the number of branches in the power system.

$$P_{line(i,j)} = P_{(i)} - P_{(j)} \quad (2)$$

$$P_i = P_{DG_i} - P_{D_i} = |V_i| \sum_{j=1, j \neq i}^n |V_j| [G_{ij} \cos(\theta_i - \theta_j) + B_{ij} \sin(\theta_i - \theta_j)] \quad (3)$$

$$Q_i = Q_{DG_i} - Q_{D_i} = |V_i| \sum_{j=1, j \neq i}^n |V_j| [G_{ij} \sin(\theta_i - \theta_j) + B_{ij} \cos(\theta_i - \theta_j)] \quad (4)$$

where ' i ' is the location of the capacitor or DG unit ($i=1, 2, 3, \dots, n$) and ' n ' is the total number of bus bars in the distribution network. P_i and Q_i are net real and reactive power injection in the bus ' i ' respectively. V_i is the voltage magnitude at the bus ' i ' respectively. P_{DG_i} and Q_{DG_i} are the real and reactive power generations of DG at the bus ' i '. P_{D_i} and Q_{D_i} are the real and reactive power demand at the bus ' i '. So objective function is to minimize the power loss considering following constraints:

$$P_{loss} = \sum_{i=1}^n P_{G(i)} - \sum_{i=1}^n P_{D(i)} \quad (5)$$

Where $P_{G(i)}$ is the generated real power in the bus ' i ', and $P_{D(i)}$ is the consumed power in the bus-' i '

Where ' n ' is a number of buses. It should highlight that enhancing the voltage profile depends upon minimizing the voltage

deviations as:

$$P_{loss} = \sum_{i=1}^n (|V_n - V_{ref}|)^2 \quad (6)$$

Where V_{ref} is the reference voltage that commonly equals to 1 p.u.

$$|V_{i \min}| \leq |V_i| \leq |V_{i \max}|$$

$$P_{line(i,j)} \leq P_{line(i,j) \max}$$

Proper settings for $|V_{i \min}|$ and $|V_{i \max}|$ results in better voltage profile of system.

4. Results and Discussion

A normal load flow and optimal load flow program run by Neplan (power simulation software) on a Libyan distribution network to find the optimum size and location for shunt capacitors, and distributed generation (DG). Simulations were carried out on a local distribution system, 11 kv, called Sileen Al-Bahria, in Khoms / Libya, located on an approximated area 120 km², and 78 loads.

4.1. The Consideration of Work

- 1) The data of loads obtained in currents, not in active or reactive power, measured per four months (by the general electric company of Libya).
- 2) The power factor of the loads was unknown. Hence, it considered 0.87 to calculate the active and reactive power.

- 3) The distribution system is unbalanced, which led to taking the average of the load currents, to represent the system in one line diagram per phase.
- 4) The load factor is equal to one.

4.1. Case Study I

The first case study is a normal load flow approach, which finds the optimal sizes of shunt capacitors installed at each bus, which gives the less loss according to capacitor size.

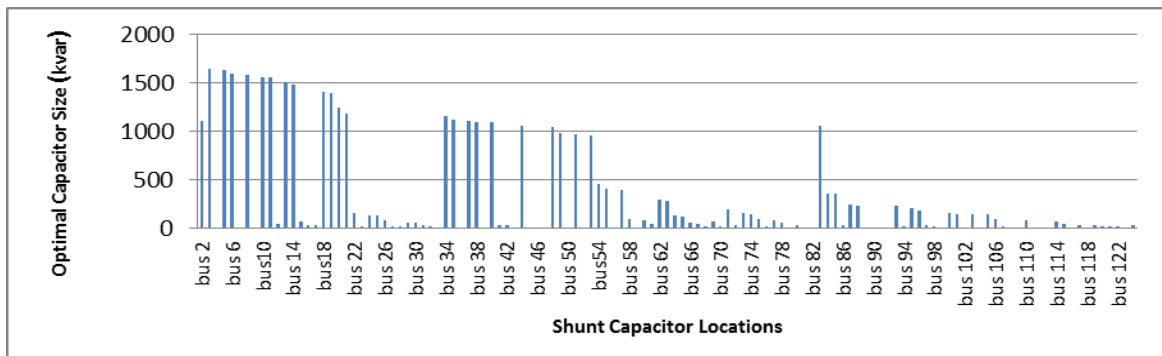


Figure 1: Optimal capacitor size for each bus bar locations

Figure 1 shows the shunt capacitor size, which is the optimal size for each bus bar location.

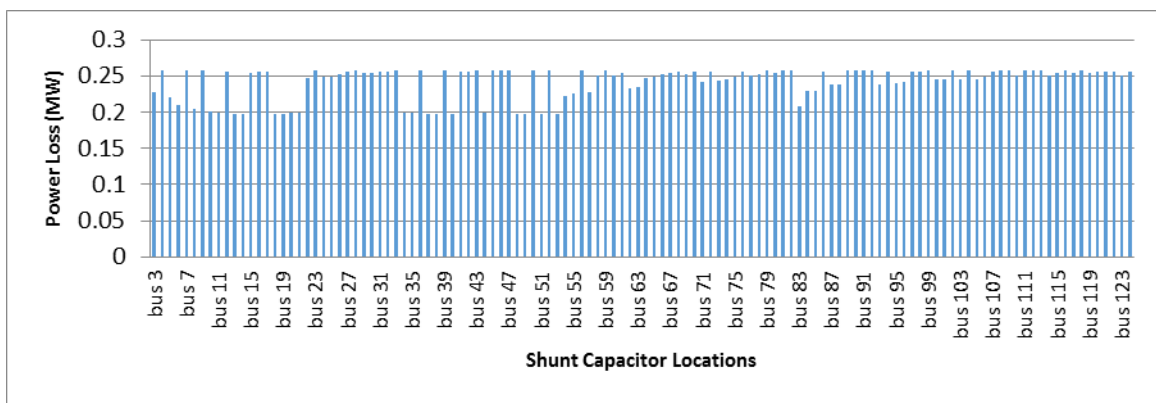


Figure 2: Power losses vs optimal shunt capacitor locations

Figure 2 shows the total losses for each optimal shunt capacitor size installed at each busbar in kvar and shows the optimal size which gives the less loss at bus 53 with total losses 0.1967 MW, and optimal capacitor size 960.5 kvar.

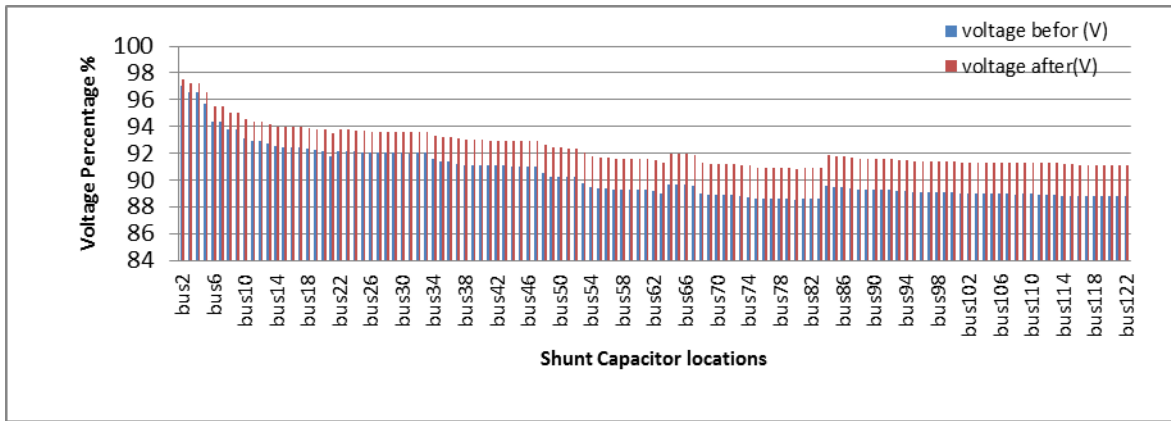


Figure 3: Voltage percentage vs shunt capacitor locations

Figure 3 after connecting a shunt capacitor at bus 53 with the optimal size 960.5kvar, shows obtaining a very good voltage improvement for each bus.

4.2. Case Study II

The second approach is an application of the optimal load flow by Newton Raphson wherein the optimal size of DG which could be found at each bus, which leads to finding the less loss in the network at all.

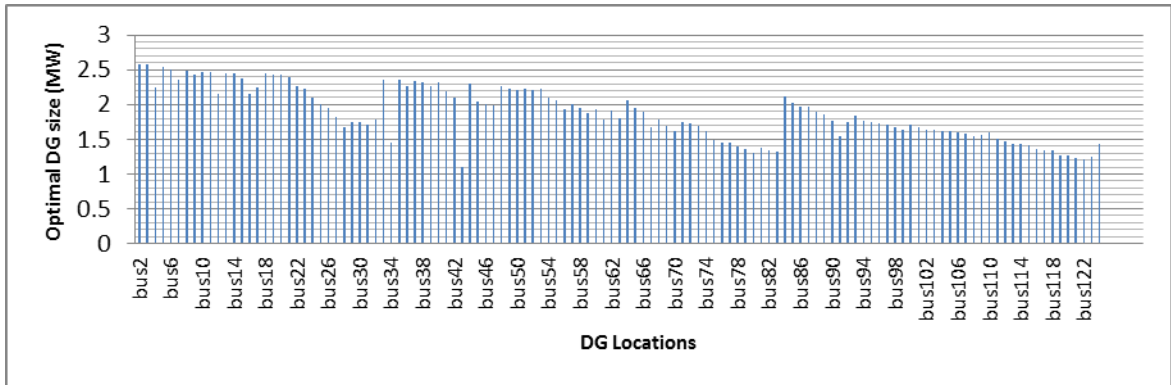


Figure 4: Optimal DG size for each bus bar location

Figure 4 shows the DGsize, which is the optimal size for each bus bar location.

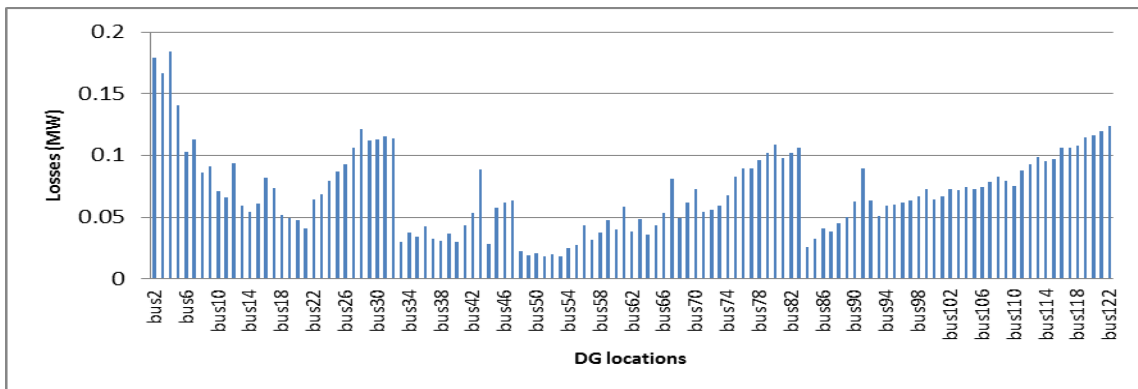


Figure 5: Power losses vs Optimal DG locations

Figure 5, which shows the total losses for each optimal DG size, installed at each busbar in MW, and shows the optimal size which gives the less loss at bus 53 with total losses 0.0292272 MW, and optimal DG size 2.218 MW.

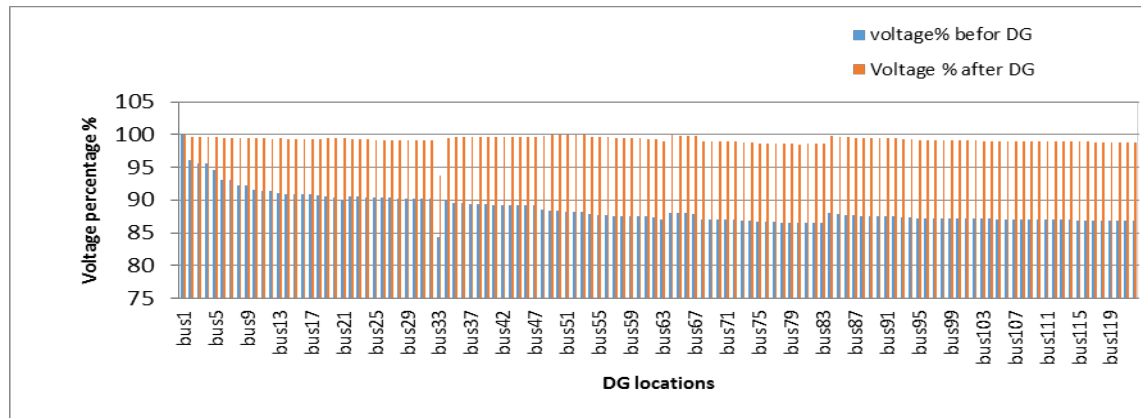


Figure 6: Voltage percentage Vs DG locations

Figure 6 after connecting a distributed generator at bus 53 with the optimal size 2.218 MW, shows obtaining a very good voltage improvement for each bus.

4.3. Comparison between the two case studies

The following table shows a comparison between the two case studies mentioned above:

Table 1: Optimal placement and sizing of DG and capacitor

Case study	Optimal bus location	Optimal size	Total Losses before	Total losses after	Power loss saving	Voltage Deviation (pu) before	Voltage Deviation (pu) after
Case I	53	960.5 kvar	0.2583 MW	0.1967 MW	0.0616 MW	1.1716	0.7327
Case II	53	2.218 MW	0.2583 MW	0.0292 MW	0.2291 MW	1.1716	0.0120

5. Conclusions

In this paper, an efficient optimization algorithm proposed for optimal size and location of shunt capacitor and DG on a Libyan distribution network . This method based on Newton Raphson has an efficient minimization of the real and reactive power losses and voltage difference to retain the voltage limits within the accepted range. Two effective case studies have been used; a conventional case study

represented by installing Shunt Capacitors, and a modern case study represented by installing Distributed generators (DG). A real application on a Libyan distribution network by NEPLAN Software is applied and gave good results of loss minimization & voltage profile. A Comparison between the two case studies showed the difference between them.

References

- [1]. R. A. Gallego, A. J. Monticelli, and R. Romero, "Optimal capacitor placement in radial distribution networks", IEEE Trans. on Power Systems, vol. 16, Issue 4, pp. 630- 637, 2001.
- [2]. H. N. Ng, M. M. A. Salama, and A. Y. Chikhani, "Classification of capacitor allocation techniques", IEEE Trans. on Power Delivery, vol. 15, pp. 387-392, 2000.
- [3]. Abdel hay A. Sallam, Mohamed Desouky and Hussien Desouky, "Shunt Capacitor Effect on Electrical Distribution System Reliability" IEEE Trans on Reliability, Vol. 43, Issue 1, pp. 170-176, March 1994.
- [4]. Srinivasan Sundhararajan and Anil Pahwa, "Optimal Selection of Capacitors for Radial Distribution Systems using a Genetic Algorithm" IEEE Transactions on Power Systems, Vol. 9, Issue. 3, pp. 1499-1507, August 1994.
- [5]. Maurizio Delfanti, Gianpietro P. Granelli, Paolo Marannino, and Mario Montagna, "Optimal Capacitor Placement Using Deterministic and Genetic Algorithms" IEEE Transactions on power systems, VOL. 15, Issue. 3, pp. 1041- 1046 August 2000.
- [6]. T. Ackermann, G. Anderson, L. Soder, "Distributed generation: a definition" Electric Power Systems Research, Volume 57, Issue 3, Pages 195-204, April 2001.
- [7]. El-Khattam and M.M.A. Salama, "Distributed generation technologies, definitions, and benefits" Electric Power Systems Research, Volume 71, Issue 2, Pages 119-128, October 2004.
- [8]. P. P. Barker, R. W. de Mello, "Determining the Impact of Distributed Generation on Power Systems: Part 1 - Radial Distribution System" IEEE Power Engineering Society Summer Meeting, vol. 3, pp. 1645-1656, 2000.
- [9]. M. Afzalan, M. A. Taghikhani, "DG Placement and Sizing in Radial Distribution Network Using PSO&HBMO Algorithms", Electrical Power Distribution Networks (EPDC), 2012 Proceedings of 17th Conference on, vol., no., pp.1-6, 2-3 May 2012.
- [10]. Carmen L.T. Borges, Djalma M. Falcao, "Optimal distributed generation allocation for reliability, losses, and voltage improvement", International Journal of Electrical Power & Energy Systems, Volume 28, Issue 6, Pages 413-420, July 2006.
- [11]. Hussein Alfared, Abdalla I. Fadel, "Power Loss Minimization and Voltage Profile Improvement of a Distribution System Using Optimal Size and Location of Distribution Generation," *Libyan conference LICEET 2018*, no. 25. March 2018.
- [12]. J. C. Das, "Power System Analysis Short-Circuit Load Flow and Harmonics", Marcel Dekker, Inc.

Experimental Investigation on the Performance Evaluation of Solar Tracking Photovoltaic System

A. Kagilik¹, S. Mousa², I. Enageem³

¹as.kagilik@gmail.com, ²salahmousa@hotmail.com, ³ana_geem@hotmail.com

^{1,2,3}Electrical and Electronic Department, Sabratha University, Sabratha, Libya

ABSTRACT

The optimization of photovoltaic (PV) power generating system needs to be magnified by maximizing the solar radiation falling perpendicular on the PV module surface. The photovoltaic module can extract maximum power from solar irradiance by optimizing its orientation and its angle of inclination with the horizon. Therefore, it is recommended that for high efficiency and low loss of energy. PV module needs to be tilted at the correct angle. On the other hand, solar tracking system can be used to maximize the performance of the PV system, since solar tracking allows more energy to be produced because the solar array is able to remain aligned to the sun. The aim of this paper is to investigate experimentally the performance evaluation of solar tracking photovoltaic system. In this direction, an extensive experimental work at Faculty of Engineering, Sabratha-Libya to improve the output power of PV module by implementation of one axis tracking system. The project will include the design and construction of a microcontroller-based solar panel tracking system. The operation of the experimental model is based on DC motor intelligently controlled by a dedicated drive unit that moves PV panel according to the signals received from two simple but efficient light sensors. Practical comparison between fixed and tracking systems using identical PV modules is performed. It is found that the tracking system significantly improves the output power of PV module compared to the fixed PV panel under same climate conditions. Results indicated that the tracking system increases the output current by more than 60% compared with fixed PV panel, especially at early morning hours and before the sunset hours. This demonstrates, as expected, that the tracker photovoltaic system provides more efficient performance compared to the fixed photovoltaic system.

Keyword— solar radiation, Photovoltaic system, tracking system

1. Introduction

Recently, the demand of the renewable energy such as wind energy, solar energy, etc. has been increased dramatically around the world due to reduction in existing sources of fossil fuels and the growing concern regarding environment pollution. The conversion of solar light into electrical energy represents one of the most promising and challenging energetic technologies. Today, photovoltaics is considered as highly competitive technology and its world market is mainly fully developed including PV system components (mechanical/electrical). During the last decade, PV is applied at countless locations in many countries and has been implemented successfully with rapid falling installation costs and environments throughout the planet. The world wide cumulative PV capacity reached about 303 GW by the end of 2016. During 2016, at least 75 GW PV capacity was added compared to 51 GW during 2015 with percentage increase up to 47 %. On the other hand, the global weighted

average total installed cost of commissioned utility-scale (larger than 1 MW capacity) solar PV projects between 2010 and 2016 fell by 65%, with the levelised cost of electricity (LCOE) falling by 67% over the period. In 2016, an average LCOE of around USD 0.12 per kWh, and a range of USD 0.05 per kWh to USD 0.35 per kWh was achieved according to region [1].

The maximum solar energy extracted from the solar photons is affected by the amount of the collection of the sun radiation and the performance of PV power generating system is highly influenced by the incident solar radiation reaching the surface of the collector. Solar irradiation on PV modules varies with the modules position and the PV output power takes its maximum value when the solar radiation is perpendicular on the collector. Therefore, the optimization of PV module needs to be magnified by optimizing its orientation and its angle of inclination with the horizon. From our previous work, the strongly dependence of the maximum output power on the optimum inclination angle of the fixed PV solar module has been demonstrated and it has been found that the optimum tilt is different for each month of the year and the yearly average optimum tilt is approximately equal to the latitude of the site. Unfortunately, in spite of keeping the classical fixed PV panel in optimum position, the necessary optimum insulation for the maximum performance of PV module cannot be obtained during the whole year [2]. Thus an annually improving the output energy can be obtained by aligning the PV module with the sun such that the maximum radiation falls perpendicularly on the module surface, and the problem of loss can be avoided during the whole year.

Recent technology for optimization both the PV solar module orientation and angle of inclination and maximizing the PV performance is characterized by using the solar tracking system. Unlike the classical fixed PV panel, the function of the solar tracking device is following the sun trajectory such that the solar module is kept under optimum insolation for all positions of the sun. The sun tracking system approach must be equipped with essential features which are the azimuth tracking for adjusting the tilt angle of the surface of the PV array during changing seasons; and daily solar tracking for maximum solar radiation incidence to the PV array [3]. There are two main types of trackers, single axis and dual-axis, which usually operate using either a passive or active mechanism. It has been estimated that the tracking system increases the yield by (30 -60%) compared to stationary one. However, although the tracking systems strongly enhance the module efficiency, they increase the initial cost and complexity of the system and therefore they are still not practical solution for a small-scale application [4].

To date, the performance of photovoltaic (PV) systems with different available technologies of solar trackers have been designed and executed by many workers. In this direction, numerous methods and mathematical models have been considered to validate the design methodologies. Many measurements setup including microcontroller-based solar panel tracking system, stepper motors and drivers, light intensity sensors, voltage regulation, physical construction, and software/system operation explanation have been used to obtain the optimum PV system performance under different climate conditions. Their analyses show an increase of solar irradiation upon a tilted system, azimuth tracker system, and dual axis tracker system as compared to the horizontal system [4, 5].

The aim of this paper is to investigate experimentally the performance evaluation of a single axis solar tracking photovoltaic system under Libyan climate conditions. The measurements are performed during the whole year and the optimized tracking system for four seasons are documented. Different preliminary results are presented in a number of graphs and table for a better interpretation. The proposed tracking method in this paper has been compared with conventional fixed method and good agreement with other investigators has been demonstrated.

2. Solar Photovoltaic Tracking System

2.1. System description

The main solar tracking PV system under investigation in this work is presented. The single-axis solar tracking system consists of a PV panel rotating around a tilted shaft, under the action of a DC motor controlled with respect to the real Sun position estimated by means of two light intensity sensors. Depending on the orientation type solar trackers have a movement part based on a sun trajectory that updates the PV panel position according to the instantaneous solar irradiation. Therefore, the proposed solar tracking system was designed and executed so that specific technical requirements such as: optimum performance, operation reliability, movement simplicity are satisfied. Figure 1 shows the PV solar tracking system which designed and built in this work, while figure 2 illustrates the basic control circuit for a unipolar stepper motor or the complete hardware schematic of the system. As shown in the figures above, the solar tracking PV panels consists of moving parts and control elements, such as: PV module, DC motor, Light sensors, Limit Switch, relay and the Microcontroller. In this section, the background information on the main subsystems of the project was presented. The main part of this system is the PV module under measurements which is considered as a energy source.

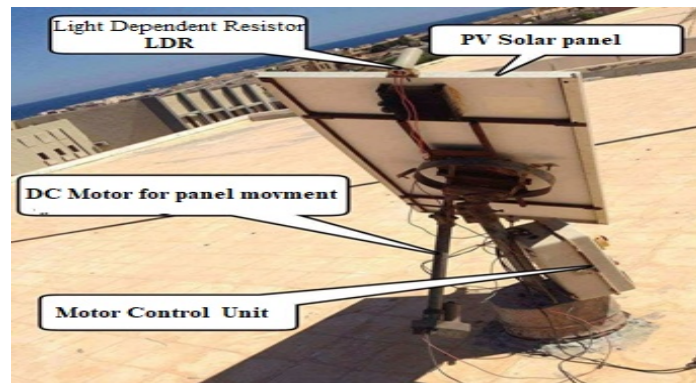


Figure 1: Solar tracking system

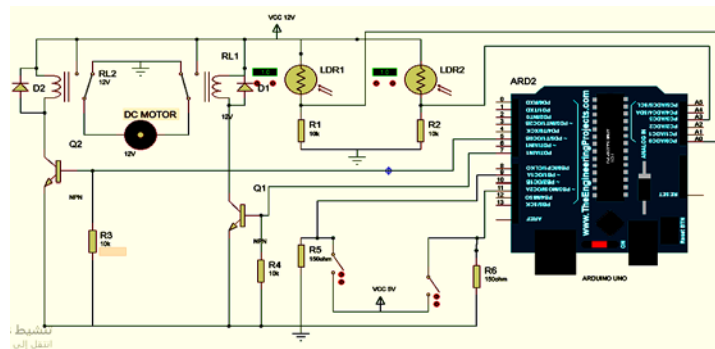


Figure 2: Hardware Schematic Diagram

The second part of the system is the stepper DC motor. This motor is commonly used for precision positioning control applications and it was chosen to position the tracking sensor. The motor is characterized by brushless device, open loop positioning capability, good holding torque, excellent response characteristics and less circuit complicity.

The project consists of two reading of light sensor values which can control a motor to align with the greatest value which corresponds to the sun's position. Thus, these sensors allow an update of the PV panels position on a monthly or seasonal basis to obtain better PV performance and increase the global energy output of the system. Light sensors are among the most common sensor type. The simplest optical sensor is a photo resistor or Light Dependent Resistor (LDR) that the resistance of these sensors decreases with an increase in solar intensity. This is the least expensive and least complex type of light sensor.

Lastly, a microcontroller is provided to the control circuit. Since the project's focus is on embedded software control, the microcontroller is the heart of the system. The microcontroller selected for this project is able to convert the analog photocell voltage into digital values and also provide output channels to control motor rotation. The Arduino™ MEGA2560R3 was selected as it satisfies these requirements in addition to already being provided with the class lab kit. MEGA 2560 R3 is an Arduino compatible board with Microcontroller AT Mega 328, it's based on Arduino MEGA 2560 design. All Code, shield and IDE for Arduino MEGA 2560 R3 are also valid on BUONO MEGA 2560, some visible improvement on hardware make BUONO more flexible and easier use, and it's designed for projects that require more I/O lines, more sketch memory and more RAM with 54 digital I/O pins, 16 analog inputs. The Arduino Mega 2560R3 is programmed using the Arduino Software (IDE). The Arduino Programming language is easy to learn and understand since the Arduino IDE is linked with some software's such as: Max MSP processing and MATLAB.

2.2. Algorithm for Control of Tracking System

Figure 3 shows the flowchart of the tracking system control algorithm, while figure 6 illustrates the system protocol. As can be seen, the operation of PV tracking system is based on sensor method. This programming method, using Proteus software, is to track sun's trace by using photo sensors (LDR's) that is tracked through difference in amount of light. On the other hand, the photo resistor

and stepper motor theory is discussed in order to provide a better understanding as to how they relate to the solar tracker.

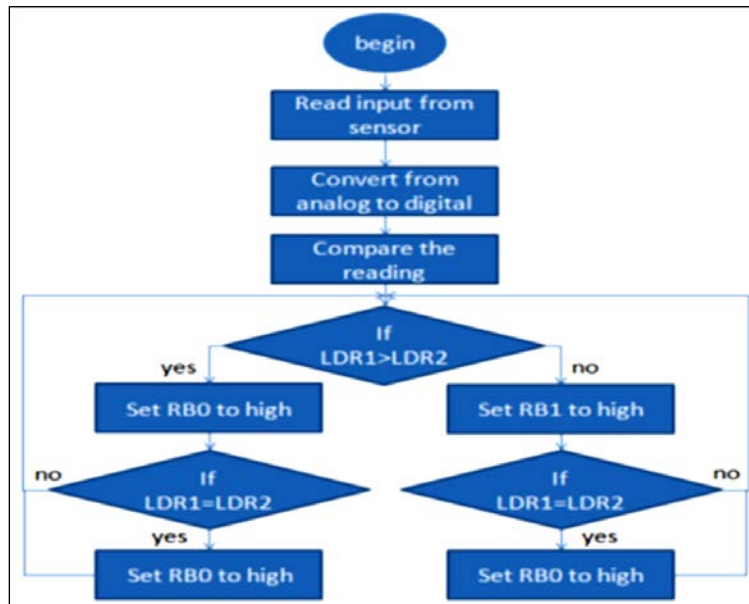


Figure 3: Flowchart of the tracking system control algorithm

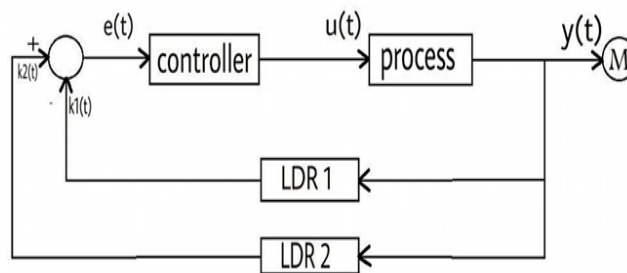


Figure 4: System control protocol

The error signal $e(t)$ is compared with the light intensity detected by the two LDRs as feedback signal. Therefore, the output error signal or the voltage difference will control to the movement direction of the PV panel, so as to bring it normally oriented to the incident sun light rays and thus to obtain a maximum conversion efficiency of light into electricity. The error signal is characterized by the difference between two sensors signals $K_1(t)$ and $K_2(t)$ through the relation given by:

$$e(t) = k_2(t) - k_1(t) \quad (1)$$

Where $k_1(t)$ and $k_2(t)$ are the first and second sensor signal, respectively. Depending on the light intensity imposed to the both sensors, there is a difference in the internal resistance value. That means when LDR1 receives much light that LDR2, then the internal resistance value of LDR1 is smaller than of LDR2 and hence this difference value will be received by the controller which works as a comparator that the output will send a signal to one of the transistors (processor) which works

as On/Off switch, hence the transistor connect the current to the relay which control to the DC motor, as shown in figure 4. However, the DC motor that ensures the PV panel movement according to system protocol, as follows:

$$e(t) = 0 \text{ no move} \quad (2)$$

$$e(t) > 0 \text{ right move} \quad (3)$$

$$e(t) < 0 \text{ left move} \quad (4)$$

This process will be continued during the whole day until sun set. Therefore, the controller will receive a signal from the limit switch that the DC motor will move to its original position and stops its movement until the second day, and so on. This process is also happened in a very cloudy day. In this case, the motor control unit will readjust the solar panel position until the sun shines again to continue the desired protocol, but this phenomena is rarely happened in our climate here in Libya.

3. Experimental Investigation

Experimental investigation was carried out in order to compare the performance of the solar tracking PV panel in comparison with a fixed PV panel of the same type. In this direction, an extensive experimental work at Faculty of Engineering, Sabratha-Libya was performed, to determine practically how solar PV tracking system can be optimized to extract the maximum power. Unfortunately, no long term ground global horizontal measurement stations were located near the site selected. However, it should be realized that all the data used in this work were based on the calculation of solar radiation in Sabratha city using MATLAB simulation software.

The photovoltaic performance of solar module was obtained by measuring the current–voltage characteristics under natural climate conditions. The PV modules under investigation which were installed on the roof top of Electrical Engineering Department are TE750 TOTAL poly-crystalline commercially modules with capacity of 75 W and dimension of 31x125 cm² for each module. The typical specifications of the PV solar module at STC (AM1.5, 100W/m²at 25 °C) is shown in Table 1.

Table1: Technical Data for Solar Module

Electrical characteristics	Specifications
Module type	TOTAL TE750
Number of Cells	80
Typical Peak Power (P _{max})	75W
Voltage at Peak Power (V _{mp})	17 V
Current at Peak Power (I _{mp})	4.4 A
Short Circuit Current (I _{sc})	4.7 A
Open Circuit Voltage (V _{oc})	21.6 V
Minimum Power (P _{min})	70.1 W
Minimum Pass Diode	6 A
Minimum Series Fuse Rate	8 A

Unlike the classical fixed PV panel, the mobile one driven by solar tracker is kept under optimum insolation for all positions of the Sun, boosting thus the PV conversion efficiency of the system. The experimental procedure is characterized by measuring the output current, voltage and power produced from PV module that using single axis solar tracker system that automatically searches the optimum panel position with respect to the sun is compared with 30° tilt angle fixed PV module to act as a comparison reference. It is documented from previous study that this tilt angle is found as the optimum angle for four seasons at this location [2]. However, to demonstrate that the tracking system was working in optimum conditions, a video camera has installed and observe the movement of the PV module if it can response to the sun position during the whole day. It was found that, fortunately, the system was working perfect and satisfactory results have been determined and documented.

4. Results and Discussion

Solar irradiance is one of the most important parameter for evaluation of PV system performance. Based on site metrological data (latitude and longitude) of sabrathah city, where the PV module characteristics measurements were taken, a simulation of solar radiation has be performed. The calculations have been done during the whole year. For comparison, two days in summer season where the sun shine duration is more than 7 hours (at about 1000 W/m² incident power)have been chosen. Figure 5 and figure 6 illustrate the average solar irradiance (W/m²) incident on 30° tilted PV module. The calculations have been done for one day from the sun rise to sun set. As can be seen, it is found that the simulation results is in agreement with the data registered from metrological stations in Libya.

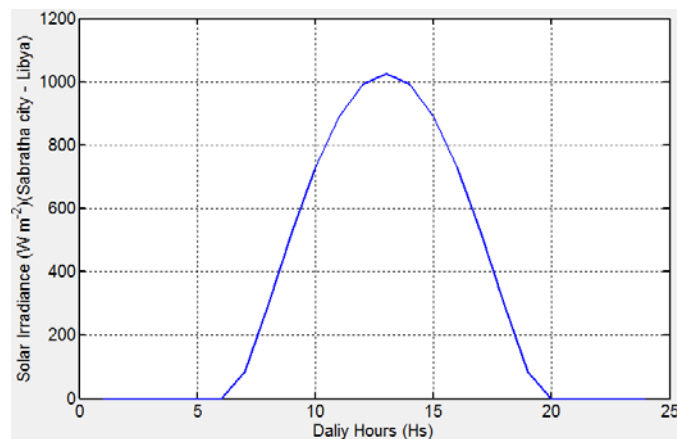


Figure 5: calculated solar radiation on tilted PV module using MATLAB simulation software (29.06.2017)

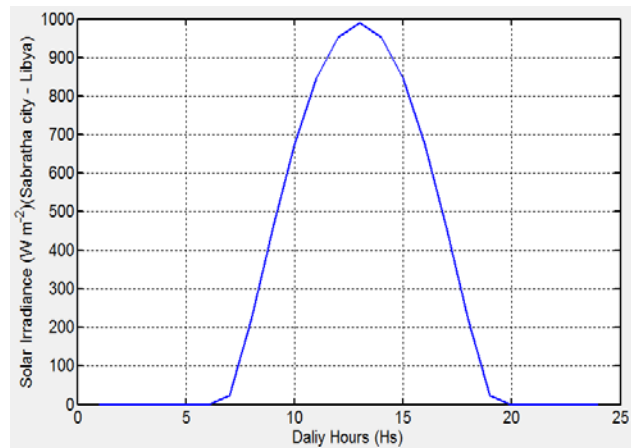


Figure 6: calculated solar radiation on tilted PV module (16.08.2017)

By measuring the current-voltage characteristics, the dependence of the photovoltaic performance on the solar irradiance has been investigated. The output power production of PV tracking module as compared to the fixed PV panel has been obtained, respectively. The measurements have been taken during four seasons and annual analysis has been documented. Since, the short circuit current (I_{sc}) increases linearly with irradiance increasing, while the open-circuit voltage increases logarithmically with intensity, it is focused on the dependence of current on solar irradiance for both PV modules, due to the strongly dependence on radiation intensity [6]. The dependence of I_{sc} on the solar radiation for fixed and tracking modules at selected two days are shown in figures 7 and 8.

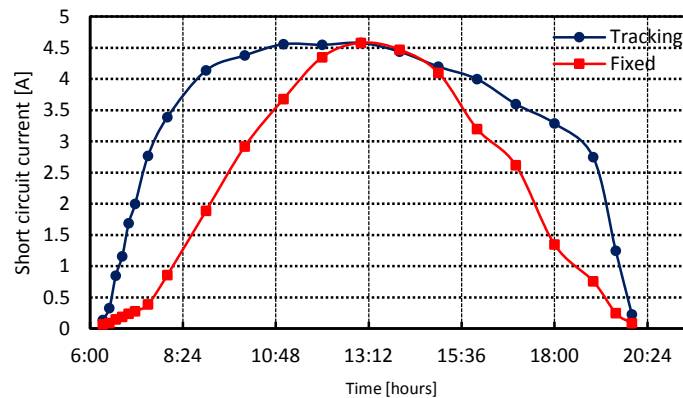


Figure 7: The dependence of the I_{sc} on the solar irradiance (29.06.2017)

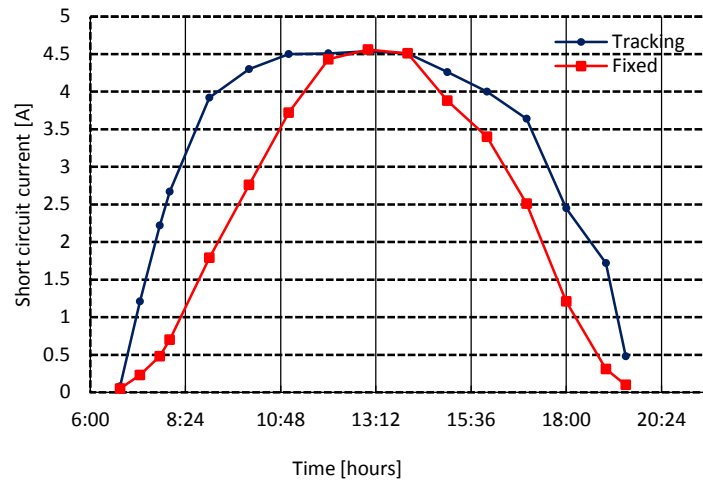


Figure 8: The dependence of I_{sc} on the solar irradiance (16.08.2017)

As can be seen, the maximum current is obtained at the med day where the solar irradiance is maximum. On the other hand, the maximum performance obtained at optimum positions are very close to the module data specifications illustrated in table1. However, results show an increase in current of tracked panel as compared to the tilted fixed panel. This is because the maximum solar radiation is almost falling perpendicular on the tracked module surface during the whole day, which is not possible for the fixed PV panel [7]. The tracked module achieves higher performance at the morning and evening period than the fixed PV panel, reaching up to 60% improvement at this time period due to the more light intensity absorbance. It is observed that at midday almost both panels have same output and no significant difference in current because of the same tilt angles at this time and all the systems receive almost the same amount of irradiation approximately. Finally, according to our results, it is demonstrated that the single-axis tracking panel has the highest performance compared to the other fixed PV panel.

5. Conclusions

The sun tracking has an essential advantage that provides the maximum output energy with high accuracy against any variation of incident light from the sun or climatic conditions change compare to fixed PV module due to the surface of PV module is not perpendicular toward the sun at each time. In this work, an experimental study has been made to improve the PV system output performance through maintaining the module surface in optimum position for receiving maximum solar radiation. In this direction, single-axis solar PV tracking system has been designed and executed. To demonstrate of the feasibility and effectiveness of solar tracking system, an experimental investigation has been performed.

The current–voltage characteristics of the tracked PV module have been carried out and the dependence of the short circuit current on solar irradiance has been determined. From these measurements, it has been found that there is an significant improvement in the PV module performance and an enhancement in module current of more than 60% has been obtained compared

to the tilted fix PV module, specially at the morning and evening time periods. This can be explained by that the tracked module surface almost remains under perpendicular irradiance receiving maximum radiation during the whole day.

References

- [1]. REN21, Renewables 2017, Global Status Report, PP. 63-71, Paris: REN21 Secretariat, ISBN 978-3-9818107-6-9.
- [2]. S. Mousa, I. Najem, O. Wehida, A. Khlifa, and A. Kagilik, "Optimization of Tilt Angle for Extracting Maximum Power from Photovoltaic Modules", *Libyan International Conference on Electrical Engineering and Technologies (LICEET 2018)*, 4-6 March, 2018, Tripoli – Libya.
- [3]. Bill Lane, "Solar Tracker", *EEC 517*, Department of Electrical and Computer Engineering, Cleveland State University, April 30, 2008.
- [4]. Tiberiu Tudorache, Constantin Daniel Oancea, Liviu Kreindler, "Performance evaluation of a solar tracking PV panel", *U.P.B. Sci. Bull., Series C*, Vol. 74, Iss. 1, PP. 3-10, 2012, ISSN 1454-234x.
- [5]. Mostafa mehrtash, Guillermo quesada, Yvan dutil, Daniel rouse, "Performance Evaluation of Sun Tracking Photovoltaic Systems in Canada", *20th Annual International Conference on Mechanical Engineering- ISME2012*, 16-18 May, 2012, School of Mechanical Eng., Shiraz University, Shiraz, Iran, ISME2012-2329.
- [6]. S. Buday, "Measuring irradiance, temperature and angle of incidence effects on photovoltaic modules in Auburn Hills, Michigan", *MSc Thesis*, University of Michigan, August, 2011
- [7]. S. Lakeou, E. Ososanya, B.O. Latigo, W. Mahmoud, "Design of a Low-cost Solar Tracking Photovoltaic (PV) Module and Wind Turbine Combination System", University of the District of Columbia.

Comparative Analysis of Electric Field and Potential Distributions over Porcelain and Glass Insulators Using Finite Element Method

Adnan S. Krzma^{1*}, Mahmoud Y. Khamaira², Marwan Abdulsamad³
1Salamaaek@Elmergib.edu.ly, 2Mykhamaira@Elmergib.edu.ly, 3Marwan18Abdulsamad@gmail.com
^{1,2,3}Department of Electrical and Computer Engineering, Faculty of Engineering, Elmergib University, Libya

ABSTRACT

This paper investigates the electrical performance of outdoor porcelain and glass insulators when subjected to an 11 kV AC voltage. The insulators are modeled in two dimensions, and the analysis of COMSOL software is used for the finite element simulations. The electric field and voltage distribution in the vicinity of the insulator surfaces were computed and examined. Comparative studies of field and equipotential lines for the insulators are presented under both dry clean and wet polluted conditions. The pollution layer over the insulator surfaces are assumed to be uniform with 0.5 mm thickness. The simulation results show that the field distribution of porcelain and glass insulators were obviously depended on the contamination conditions. The critical of high field regions on both surfaces were identified and the effect of the pollution on the electric field distribution was revealed. The results also confirmed that porcelain insulator has slightly higher field distribution near the high voltage end compared with the glass surface.

Keyword— Electric field distribution, potential distribution, finite element method, porcelain insulator, glass insulator.

1. Introduction

Outdoor high voltage insulators play an important role in the reliability of power system networks [1, 2]. Ceramic insulators have been extensively used in power transmission lines and distribution systems. In fact, insulator has crucial problems when exposed to environmental and electrical conditions. The problem of the pollution is one of the phenomena affect the insulator experienced by many utilities [3, 4]. The presence of the pollution layer on the insulating surface is quite common especially in costal and industrial areas. It is known that the performance of the dry insulator surface remains usually unchanged. But, when the polluted surface becomes wet, water films are formed on the insulating surface and noticeable leakage current flows [5]. The flow of leakage current on the insulator surface may increase the probability of dry band arcing and this can eventually cause a complete flashover or degrade the insulator [6]. Therefore, field and potential distribution around the insulator are essential not only for the dry clean surface, but also for wet polluted condition. Moreover, knowing the electric field distribution along the insulator surface is very important for the detection of defects in the insulator. On this basis, computation of potential changes and field distribution is believed to provide valuable information on the state of the insulator and this may improve the reliability of the system [7].

In this paper, the performance of cap and pin ceramic insulators is investigated. The insulators are modelled based on the Finite Element Method (FEM) and a two dimension (2D) model COMSOL Multi physics software is used for the simulation. The main purpose of the simulation was to evaluate the electrical performance of porcelain and glass surfaces under both dry clean and wet polluted conditions.

2. Insulator Profile and Computational Modeling

2.1. Insulator Profile

The insulator investigated in this study is a standard cap and pin suspension insulator rated at 11 kV. The insulating material and geometry of the insulator are shown in Figure 1.

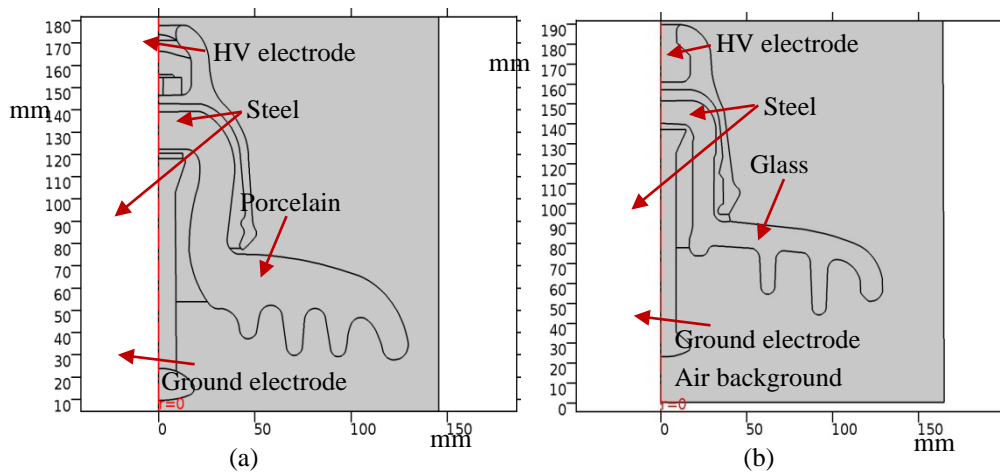
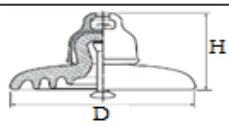


Figure 1: Cross-sectional profile of an 11 kV cap and pin insulator: (a) porcelain (b) glass

The technical dimensions of 81022 porcelain and U100BL glass profiles are summarized in Table 1, in which D is the diameter of the insulating part, H is the configuration height and L is the nominal leakage distance.

Table 1: Dimensions of 81022 porcelain and U100BL glass insulators

Profile	Material	Parameters (mm)		
		D	H	L
	Porcelain	257	146	320
	Glass	255	127	320

2.2. Material Properties

The insulators are generally comprised of two main components. The dielectric component which are porcelain and glass and the terminations which are cap and pin. The insulating housing is made of porcelain and glass materials with a relative permittivity of $\epsilon_r = 4.2$. The end fitting elements used for

the high voltage and ground electrodes are made of a steel. These fittings are crimped to the dielectric to support the mechanical strength of the insulator. In this simulation, the dielectric materials of porcelain and glass were assumed to be perfect insulators with a conductivity of $1 * 10^{-14}$ S/m. The air background region surrounding the insulators was specified with appropriate conductivity of $1 * 10^{-15}$ S/m. The pollution layer along the insulator surfaces is assumed to be uniform with 1.5 mm thickness. The conductivity of the pollution layer was adopted from the laboratory with a value of $600 * 10^{-16}$ S/m and the permittivity of the layer is set to be 81 [8]. The electrical properties used for the insulator modeling are specified in Table 2.

Table 2: Dimensions of 81022 porcelain and U100BL glass insulators

Material	Relative permittivity, ϵ_r	Conductivity, σ (S/m)
Air	1.0	$1 * 10^{-15}$
Porcelain	4.2	$1 * 10^{-14}$
Glass	4.2	$1 * 10^{-14}$
Steel	1.0	$1.45 * 10^6$
Cement	2.09	$1 * 10^{-14}$
Pollution layer	81	$600 * 10^{-6}$

The high voltage (HV) terminal which represents the cap was energised with an AC voltage of 11kV at 50 Hz. This r.m.s value was subjected to the insulator under both dry clean and wet polluted conditions, according to the IEC 60507 standard [9]. The lower pin terminal was connected to the ground at 0 V. The air region surrounding the insulator is simulated effectively large to reduce its influence on the potential distribution over the insulator profile and near to the electrodes. The outer edges of the air region are allocated with a boundary that expected zero external current and electromagnetic sources, hence demonstrating a physical system that is in isolated open space.

2.3. Finite Element Method (FEM)

The procedure for creating the 2D symmetrical model was achieved by drawing the insulator using AutoCAD tools and saved in an extension file of dxf format. The insulator was then imported to the COMSOL 5.2 Multi physics software. The simplification of using the 2D model instead of three dimensions (3D) model is preferred. This is because it saves a significant size of memory and processing time without affecting the accuracy of the simulation results. In addition, using symmetric model, only half of the insulator structure was modelled.

After completing the stage of the structure, the model is assigned with a suitable material properties and boundaries conditions as previously described. As a part of FEM system, the entire geometry of the insulator except the end fitting regions were divided into small triangular elements as shown in Figure 2. This process is called the meshing. This meshing discretisation can enhance the accuracy of the simulation results by increasing the number of meshing elements over the insulator surface where the field intensity is found to be higher.

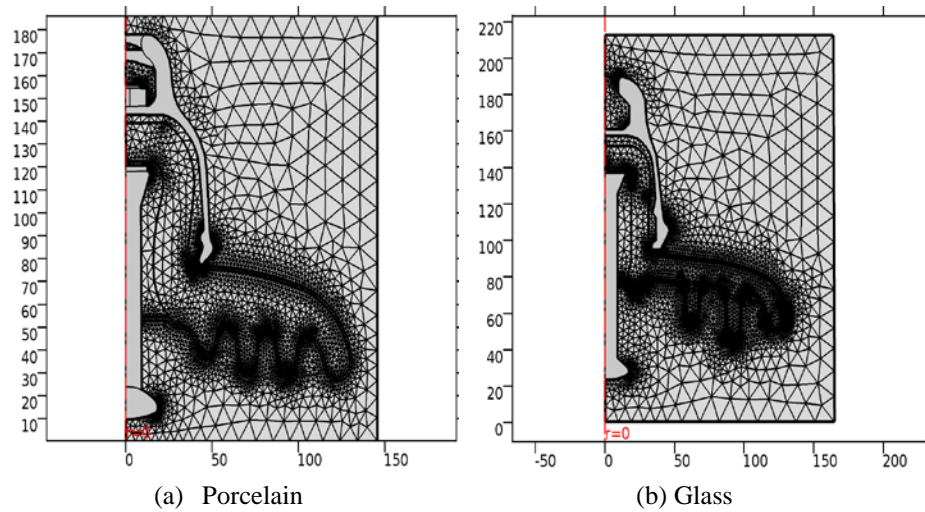


Figure 2: Meshing discretisation of insulator domain (a) Porcelain (b) Glass

The insulator model is analysed using the FEM based on Quasi-Static Electric mode, which assumes that the current changing slowly with the electromagnetic field [10]. This assumption is effective for insulator and many high voltage applications that operate at 50 Hz power frequency. The potential and field distribution are computed by solving the differential equation in the software given by equation (1).

$$-\nabla \cdot (\epsilon_0 \epsilon_r \nabla r) / \partial t - \nabla \cdot (\sigma \nabla V - J_e) = QJ \quad (1)$$

Where J_e : External current density (A/m²)

QJ : Current source (A/m³)

σ : Electric conductivity (S/m)

ϵ : Permittivity

3. Simulation Results and Discussion

3.1. Potential Distribution

The voltage distributions along the porcelain and glass insulators were computed for analysing and investigation studies. Figure 3(a) and Figure 3(b) respectively show the equipotential lines along the porcelain surface under both dry clean and wet polluted conditions. The lines are modeled at 5% voltage interval, therefore a total of 20 equipotential lines are plotted in the simulation results. The same action for voltage computation was achieved over the glass surface and Figure 3(c) and Figure 3(d) respectively observe the behaviour of the insulator under a certain conditions. As can be seen from both insulators, more than 75% of the voltage lines concentrated between the pin fitting and the first inner skirt. Over 15% of the voltage contours is concentrated nearby the cap.

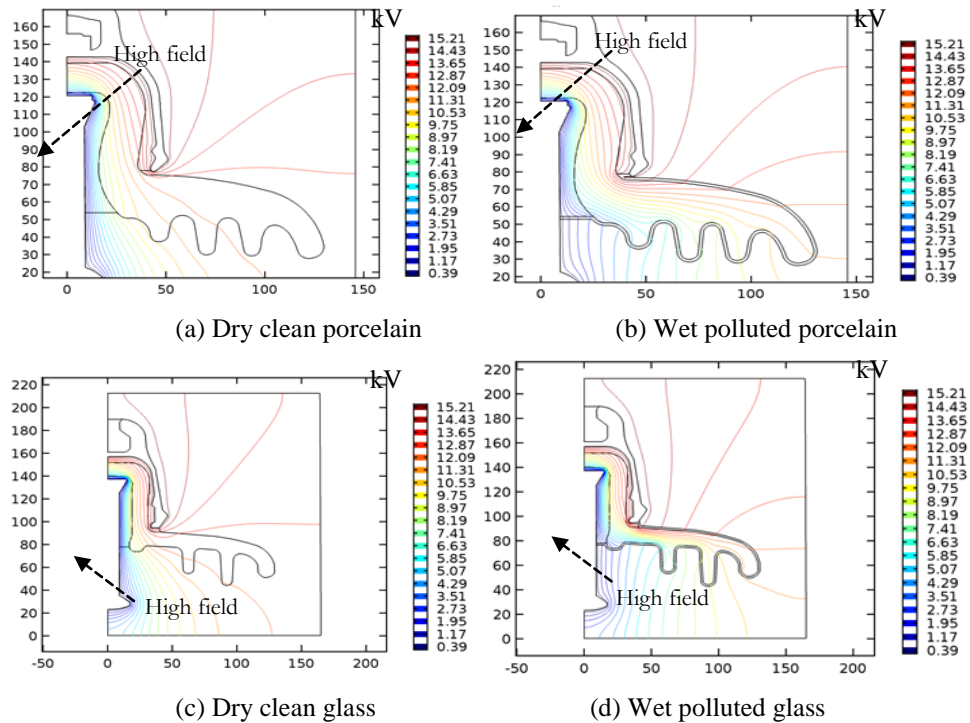
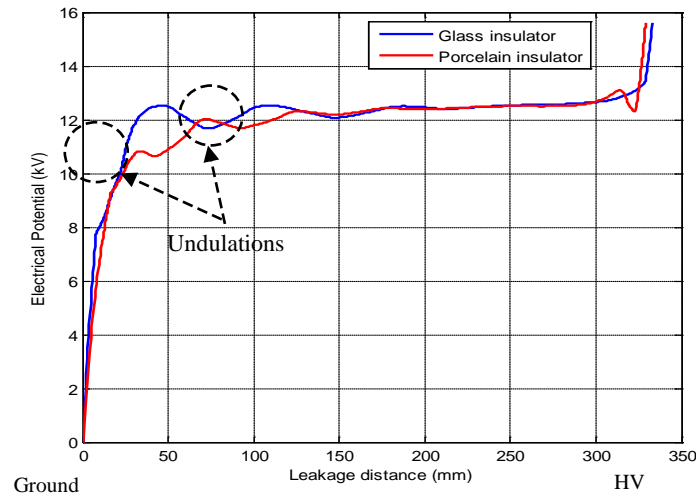
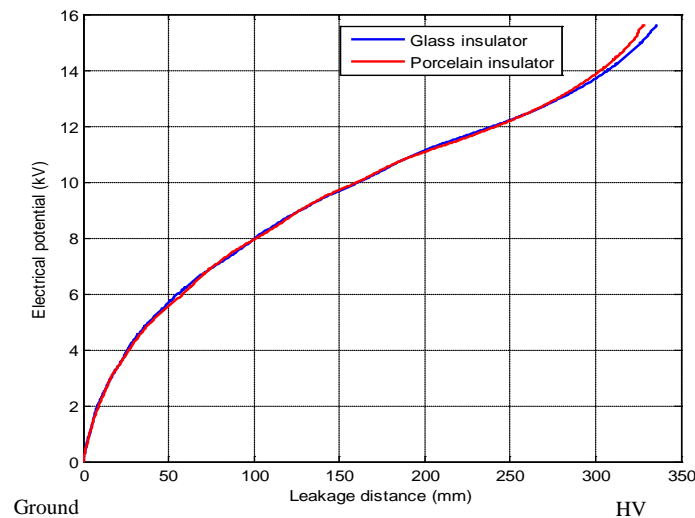


Figure 3: Equipotential contours over the surface profile of porcelain and glass insulators under dry clean and uniformly wet polluted conditions

The lines are commonly concentrated close to the end fitting regions and this may indicate to the highly field stress. When the insulator is polluted, the potential distributions are start to be uniform compared with those attained from the clean surface. This behaviour happens due to the presence of the pollution layer which helps to redistribute the potential lines widespread over the surface. The computed voltage profile along the porcelain and glass insulators under both surface conditions are shown in Figure 4. The leakage path of the insulator is measured along the surface, starting from the ground and termination at the HV end. An increase trend is observed for both graphs when shifting to the energisation end.



- Dry clean surface



- (b) Wet polluted surface

Figure 4: Voltage profiles along the porcelain and glass insulators: (a) dry clean, and (b) wet polluted

For dry clean insulators, a steep rise in the potential is observed up to 11 kV for the porcelain and 12 kV for the glass at a surface distance of 40 mm nearby the ground end. The clean surface also shows curve undulations because of the individual lines cross the insulator at more than one points. These undulations are accompanied by electric field reveal over the insulator. For wet polluted conditions, the water droplets hit the top of the polluted surface and local variations in the resistive current can occur. This behaviour may redistribute the voltage profile and extremely high field can be initiated.

3.2. Electric Field Distribution

Figure 5 and Figure 6 show respectively the plot results of field distributions along the porcelain and glass insulators under dry clean and wet polluted surface conditions. The simulated field was

represented the tangential electric field along the insulator surface. The graphs, in general, exhibit a similar tendency of field distributions along the surface profiles. Peaks can be observed in the rate of change of the tangential field at both HV and ground ends. These peaks confirmed the equipotential results concerning the high field regions. Under wet polluted condition, the tangential field attained on both surfaces was higher compared with the dry clean case. The highest field recorded was near to the metal fittings with magnitude value of 3.2 kV/cm. However, away from the metal fittings along the surface distance of the insulators, the trend of the electric field was reduced to a lower value.

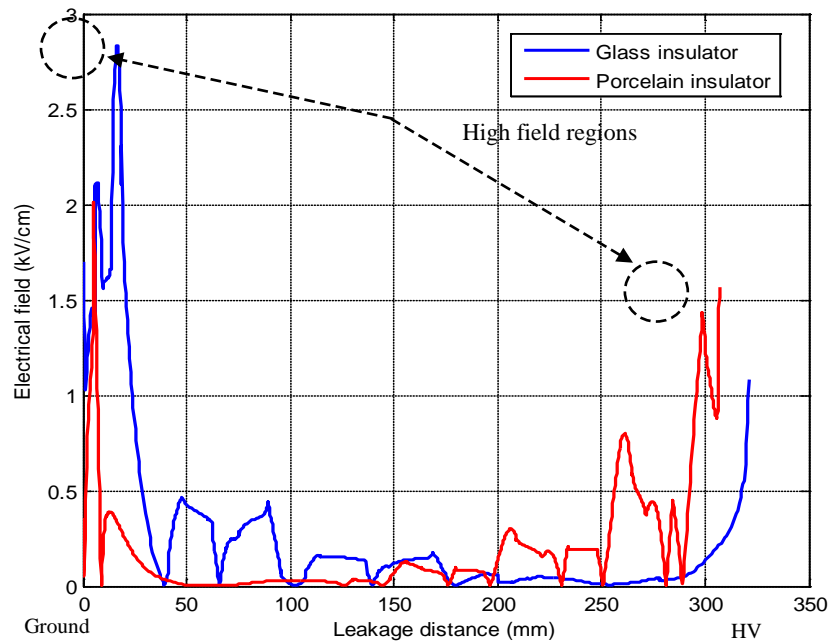


Figure 5: Field distributions over the surface of porcelain and glass insulators under dry clean condition

Porcelain insulator exhibit a significant increase in the field near to the HV terminal compared with the glass. This can be observed under both dry clean and wet polluted conditions. Therefore, the presence of the pollution layer can increase the possibility of the electric field at the insulator surface and this may lead to the surface heating and eventually to the flashover.

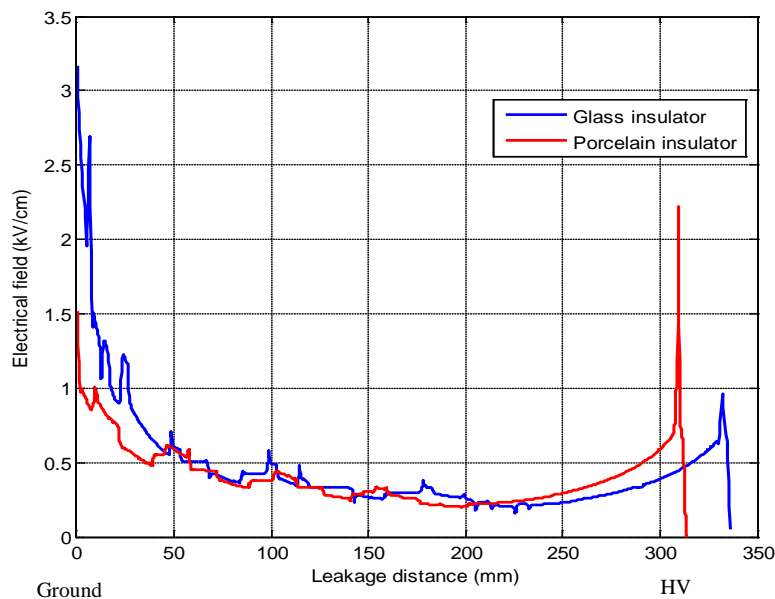


Figure 6: Field distributions over the surface of porcelain and glass insulators under wet polluted condition

4. Conclusions

The electrical performance of porcelain and glass insulators was investigated in this paper. The potential and field distributions over the insulator surfaces were studied using the Finite Element Method COMSOL Multiphysics Software. An ideal model has been adopted for an easily simulation the laboratory test conditions. The tangential field was performed on the insulator surfaces for both dry clean and wet polluted conditions. The result reveals that the highly field region was observed on the polluted insulators as expected. At the high voltage end region where is the extremely field stress, glass insulator offers better electrical performance compared with the porcelain. These all useful information might be worth to understand the insulator properties and to choose an appropriate design.

References

- [1]. J. S. T. Looms. *Insulators for High Voltages*. London, United Kingdom: Peter Peregrinus Ltd, 1988, pp. 2-12. R. S. Gorur, E. A. Cherney, and J. T. Burnham, *Outdoor Insulators*, Ravi S. Gorur, Inc., Phoenix, Arizona, USA, 1999.
- [2]. S. Chakravorti and H. Steinbigler, "Boundary element studies on insulator shape and electric field around HV insulators with or without pollution," *IEEE Transactions on Dielectrics and Electrical Insulation*, vol.7, no.2, pp.169-176, Apr 2000.
- [3]. S. Krzma, M. Albano, and A. Haddad, "Comparative performance of 11kV silicone rubber insulators using artificial pollution tests," in 2015 50th International Universities Power Engineering Conference (UPEC), Stoke On Trent, United Kingdom, pp. 1-6, 2015.
- [4]. CIGRE Taskforce 33.04.01: "Polluted insulators: review of current knowledge," CIGRE technical brochure 158, June 2000.

- [5]. S. Krzma, M. Albano, and A. Haddad, “*Flashover influence of fog rate on the characteristics of polluted silicone rubber insulators,*” in 2017 52th International Universities Power Engineering Conference (UPEC), Crete, Greece, pp. 1–6, 2017.
- [6]. J. L. Rasolonjanahary, L. Krahenbuhl, and A. Nicolas, “*Computation of electric fields and potential on polluted insulators using a boundary element method,*” *IEEE Transactions on Magnetics*, vol.28, no.2, pp.1473-1476, Mar 1992.
- [7]. M. Albano, A. S. Krzma, R. T. Waters, H. Griffiths, and A. Haddad, “*Artificial pollution layer characterization on conventional and textured silicone-rubber insulators,*” in The 19th International Symposium on High Voltage Engineering (ISH), Pilsen, Czech Republic, 2015.
- [8]. IEC 60507:2013, ‘*Artificial pollution tests on high-voltage ceramic and glass insulators to be used on a.c. systems*’, 3rd edition.
- [9]. COMSOL Multiphysics User's Manual," ed: Version 5.2.

Long Term Peak Load Forecasting for the Libyan Network

Mahmoud Y. Khamaira¹, Adnan S. Krzma², A. M. Alnass³

¹mykhamaira@Elmergib.edu.ly, ²ASkrzma@Elmergib.edu.ly, ³A.Alnass@gmail.com

^{1,2,3}Department of Electrical and Computer Engineering, Faculty of Engineering, Elmergib University, Libya

ABSTRACT

Long term load demand forecasting is a necessary process in electric power system operation and development. It contains the accurate prediction of both magnitudes and geographical locations of electric load over the different periods of the planning horizon. Several economic implications of power utility such as economic scheduling of generating capacity, scheduling of fuel purchases, security analysis, planning of power development, maintenance scheduling and dispatching of generation units are mainly worked based on accurate load forecasting. In this paper, the peak load for seven years ahead is performed for the Libyan electric network with the simple regression method. MATLAB programming has been used for computational work. The results attained are validated with the real data obtained from the National Control Center of the General Electricity Company of Libya (GECOL).

Keyword— Long term load forecasting, Simple regression, Libyan network

1. Introduction

Global electricity demand is expected to growth by 85% in 2040 as living standards increase, economies expand and the requirement for electrification of society continues [1]. Electricity demand calculating plays a vital role in load allocation and scheduling for future generation facilities and transmission development. Load demand in a given season is subject to a range of uncertainties, comprising population growth, climate change and economic circumstances. Furthermore, historical data are significance in demand predicting. Load forecasting can be divided into three categories: short-term forecasts, medium-term forecasts and long term forecasts. Short-term forecasts are usually from one hour to one week. They play an important role in the day-to-day operations of a utility such as unit commitment, economic dispatch and load management. A short term electricity demand forecast is commonly mentioned to as an hourly load prediction. Medium-term forecasts are usually from a several weeks to a few months and even up to a one year. They are necessary in planning fuel procurement, scheduling unit maintenance and energy trading and revenue assessment for the utilities. A medium-term forecast is commonly referred to as the monthly load forecast. Long-term electricity demand forecasting is a crucial part in the electric power system planning, tariff regulation and energy trading [2]. A long-term forecast is required to be valid from 5 to 25 years. This type of forecast is used to deciding on the system generation and transmission expansion plans. A long term forecast is generally known as an annual peak load [1].

This work offers an uncomplicated technique to forecast the future peak demand for the Libyan electric network. The offered technique might be useful to determine the powerful energy management strategy so as to meet the required load demand at minimum operating cost. In addition, the factors affecting load patterns are presented.

2. Factors Affecting Load Patterns

A large number of factors influence the load demand considerably. The effects of all these factors which affect the load need to be studied in order to improve an accurate load forecasting model.

2.1. Economic factor

Several economic factors such as the type of customers such as residential, agricultural, commercial and industrial, demographic conditions, population, GDP growth, national economic growth and social activities etc. can cause a significant variation in the load pattern. These economic factors generally affect the long-term load forecasting.

2.2. Weather Factors

Load forecasting is significantly affected by weather conditions such as temperature (dry and wet temperature), humidity, cloud coverage etc. The most essential weather factor is the temperature. The variations considerably affect the load requirement for heating in winter and air conditioning in summer. Load forecasting also affected by other factors such as humidity especially in hot and humid areas, wind speed and light intensity of the day [3].

2.3. Time and Seasonal Factors

Time factors play an important role in accurate load forecasting. It may cause a considerable change in load pattern. There are following factors;

- Seasonal variation: change of season (summer, winter, rainy and autumn), change of day light hours, change of average temperature, etc.
- Daily variation: different day time and night time consumption
- Weekly cycle: Different weekday and weekend consumption patterns
- Holidays and special days: Load pattern on holidays will be different from that of weekdays and weekend. Special days such as festive days can affect the load.

2.4. Price Factor

Load forecasting is strongly affected by electricity price. Electrical price which may have a complicated relationship with the system load, it is an important factor in load forecasting. Change in tariff may also change the load pattern.

2.5. Random Disturbances

A random disturbance happens in the power system which may disturb the load pattern considerably. The random disturbances include sudden shutdown or start of industries, wide spread strikes, marriages, special functions etc. [4].

2.6. Other Factors

In addition to all the factors listed above, the load pattern may also change due to geographical condition (urban or rural areas), type of consumers (rural or urban), home appliances sale data, television program (sports, serial etc.) etc. [3]

3. Literature Survey

Generally, long-term load demand forecasting methods can be classified in to two categories: artificial intelligence based methods and parametric methods [5]. The artificial intelligence based methods are further classified in to neural networks [6-10] support vector machines [11], genetic algorithms [12], wavelet networks [13, 14], fuzzy logics [15] and expert system [16] methods. The parametric methods are based on relating load demand to its affecting factors by a mathematical model. The model parameters are estimated using statistical techniques on historical data of load and it's affecting factors. Parametric load forecasting methods can be generally categorized under three approaches: regression methods, time series prediction methods [17]. Traditional statistical load demand forecasting techniques or parametric methods have been used in practice for a long time. These traditional methods can be combined using weighted multi-model forecasting techniques, showing adequate results in practical system. These methods cannot properly present the complex nonlinear relationships that exist between the load and factors that influence on it [18].

4. Simple Linear Regression

A regression model is a statistical procedure that allows a researcher to estimate the linear relationship that relates two or more variables. This linear relationship summarizes the amount of change in one variable that is associated with change in another variable or variables. However, the straight line connecting any two variables X (independent variable) and Y (dependent variable) can be stated algebraically as [19];

$$Y = \beta_0 + \beta_1 X + \varepsilon \quad (1)$$

where β_0 and β_1 are two unknown constants that represent the intercept and slope, known as coefficients, and ε is the error term. Given some estimates $\hat{\beta}_0$ and $\hat{\beta}_1$ for the model coefficients, the future values can be predicted as following;

$$\hat{y} = \hat{\beta}_0 + \hat{\beta}_1 x \quad (2)$$

where \hat{y} indicates a prediction of Y on the basis of $X = x$. The hat symbol denotes an estimated value.

Let $\hat{y} = \hat{\beta}_0 + \hat{\beta}_1 x_i$ be the prediction for Y based on the i th value of X. Then $e_i = y_i - \hat{y}_i$ represents the i th residual.

The residual sum of squares (RSS) is defined as;

$$RSS = e^2_1 + e^2_2 + \dots + e^2_n \quad (3)$$

The least squares approach chooses $\hat{\beta}_0$ and $\hat{\beta}_1$ to minimize the RSS. The minimizing values can be shown to be;

$$\hat{\beta}_1 = \frac{\sum_{i=1}^n (x_i - \bar{x})(y_i - \bar{y})}{\sum_{i=1}^n (x_i - \bar{x})^2} \quad (4)$$

$$\hat{\beta}_0 = \bar{y} - \hat{\beta}_1 \bar{x} \quad (5)$$

Where $\bar{y} = \frac{1}{n} \sum_{i=1}^n y_i$ and $\bar{x} = \frac{1}{n} \sum_{i=1}^n x_i$ are the sample means.

4.1. Assessing the Overall Accuracy of the Model

For making sure that used model is giving a good relationship between the considered variables, the Residual Standard Error (R2) can be calculated as follows [19];

$$R^2 = \frac{\text{Residual sum of squares}}{\text{Total sum of squares}} = 1 - \frac{\sum_{i=1}^n (y_i - \hat{y}_i)^2}{\sum_{i=1}^n (y_i - \bar{y})^2} \quad (6)$$

The minimum value for R^2 is 0. This would occur when there is no relationship between the two variables, so that X does not help at all in explaining the differences in values of Y. The maximum possible value for R^2 is 1. This would occur when the two variables are perfectly related, so that the observed values of Y exactly correspond with the predicted values from the regression line, and there are no prediction errors. This would mean a perfect goodness of fit.

5. Model Implementation

In this section, a regression model will be performed for forecasting the future peak load for the Libyan network. Data, that used to prepare the forecasted model, are as shown in the Table 1.

According to the historical data available for the peak load as shown in table 1, it is noticed that during the period (2000-2010) the growth rate is different than that in the period (2013-2017) and this due to the situation during the period (2011-2012). This difference of the growth rate that dropped from 5760 MW to 5515 MW and then jumped to 5981 MW, makes it difficult to perform a model that gives an accurate expectation, if the whole period is considered at once, therefore, the period from (2000-2017) is divided according to the growth rate. The first period from (2000-2010), and the second one is (2013-2017), and each period is considered as a case study.

Table 1: Historical data

Year	Population n $x_i * 10^6$	Peak load (MW) Y_{actual}
2000	4.83	2630
2001	4.93	2934
2002	5.02	3081
2003	5.12	3341
2004	5.22	3612
2005	5.32	3857
2006	5.42	4005
2007	5.53	4420
2008	5.60	4756
2009	5.74	5282
2010	5.86	5760
2011	5.97	5515

2012	6.08	5981
2013	6.20	6520
2014	6.33	6600
2015	6.45	6750
2016	6.57	7017
2017	6.70	7383

5.1. Case1 (period 2000-2010)

In this case the historical data for the period (2000-2010) is only considered to achieve a forecasting model. The population is considered an independent variable (x_i) and the historical peak load is a dependent variable Y_i . As the regression model coefficient (β_0, β_1) can be calculated from equations 5 and 6, the forecasting model can be rewritten as following;

$$\hat{y} = -11669 + 0.0029 * x_i \quad (7)$$

From equation 7 the Residual Standard Error (R) also can be calculated;

$$R^2 = 0.996$$

Where;

\hat{y} = expected peak load

x_i = expected number of the population

As the predicated number of the population is available, the future peak load can be estimated from equation 8 as shown in the Table 2 and figure 1.

Table 2: Results for case 1

Year	$x_i * 10^6$	$Y_{actual}(Mw)$	$\hat{y}(Mw)$
2000	4.83	2630	2.5133
2001	4.93	2934	2.8069
2002	5.02	3081	3.0712
2003	5.12	3341	3.3648
2004	5.22	3612	3.6584
2005	5.32	3857	3.9520
2006	5.42	4005	4.2457
2007	5.53	4420	4.5687
2008	5.60	4756	4.7742
2009	5.74	5282	5.1853
2010	5.86	5760	5.5376
2011	5.97		
2012	6.09		
2013	6.20		
2014	6.33		
2015	6.45		
2016	6.57		

2017	6.70		
2018	6.83		8386
2019	6.96		8768
2020	7.10		9179
2021	7.24		9590
2022	7.38		10001
2023	7.52		10412
2024	7.66		10823
2025	7.81		11263

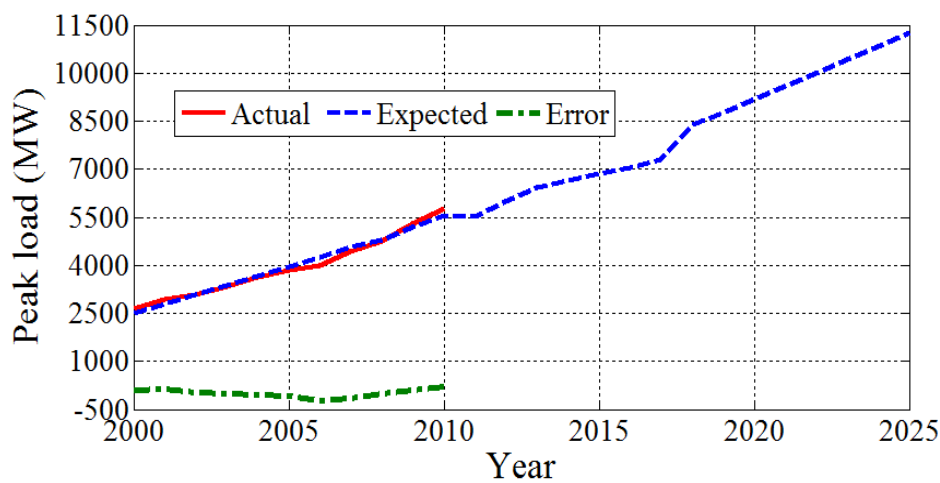


Figure 1: Results for case 1

5.2. Case 2 (period 2013-2017)

In this case the historical data for the period (2013-2017) is only considered for performing a forecasting model and the same procedure that was used in the first case is done. The forecasting regression model and the R^2 for this case can be written as following:

$$\hat{y} = -4292.6 + 0.0017 * x_i \tag{8}$$

$$R^2 = 0.998$$

Table 3: Results for case 2

Year	$x_i * 10^6$	Y_{actual} (Mw)	\hat{y} (Mw)
2013	6.20	6520	6.422
2014	6.33	6600	6.6466
2015	6.45	6750	6.854
2016	6.57	7017	7.0614
2017	6.70	7383	7.286
2018	6.83		7510.7
2019	6.96		7735.4

2020	7.10		7977.3
2021	7.24		8219.2
2022	7.38		8461.2
2023	7.52		8703.1
2024	7.66		8945.1
2025	7.81		9204.3

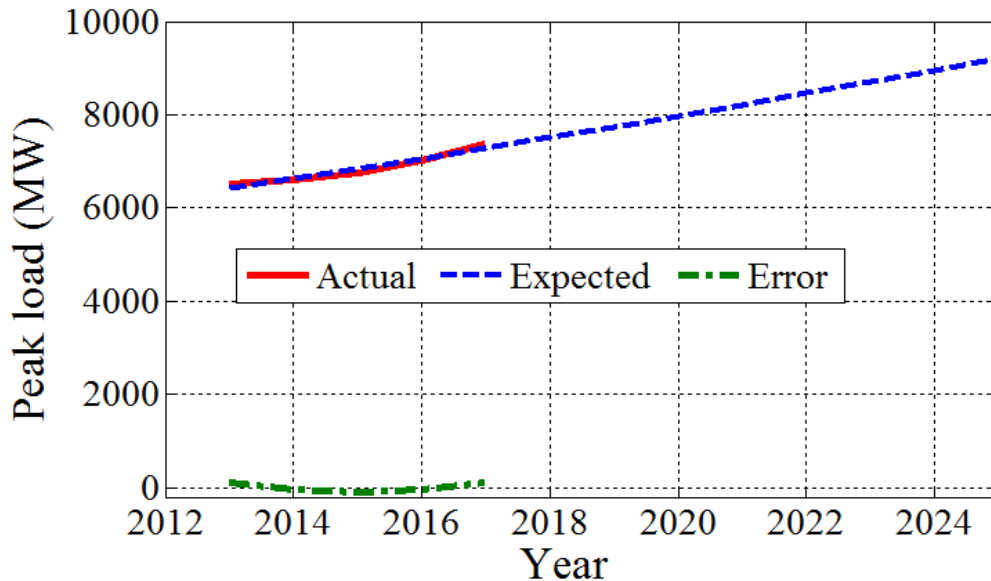


Figure 2: Results for case 2

6. Discussion of Results

The simple linear regression method was applied to the peak load from 2000 to 2013. After the SLR was explained, it was used in two cases to forecast the peak load from 2018 to 2025. The results attained for case1 are summarized in the Table 1 and illustrated as graphic form in the figure 1. The data used are the annual peak loads and the population number recorded between years 2000 and 2010. It can be seen from results that the expected peak load at 2025 will be about 11263 Mw. On the other side, results for the case 2 are displayed in the Table 2 and demonstrated as graphic form in the figure 2. Data used are the annual peak loads and the population number recorded between years 2013 and 2017. It can also be also seen from the Table 2 that for case 2 the expected peak load will be around 9204.3 Mw.

7. Conclusions

Electric load predicting considers a vital part in the economic optimization and secure operation of electric power systems. It represents the first step in developing future generation, transmission, and distribution facilities. In this paper, the main factors that affect the accuracy of the load forecasts are presented and the annual peak load for seven years ahead is expected for the Libyan electric network.

Results demonstrate that proposed method can be used as a good technique for long term load forecasting with minimum error.

Acknowledgment

The authors express their deep gratitude and thanks to engineers of the National Control Centre for the General Electricity Company of Libya for their valuable help and cooperation in this work.

References

- [1]. N. Phuangpornpitak, and W. Prommee, "A Study of Load Demand Forecasting Models in Electric Power System Operation and Planning,"GMSARN International Journal 10 (2016) 19 – 24.
- [2]. Pessanha, J.F.M., and Leon, "Forecasting Long-term Electricity Demand in the Residential Sector," Procedia Computer Science, 2015, 55, 529-38.
- [3]. G. Singh, D.S. Chauhan, A.Chandel, D.Parashar, and G. Sharma, "Factor Affecting Elements and Short term Load forecasting Based on Multiple Linear Regression Method," International Journal of Engineering Research & Technology, Vol. 3, Issue 12, December-2014.
- [4]. Mahmoud Y. Khamaira, Adnan S. Krzma, A. M. Alnass, and I. R. Jaba, "Modeling and Forecasting Short-Term Electricity Demand for Libyan Electric Network," The International Journal Of Engineering And Information Technology (IJEIT), VOL.4, NO.2, JUNE 2018.
- [5]. L. Ghods, and M. Kalantar, "Different Methods of Long-Term Electric Load Demand Forecasting; A Comprehensive Review,"Iranian Journal of Electrical & Electronic Engineering, Vol. 7, No. 4, Dec. 2011.
- [6]. Al Mamun M., and Negasaka K., "Artificial neural networks applied to long-term electricity demand forecasting,"Proceedings of the Fourth International Conference on Hybrid Intelligent Systems, pp. 204-209, Dec. 2004.
- [7]. Dang Khoa T. Q., and Oanh P. T., "Application of Elman and neural wavelet network to long-term load forecasting," ISEE Journal, track 3, sec. B, No. 20, pp. 1-6, 2005.
- [8]. Negasaka K., and Al Mamun M., "Long-term peak demand prediction of 9 Japanese power utilities using radial basis function networks," IEEE Power Engineering Society General Meeting, Vol. 1, pp. 315-322, 6-10 June 2004.
- [9]. Taradar H. M., and Kashtiban A. M., "Application of neural networks in power systems; A review," Transaction of Engineering, Computing and Technology, Vol. 6, No. 1, ISSN 1305-5313, pp. 53-57, June 2005.
- [10]. Kermanshahi B. S., and Iwamiya H., "Up to year 2020 load forecasting using neural nets," Electric Power System Research, Vol. 24, No. 9, pp. 789-797, 2002.
- [11]. Pai P.-F., and Hong W. C., "Forecasting regional electricity load based on recurrent support vector machines with genetic algorithms," Electric Power System Research, Vol. 74, No. 3, pp. 417-425, 2005.
- [12]. EL_Naggar K. M., and AL-Rumaih K. A., "Electric load forecasting using genetic based algorithm, optimal filter estimator and least error square technique: Comparative study," Transaction of Engineering, Computing and Technology, Vol. 6, pp. 138-142, ISSN 1305- 5313, June 2005.
- [13]. Khoa T. Q., Phuong L. M., Binh P. T., and Lien N. T. H., "Application of wavelet and neural network to long-term load forecasting," International Conference on Power System Technology, pp. 840-844, Singapore, 21-24 November 2004.

- [14]. Khoa T. Q., Phuong L. M., Binh P. T. , and Lien N. T. H., “Power load forecasting algorithm based on wavelet packet analysis,” International Conference on Power System Technology, pp. 987-990, Singapore, 21- 24 November 2004.
- [15]. Faraht M. A., “Long-term industrial load forecasting and planning using neural networks technique and fuzzy interface method,” 39th International Universities Power Engineering Conference, UPEC 2004, Vol. 1, pp. 368-372, 2004.
- [16]. Kandil M. S., El-Debeiky S. M., and Hasanien N. E., “The implementation of long-term forecasting strategies using a knowledge-based expert system: part-II,” Electric Power System Research, Vol. 58, No. 1, pp. 19-25, 2001.
- [17]. Al-Hamidi H. M., and Soliman S. A., “Longterm/mid-term electric load forecasting based on short-term correlation and annual growth,” Electric Power System Research, Vol. 74, No. 3, pp. 353-361, June 2005.
- [18]. Dang Khoa T. Q., and Oanh P. T., “Application of Elman and neural wavelet network to long-term load forecasting,” ISEE Journal, track 3, sec. B, No. 20, pp. 1-6, 2005.
- [19]. John O. R., Sastry G. P., and David A. D., “Applied Regression Analysis: A Research Tool,” Second Edition, Springer, 1998.

THD Investigation of Hybrid Cascaded Multilevel Inverter

Alseddig Elzowawi¹, Islam Saad², Mustafa Elsherif³

¹ Alseddig.Elzowawi@eng.misuratau.edu.ly, ² islam.saad@eng.misuratau.edu.ly,

³ M.A.elsherif@misuratau.edu.ly

^{1, 2, 3} Department of electrical and electronic engineering, Faculty of Engineering, Misurata University, Libya

ABSTRACT

Hybrid cascaded multilevel (HCML) inverter is a modification of the cascaded H-bridge (CHB) inverter, where this inverter has overcome the main drawback of the CHB inverter, which is the connection of a separate DC source in each H-bridge (cell). The solution was connecting one DC source in the first cell, and capacitors in the rest of the cells. Therefore, by controlling the switches of the inverter, the voltages of the capacitors can be regulated at a certain level and the inverter can generate an alternating voltage. In this paper, two cells and three cells HCML inverters have been simulated with PLECS software and modulated with phase shift- pulse width modulation strategy (PS-PWM). This modulation scheme was implemented with C language. The modulation program considers the load current and the voltages of the capacitors as feedbacks. The two inverters have been investigated in terms of the total harmonic distortion (THD) of the voltage and current waveforms. Therefore, the effect of the load sizes and cells number was addressed. Several significant results have been obtained from this study.

Keyword— CHB inverter, HCML Inverter, PS-PWM, THD.

1. Introduction

Cascaded multilevel inverter has become the solution for many renewable energy and motor drive applications due to the considerable advantages. The simplified topology (HCML inverter) has overcome the need to connect a separate DC source in every H-bridge. Therefore, it can suit a wider range of applications in the industry sector as the cost and the size of the inverter are reduced [1, 2, 3]. A growing body of literature has investigated different aspects of this significant inverter. However, one of the major areas of study is the total harmonic distortion in the output voltage and current waveforms generated by the inverter. As the THD content affects the power quality delivered to the load [4, 5, 6]. In [5] selective harmonic elimination pulse width modulation was suggested to modulate the considered inverters, where the THD was decreased by 10%. In this paper, the methodology used to investigate the THD content in the output waveforms was based on simulation processes. Two inverters with different cells number have been modeled and simulated with PLECS software. Thus, the number of cells and the load components (resistance and inductance) have been considered to explore their impacts on the THD of the output voltage and the load current. Based on that, several scenarios have been studied and compared with each other to understand the effect of the above factors on the THD content.

2. Connecting the Inverters

In order to examine the effect of the load and cells number on the total harmonic distortion content in the output waveforms of the hybrid cascaded multilevel inverter, Two cells and three cells HCML inverters have been built and simulated with PLECS software. The two cells inverter has two H-bridge cells. The first cell has four IGBTs switches connected to a 100 V DC source. The second cell has four IGBTs switches connected to a capacitor. Then the load was connected in parallel with the two cells as shown in Figure 1.

Furthermore, the three cell inverter has three H-bridge cells. The first cell has four IGBTs switches connected to a 100 V DC source. However, the second and the third cells have four IGBTs switches and connected to two capacitors as depicted in Figure 2. Therefore, the capacitors will replace the DC source in the second and third cells. Hence, by regulating the voltage of the capacitors at the level of 100 V, the inverters will generate alternating voltage with maximum voltage of 200V for two cells inverter with 5-level output voltage (200, 100, 0, -100, -200), whereas, 300V for three cells inverter with 7-level output voltage (300, 200, 100, 0, -100, -200, -300). Regulation process needs a modulation scheme that can provide the proper switching states for all switches. On the other hand, it needs to synthesize the right output voltage waveform with minimum THD.

For the two cells inverter, the capacitor value was 3.5mF, the load resistance was 0.5 Ω , and the load inductance was 0.03H. However, for the three cells inverter, the two capacitors values were 4 mF, the load resistance was 1.11 Ω , and the load inductance was 0.056H. The values of these parameters were selected based on the performance of the inverters, where these values offer the best operation and output waveforms.

3. Implementing PS-PWM Strategy

Phase Shift PWM (PS-PWM) is tremendously common in the industrial applications particularly for CHB inverter. It is able to reduce the harmonics in the output, distributes the power equally between the H-bridges. PS-PWM was developed from the traditional sinusoidal PWM schemes especially for CHB inverters, where this scheme is based on multiple carriers (triangle wave carriers) compared with only one modulation signal. Each carrier is assigned to a certain H-bridge with a phase shift between the carriers.[7] Therefore, Phase shift-pulse width modulation was employed to modulate the two considered inverters. This modulation strategy was implemented in PLECS software by using C-script block. This block contains a programme written with C language, where the programme controls every process in the inverter. However, the main tasks of the C code are to generate the modulation pulses for all the switches and balance the voltages of the capacitors. Maintaining the capacitors voltages requires measuring the voltages of the capacitors and load current and feed them back to the programme, so that the code can understand the case of the capacitors and take the decision whether to charge or discharge them depending on their voltages and the sign of the load current.

3.1. Modulating the Two Cells Inverter

The C-script block has 5 input signals, one modulation wave (sine wave) with 50 Hz and 0.8V amplitude. Two carrier waves (triangle waves) with 250 Hz and 1V amplitude, each carrier was assigned to one cell. Besides, the voltage of the capacitor was measured and fed back to the block as an input, and the load current was also measured and fed to the this block. Therefore, in order to maintain the capacitor voltage at a certain level, the C language programme has to read the values of the capacitor voltage and the load current, so that it can select the right switching states for the inverter's switches.

The two triangle carriers have a phase shift between them and that phase shift was calculated by using the following equation [8]:

Phase shift angle $\theta_k = [(k-1)/N] \times 180$

$$(1) \text{Phaseshiftangle}(\theta_k) = \frac{K-1}{N} * 180$$

Where:

θ_k is the phase shift angle for each cell.

k is the individual number of the cell.

N is the total number of the cells.

Therefore, the calculated phase shift angles are $\theta_{HB1} = 0^\circ$, $\theta_{HB2} = 90^\circ$. On the other hand, to enter these angles into Plocs software, they must be changed to time base on the following equation [8]:

$$\text{Phase shift time } T_k = [(k-1)/N] \times T_s / 2 \quad (2)$$

Where:

T_k is the phase shift time for each cell.

k is the individual number of the cell.

N is the total number of the cells.

T_s is the carrier frequency inverse.

Therefore, the phase shift times between the carrier signals were obtained $T_{HB1} = 0$ sec, $T_{HB2} = 0.001$ sec. Moreover, C-script block has 8 outputs, one output for every switch in the two H-bridges as can be seen in Figure 1.

3.2. Modulating the Three Cells Inverter

As this inverter has three H-bridges, so it contains one capacitor in the second and one capacitor in the third cell. Therefore, the input signals of the C-script are 7. One sine wave (50Hz, 0.8V), three triangles waves (250Hz, 1V), two feedback voltage signals of both measured capacitors voltages and one feedback load current. The phase shift between the three carriers are $\theta_{HB1} = 0^\circ$, $\theta_{HB2} = 60^\circ$, $\theta_{HB3} = 120^\circ$, while the phase shift times are $T_{HB1} = 0$ sec, $T_{HB2} = 0.000667$ sec, $T_{HB3} = 0.00133$ sec. For the outputs, there are 12 output signals exiting the C- script, one output for every switch in the three cells, as clearly depicted in Figure 2.

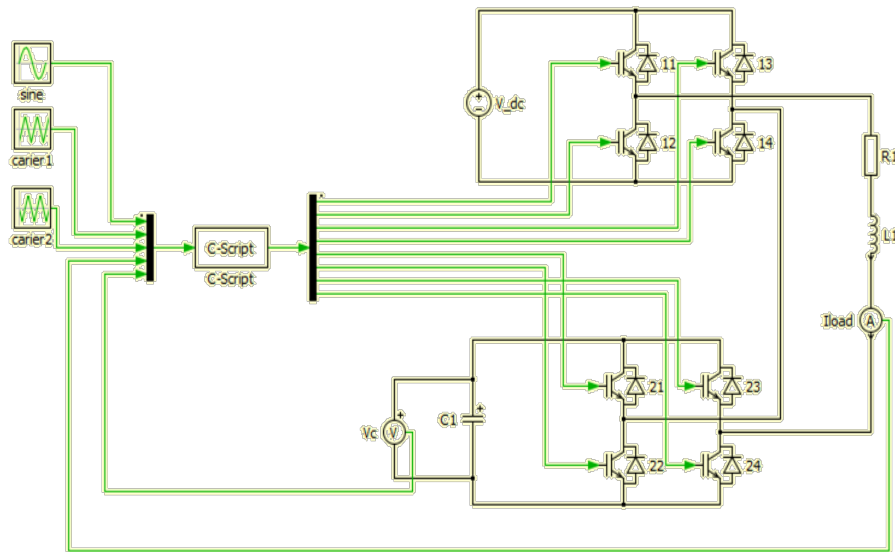


Figure 1: Two cells HCML inverter circuit

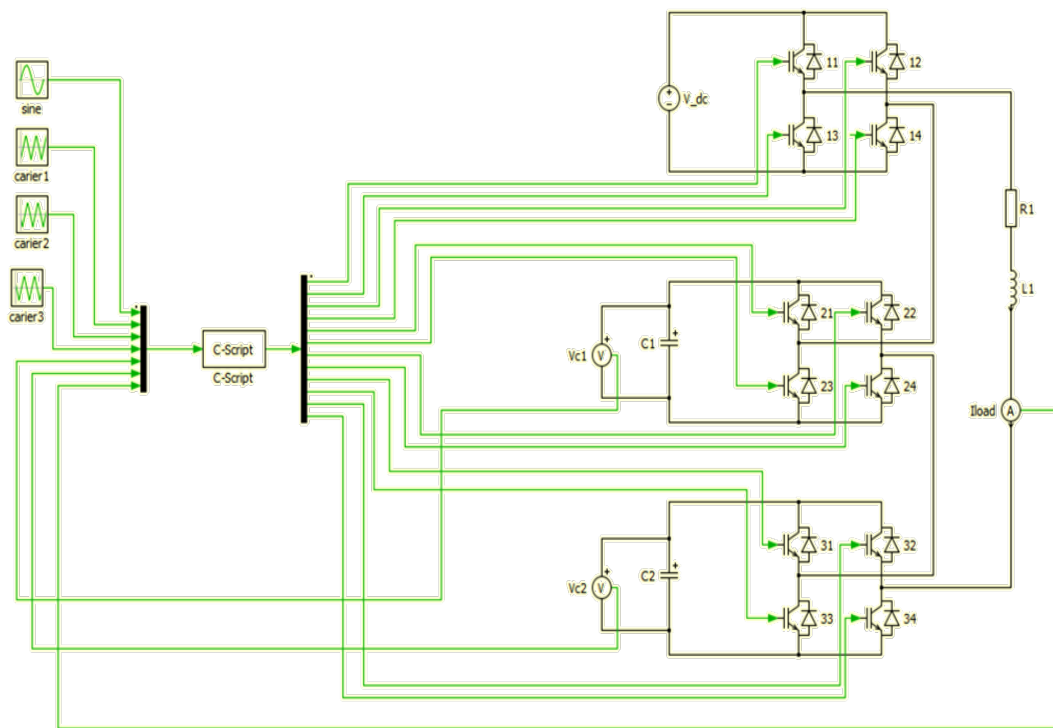


Figure 2: Three cells HCML inverter circuit

4. THD Study of the Two Inverters

In this section, the THD contents are studied in the output waveforms of the two inverters, where the inverters have been simulated under diverse resistance and inductance values. As one parameter was changing while the other was kept constant. At the same time, the THD readings of the output

voltage and the load current were taken during the test at each time the parameter changes. Therefore, several THD readings have been recorded with each scenario.

4.1. THD Study under Load Resistance Effect

In this case, the impact of the load resistance on the THD was investigated. The resistance value was changed, while the other parameters of the inverter remained constant as mentioned above. Then, the THD readings were recorded as can be seen in Tables 1 and 2.

Table 1: THD readings when changing the load resistance (two cells inverter)

R (Ω)	THD _v %	THD _I %
0.1	35.98	1.64
0.5	35.83	1.60
0.9	35.79	1.59
1.2	35.78	1.58
1.8	35.76	1.58
2.4	35.75	1.58
2.9	35.71	1.57

Table 2: THD readings when changing the load resistance (three cells inverter)

R (Ω)	THD _v %	THD _I %
0.1	25.22	2.07
0.5	25.13	0.99
0.9	24.97	0.87
1.11	24.95	0.86
1.15	24.82	0.85
1.20	24.64	0.81
1.25	24.59	0.77

Tables 1 and 2 present the results obtained from the simulation of the first scenario, where the effect of the load resistance was examined. It can be seen from the data that the THD of the voltage is larger than that of the current. This could be due to the switching frequency of the switches and due to the smoothing effect of the load inductance for the current. Moreover, the THD of both the output voltage and the load current were relatively decreasing with increasing the resistance value. This may be attributed to the decreasing of the load current value, which in turn reducing the discharging current from the capacitor. The data shown in tables 1 and 2 were plotted in Figures 3 and 4 respectively. These two figures confirm that clear trend of decreasing of both THDs.

On the other hand, both THDs for three cells inverter are less than that of the two cells inverter. This was caused by the higher number of cells which led to synthesize more voltage steps (7 levels) in the output voltage in the three cell inverter, thus, the output voltage became closer to the sine wave. Consequently, as the cells number increases, the output voltage will have less THD.

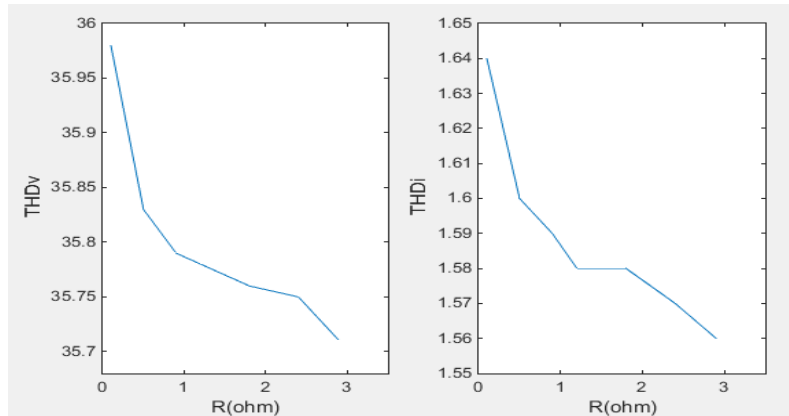


Figure 3: THD readings when load resistance changing for two cells inverter

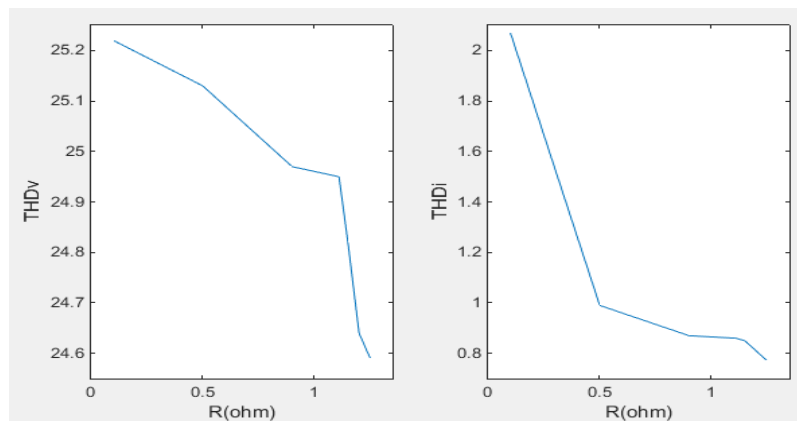


Figure 4: THD readings when load resistance changing for three cells inverter

4.2. THD Study under Load Inductance Effect

Another major factor that significantly affects the THD contents in the output waveforms, that element is the inductance of the load. Therefore, its impact was studied in this simulation scenario. The inductance value was varied while the other parameters of the inverters kept untouched. Lower and higher inductance values than that values mentioned in section 2 were tested to recognise how the load inductance influences the THD contents of the HCML inverter. A number of readings have been taken according to these values as revealed in tables 3 and 4.

Table 3: THD readings when changing the load inductance (two cells inverter)

L (H)	THD _v %	THD _i %
0.01	35.83	1.62
0.03	35.84	1.58
0.05	35.86	1.56
0.07	35.89	1.51
0.09	35.93	1.47

0.10	36.00	1.42
0.15	35.71	1.57

Table 4: THD readings when changing the load inductance (three cells inverter)

L (H)	THD _v %	THD _i %
0.01	24.49	2.57
0.035	24.63	1.04
0.056	24.95	0.96
0.09	25.08	0.89
0.12	25.11	0.81
0.15	25.17	0.74
0.20	25.21	0.63

From the tables above, it is apparent that as the inductance value was increased, the THD of the output voltage was increasing too. This could be explained by the reducing power factor as the inductance increases, where the resistance value was remained constant. However, the THD of the load current was decreasing as the inductance value was increasing, which is due to the smoothing effect of the inductance for the current. Furthermore, the THD of both the voltage and the current in the case of three cell inverter is less than that of the two cells inverter. This is similar to the result of the resistance effect. Therefore, the cells number is a vital factor that can widely improve the THD contents in the voltage and current waveforms. As a result, the cells number is an independent factor from the resistance and inductance of the load, where as the number of cells increases, the THD content decreases. However, the cells number is limited by the size, cost and the modulating technique [9]. The data presented in table 3 and 4 were plotted as shown in Figure 5 and 6.

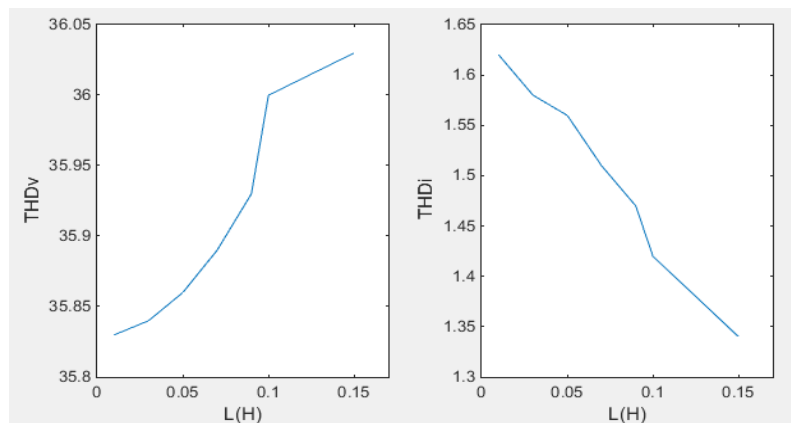


Figure 5: THD readings when load inductance changing for two cells inverter

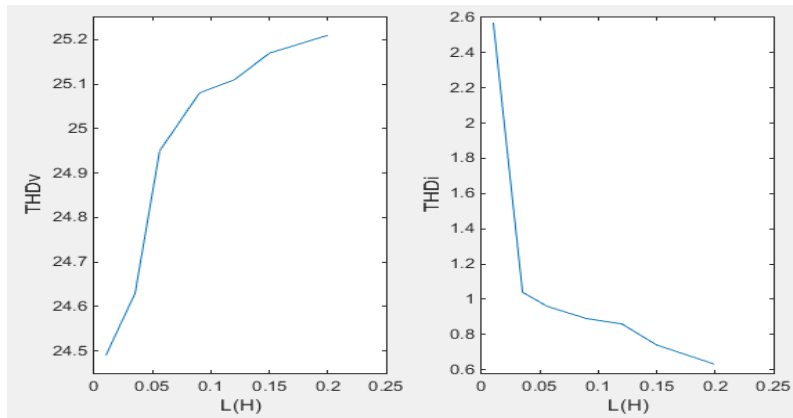


Figure 6: THD readings when load inductance changing for three cells inverter

5. Conclusions

A simulation investigation of the THD content was presented. Two cells and three cells hybrid cascaded multilevel inverters have successfully been modelled by PLECS software and simulated under various conditions. The resistance and inductance of the load have a serious impact on the THD of both the output voltage and current. For the resistance effect, it reduces the THD contents of both waveforms. However, the inductance has a different effect on both the voltage and the current. It deteriorates the voltage but improves the current. As a result, the design of the inverter should carefully consider the load, so that the inverter can operate at a wide range of loads with minimum THD contents. The cells number as an enhancing effect of both waveforms, but, it is a limited solution when it comes to the size and the cost of the inverter. Since the number of devices will be high.

References

- [1]. H. Liu, L. M. Tolbert, B. Ozpineci, and Z. Du, "Hybrid Multilevel Inverter With Single DC Source," *Midwest Symp. Circuits Syst.*, pp. 538–541, 2008.
- [2]. T. A. Lipo, "A Hybrid Multilevel Inverter Topology For Drive Applications A Hybrid Multilevel Inverter Topology For Drive Applications," no. May, 2014.
- [3]. L. M. Tolbert, F. Z. Peng, T. Cunningham, and J. N. Chiasson, "Charge Balance Control Schemes For Cascade Multilevel Converter In Hybrid Electric Vehicles," *IEEE Trans. Ind. Electron.*, vol. 49, no. 5, pp. 1058–1064, 2002.
- [4]. N. Shrivastava and A. P. Mehta, "Survey on Harmonic Mitigation Techniques in Multilevel Inverters," vol. 3, no. 12, pp. 4307–4311, 2014.
- [5]. P. Tamilvani and K. R. Valluvan, "Harmonic Mitigation in Various Levels of Multilevel Inverter with Different Loads," vol. 2, no. 9, pp. 1989–1996, 2014.
- [6]. A. Papriwal and A. Mahor, "Mitigation Of Harmonics In Inverter," vol. 2, no. 9, pp. 98–105, 2012.
- [7]. M. Malinowski, K. Gopakumar, J. Rodriguez, and M. A. Perez, "A Survey on Cascaded Multilevel Inverters," *Ind. Electron. IEEE Trans.*, vol. 57, no. 7, pp. 2197–2206, 2010.
- [8]. J. Rodriguez *et al.*, "Multilevel Converters: An Enabling Technology for High-Power Applications,"



- Proc. IEEE*, vol. 97, no. 11, pp. 1786–1817, 2009.
- [9]. Y.-M. Park, H.-S. Ryu, H.-W. Lee, M.-G. Jung, and S.-H. Lee, “Design of a Cascaded H-Bridge Multilevel Inverter Based on Power Electronics Building Blocks and Control for High Performance,” *J. Power Electron.*, vol. 10, no. 3, pp. 262–269, 2010.

Impact of Wind Generation Location on Power System Losses

I.S.Naser

ibr.naser@sebhau.edu.ly

Department of Renewable Energy, College of Mining and Energy, Sebha University, Libya

ABSTRACT

The global environmental and renewable energy initiatives have led to an increased connection of wind generation to the electricity power networks, the increase in wind generation makes a significant impact on the power system and planning for both customers and electricity suppliers. This paper investigates the impact of wind generation location in power system losses when connected at the transmission network. The doubly-fed induction generator (DFIG) and different connection scenarios are used to investigate the impact. Finally, some conclusions that provide a better understanding of the behavior of wind generator when connected to strong bus or weak bus. The Power World Simulator is used to obtain simulated results.

Keyword— Wind generation, DFIG, Transmission network, Real system losses.

1. Introduction

The increasing interest in producing electricity using renewable resources is growing rapidly due to ability of these resources to reduce greenhouse gases [1]. In some remote areas economic factor could be a major one. One of the most prevalent and desirable technologies is wind power. Wind power has been dramatic development throughout the World especially, connected to both distribution and transmission system. Recently wind generator have been experiencing a rapid development and the size of wind turbines and wind farms are increasing, and the impact of wind generation on power system operation is more important [2]. The pattern and size of the wind turbine and generator is based on the wind characteristics. Wind generation can be divided into several types depending on the design of the rotor and generator, and wind generation can be a resource for both active and reactive power. Wind turbine generators can be modelled into two categories: a fixed speed with induction generator, and a variable speed generator in PQ or PV mode.

In general, increased wind penetration level will have the impacts on the operation of the system, and the effect is becoming increasing. These impacts could be positive or negative depend on a number of factors, including wind power penetration level, type wind generator, geographical dispersion of wind generation and the size of the electrical networks [3]. Connecting a wind generator to a network can have negative effects, such as a new loading situation and changed power flow direction. Integration of a wind farm into a network can also affect the power losses and stability of the system [4]. The impact of wind generation on the distribution system has been studied and. it show that wind generation integrated on the distribution system can improve overall system voltage profile and at the same time system losses are reduced [5-6].

The objective of this paper is to investigate the impact of DFIG location based wind generation on system MWh losses in transmission system. The IEEE 30-bus system is used as a test case, simulated using the Power World Simulator, and wind penetration level is varied from 20% to 30% to assess

the impact on power system MWh losses. For the studies carried out in this paper, only focus on variable speed unit (DFIG) and modelled as PV bus, this farm is operated from 0.95 PF for Q_{max} and 0.95 PF for Q_{min} .

2. Doubly Fed Induction Generator

This configuration consists of a wound rotor induction generator where the stator windings are directly connected to the grid and the rotor windings are connected to a back-to-back power converter. This back-to-back power converter is dimensioned for partial generator power and is able to operate bi-directionally. It uses a wound rotor induction generator with slip rings to take current into or out of the rotor winding, and variable speed operation is obtained by injecting the controllable voltage into the generator rotor at slip frequency [7].

As shown in Figure 1 the rotor winding is fed through the variable frequency power converter, typically based on two AC/DC insulated gate bipolar transistor (IGBT) based voltage source converters (VSC) linked by the DC bus. The power converter decouples the network electrical frequency from the rotor mechanical frequency, enabling the variable speed operation of the wind turbine. The voltage source converter (VSC) produces an AC voltage that is controllable in magnitude and phase, similar to the synchronous generator or synchronous compensator. The VSC commutates independently of the AC-side voltage and consequently it can be used on the load-only system. This makes the VSC useful for rotor connection, wind farm connection and so forth. Converters (C1) and (C2) in Figure 1 are used to control the doubly fed induction generator wind turbine. A number of manufacturers use converter (C1) to provide torque/speed control, together with terminal voltage or power factor control for the overall system. Converter (C2) is used to maintain the DC link voltage and provide the path for power to flow to and from the AC system at unity power factor.

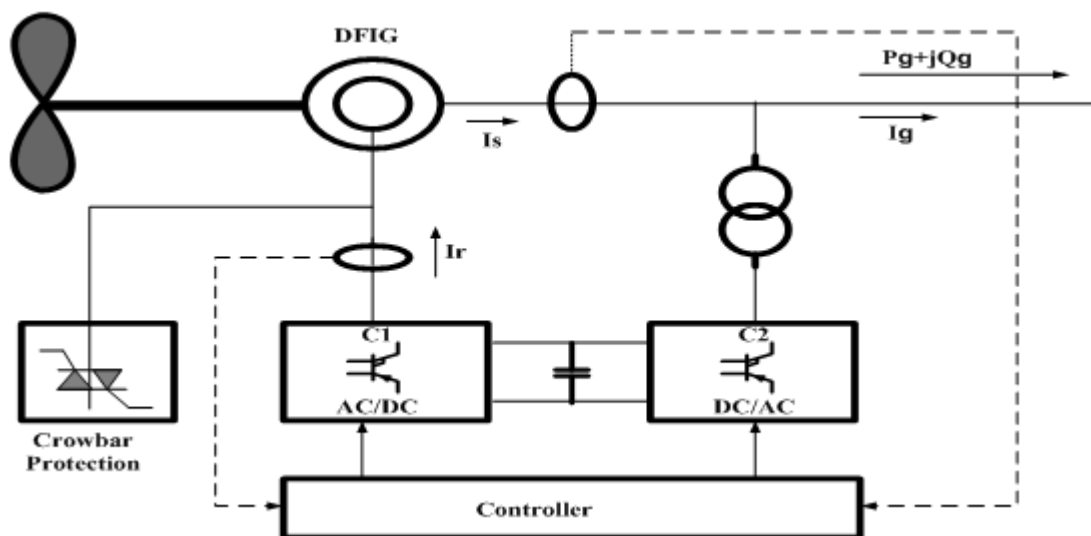


Figure 1: Typical configuration of the DFIG wind turbine

3. Doubly Fed Induction Generator Model.

Recent grid codes demand from wind farms to provide reactive output regulation, often in response to power system voltage, much as the conventional power generations. Manufacturers offer different options for var generation by DFIG based wind turbines in steady state operation. The reactive power requirements are related to the characteristics of each network. DFIG can be modelled in load flow studies as PQ or PV buses, so as to operate in power factor controlled or voltage controlled modes [8]. When the DFIG is modelled as a PQ bus, the DFIG is usually employed as a unity power factor (P.F) operation (zero reactive power output) though other (P.F) values can be specified (e.g, from 0.95 leading to 0.95 lagging). In voltage controlled mode, the DFIG is modelled as PV bus with Q limits applied. In this mode, a stator Q is varied to maintain the voltage at the point of common coupling within given reference values (in this case voltage is controlled at 1.0 p.u). For the studies carried out in this paper, only focus on variable speed unit (DFIG) and modelled as PV bus Q_{min} .

4. Test system and simulation results

A modified IEEE30-bus is modelled in PowerWorldSimulator and it used as the test system [9]. The test system consists of six generators which supply power to twenty one loads through 132/33 kV substation, the modified test system is analysed using optimal power flow (OPF). Wind farms are connected at different buses at different penetration levels of wind generation with different scenarios. For the studies carried out in this paper, only focus on variable speed unit (DFIG) and modelled as PV bus. A single-line diagram of IEEE-30 bus system is shown in Figure 2.

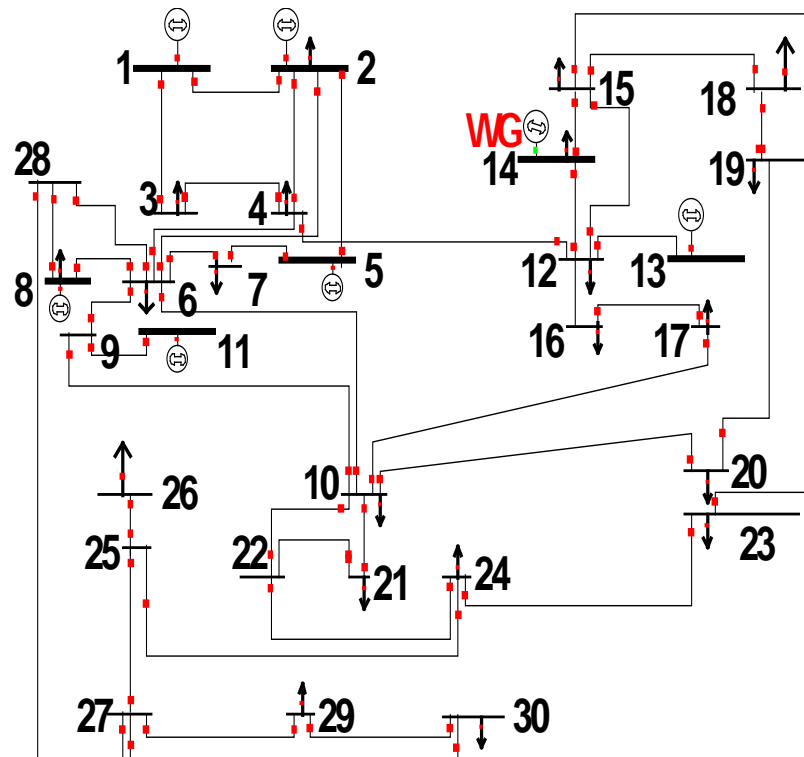


Figure 2: The modified IEEE-30 bus test system

An analysis method is used to assess a system loss that considers the time varying characteristics of the power system generation components, penetration level of wind generation, and the variable nature of wind power, using the time step option in the Power World Simulator. The analysis method has three major inputs. The wind power input is the time series values of the wind generation connected to the network in MW at one hour intervals. These data were obtained from a utility operating in the United Kingdom from a wind farm for a one day period and at one hour intervals. Table 1 shows the wind power input data for 20% and 30% penetration levels with a one day load period [10]. The input of the conventional generators is their availability considering their capacity and quantity, while the load model input is the forecasted load profile applied to the network for the evaluation of system losses.

Table 1: Wind power input data for different wind penetration with one day load period

Time (Hour)	Total Loads (MW)	20% WP (200 MW)	30% WP (300 MW)
01:00:00	283.4	24.96	55.5
02:00:00	283.4	57.7	37
03:00:00	302.5	174.5	100.5
04:00:00	302.5	162.4	8
05:00:00	358.8	104.3	91
06:00:00	358.8	45.6	275.5
07:00:00	500	119.4	165.2
08:00:00	500	190.2	5.5
09:00:00	615.5	164.4	35.7
10:00:00	615.5	143.4	167.4
11:00:00	454.6	84.7	15.3
12:00:00	454.6	54.2	110.5
13:00:00	504.3	97.9	80.7
14:00:00	504.3	200	12.5
15:00:00	745.5	157	6.5
16:00:00	745.5	123.2	285.7
17:00:00	850.1	200	300
18:00:00	850.1	96.4	7.5
19:00:00	695	130.5	0
20:00:00	695	38.2	12.4
21:00:00	450	13.5	113.6
22:00:00	450	43.8	176.3
23:00:00	314.9	30.2	165.1
00:00:00	314.9	70.1	35.9

The objective of connecting wind generation at different locations is to investigate the effect of location site on the total system MWh losses. There are three wind farm connection scenarios: a strong area at bus 28 (case 1), a weak area at bus 14 (case 2), and two locations at buses 6 and 28 as dispersion of wind generation (case3). The total system MWh losses are analysed for two different wind generation levels (20% and 30%). The results presented here are for a 24 hour period. The total system MWh losses of the network are calculated for every one hour of the simulation and are recorded. As shown in Figure 3, the value of the total system MW losses decrease with the connection of wind generation from 149.48 MW at the peak load period in the case of no wind generation to 80.06 MW for the connection case 1 (one wind farm is connected to a strong bus 28), 84.89 MW for the connection case 3 (two wind farms are connected to buses 6 and 28) and 129.6 MW as one wind farm is connected to a weak bus 14 when the percentage of wind capacity was 20% (200 MW). It can be seen that for 20% wind penetration level, the total system real power losses are reduced significantly for both wind connection scenarios compared to the base case. From a total system real power loss point of view, a single wind farm being connected to a strong bus is a better option and will reduce the total real power losses more than other connection scenarios.

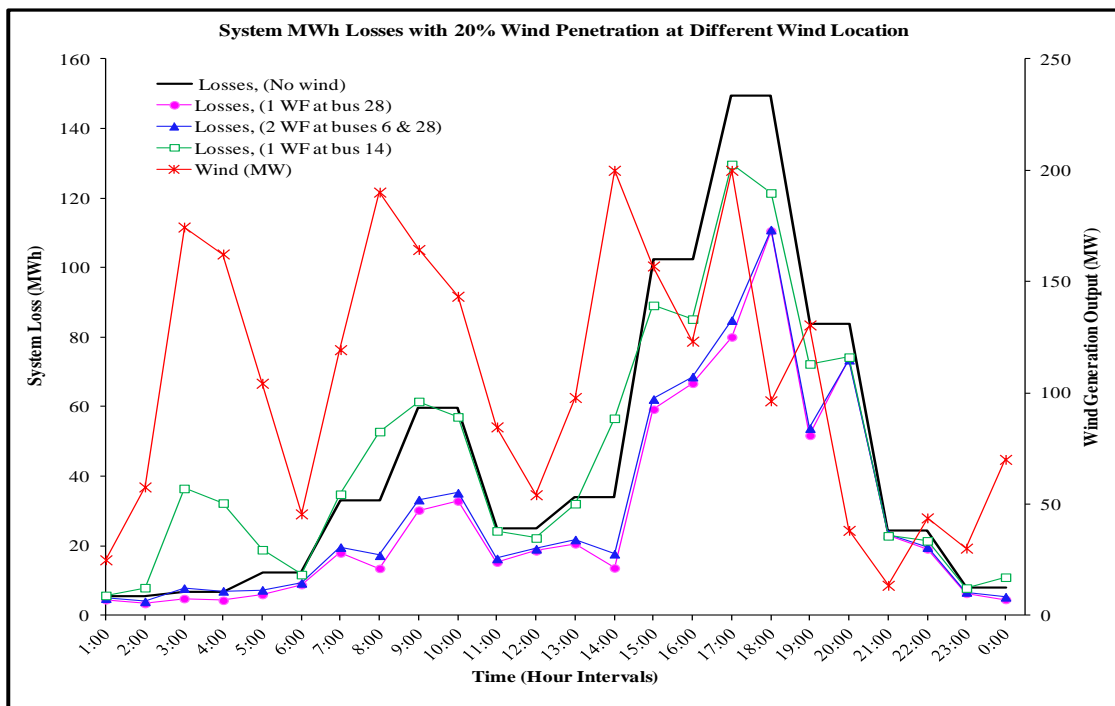


Figure 3: The total system MWh losses of IEEE-30 bus system with 20% wind penetration level, when wind farm is connected to the network at different connection scenarios.

When the wind penetration level increases from 20% to 30%, the total system MW losses are reduced more for both wind connection scenarios (for one strong location and for multiple locations) compared to the base case and when the wind generation is 30% (300 MW). The system MW losses are recorded as 59.4 MW when the wind farm is connected to the strong bus and 62 MW

for 2 wind locations. The system witnesses a significant reduction in system MW losses for higher wind penetration levels as the system becomes more heavily loaded, as shown in Figure 4. However, when the wind penetration level, connected to weak bus 14, increases to 30%, the total system MW losses are increased to 166.1 MW, which is a slight increase compared to the no wind case (149.48 MW). This means that a higher wind penetration might increase the total system MW losses during system load ability (at the peak load) when the wind farm is connected to a weak area.

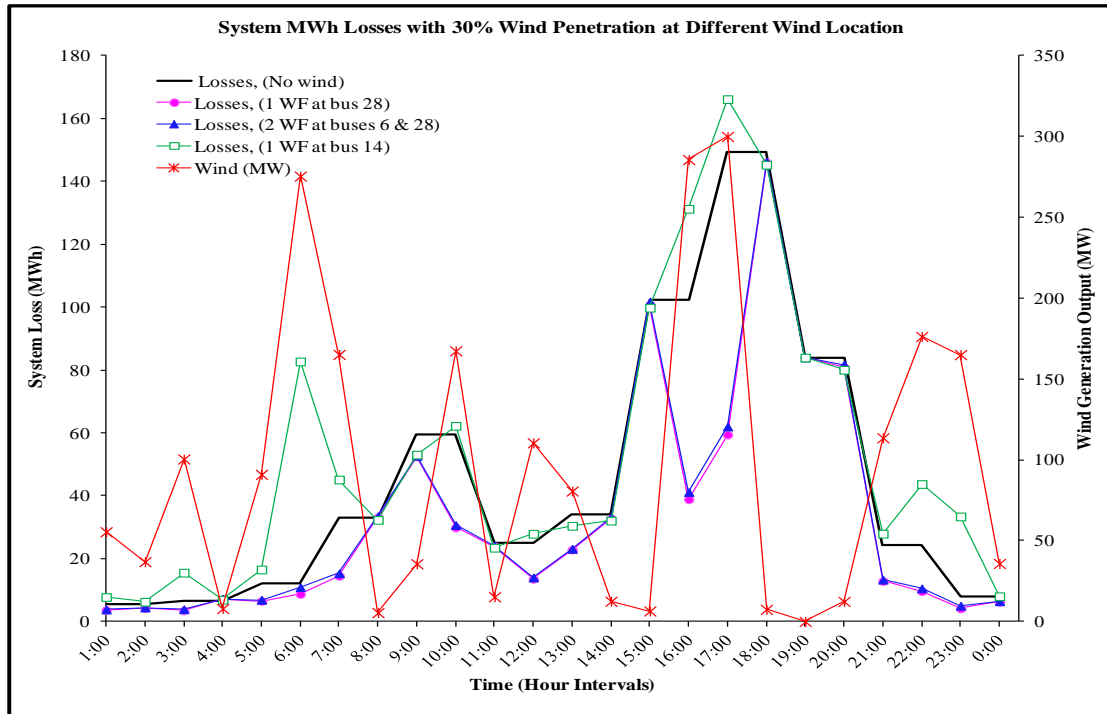


Figure 4: The total system MWh losses of IEEE-30 bus system with 30% wind penetration level, when wind farm is connected to the network at different connection scenarios.

5. Conclusions

This paper has investigated the impact of wind generation location on the total system MW losses based on system load ability in the transmission network. A DFIG based wind farm with a voltage controlled mode was integrated into an IEEE-30 bus system. Different connection scenarios of wind farms were considered; a single location (a strong bus and a weak bus) and dispersion of wind farms in two locations. Different penetration levels of wind generations were used. The results show that a single strong location for a wind farm with higher wind penetration levels can achieve a significant reduction in the total system MW losses when the system loading is high. However, the results show that total real power losses increase if the wind farm is located at a weak area with higher wind penetration levels when the system is highly loaded.

References

- [1]. Federico Milano, "Assessing adequate voltage stability analysis tools for networks with high wind power penetration," IEEE DRPT Conference, 6-9 April 2008, Nanjing, China, pp.2492-2497
- [2]. I.S.Naser, M.A.Alsharif, MN.Hussin, M.A. Alrmah "Evaluating the impact of wind generation on transmission network power losses", LICEET 2018, Libya
- [3]. I.S. Naser, Olimpo Anaya-Lara, K. L. Lo, "Study of the Impact of Wind Generation on Voltage Stability in Transmission Networks," IEEE DRPT, The 4th International Conference on Electric Utility Deregulation and Restructuring and Power Technologies. 6th-9th July, 2011, Shandong, China
- [4]. L. T. Ha, T. K. Saha, "Investigation of Power Loss and Voltage Stability Limits for Large Wind Farm Connections to a Subtransmission Network", IEEE Power Engineering Society General Meeting, Colorado, USA, June 2004.
- [5]. P. Agalgaonkar, S.V. Kulkarni, S. A. Khaparde, "Impact of Wind Generation on Losses and Voltage Profile in a Distribution System", 86 Conference on Convergent Technologies for Asia-Pacific Region, TENCON 2003, Vol. 2, pp.775-779.
- [6]. K.C Divya, P. S. Nagendra Rao, "Models for Wind Turbine Generating Systems and Their Application in Load Flow Studies", ELSEVIER, Electric Power Systems Research Vol. 76, 2006, pp. 844-856.
- [7]. L. Holdsworth, X. G. Wu, J. R. Ekanayake, N. Jenkins, "Comparison of Fixed-Speed and Doubly-Fed Induction Wind Turbine during Disturbances", IEE Proceedings Part C, 150 (3), pp.343-352, 2003.
- [8]. N. R. Ullah, T. Thiringer, "Variable Speed Wind Turbines for Power System Stability Enhancement", IEEE Transactions on Energy Conversion, Vol. 22, No. 1, pp. 52-60, March 2007.
- [9]. "Power Systems Test Case Archive" available from: <http://www.ee.washington.edu/research/psca/>
- [10]. UKGDS, "United Kingdom Generic Distribution System" 2009, available from: [http://www.sedg.ac.uk/UKGDS Networks. pdf](http://www.sedg.ac.uk/UKGDS_Networks.pdf).

Antenna Elevation Control using Multiple Switched Self-Tuning Controllers Design

Ahmed M. Alnajeh ¹, Othman E. Aburas ², Youssef Amer Arebi ³

1aalnajeh@yahoo.com, 2aburas1981@gmail.com, 3yousef.erpi@yahoo.com

¹Department of Electrical and Computer Engineering, Applied Research and Development Center, Tripoli, Libya.

²Department of Electrical and Computer Engineering, Faculty of Engineering Alkhoms, Elmergib University, Libya.

³Department of Electrical and Computer Engineering, Advanced Center of Technology, Tripoli, Libya.

ABSTRACT

Adaptive controllers have a lot of advantages over conventional ones, especially when the model of the plant to be controlled is unknown or changes with time. This paper proposes a control scheme for multiple adaptive Self-Tuning Pole-Placement controllers using both the classical technique via transfer function and the modern technique using discrete state-space. This approach enables the user to switch between the classical and modern techniques in order to control the estimated plant model on-line; the switching mechanism ensures a smooth transition amongst the two pole-placement controllers.

The performance of the proposed control scheme on the closed-loop performance of an antenna system, controlling its elevation, is demonstrated. Simulation results demonstrating the effectiveness of the switching mechanism between different controllers are presented. A Graphical User Interface is built to facilitate the controller programming and allowing the simulation of multiple adaptive controllers.

Keyword— Adaptive Self-Tuning Control, Discrete State-Space, Pole-Placement Control, Antenna Elevation Control.

1. Introduction

Control systems design techniques typically require an in-depth understanding of the plant under study and its environment. In some applications, however, the plant to be controlled is sophisticated and the involved physical processes are changeable with time and operating conditions. To deal with such situations, different approaches of adaptive control are proposed to tune the controller parameters and behavior in response to the physical processes changes [1]. Self-tuning controllers represent an important class of adaptive control since they provides systematic and flexible approaches for dealing with many difficulties including time varying parameters, non-linearity, and uncertainties. Recently, there has been increasing interest in pole-placement self-tuning controllers due to the fact that in the regulator case, they provide mechanisms to overcome the restriction to minimum phase plants of some optimal controllers. In the servo case, they give the ability to directly introduce the natural angular frequency ω_n and damping ratio ζ as tuning parameters. Moreover, robustness is an essential advantage of pole-placement methods, as they simply modify the system dynamics instead of cancelling them as applied in optimal self-tuning controller [2]. However, the main drawbacks of self-tuning pole-placement controller are based on transfer function approach and also their inability to regulate steady-state error in the presence of constant disturbances. The transfer function approach depends on polynomial algorithms, which are slow to emerge [3]. In

contrast, the linear algebraic tools that are required by state-space techniques are a lot more advanced and more suitable for optimal control design [1][4]. Therefore, the state-space technique is preferred over the transfer function approach, especially for multivariable and non-linear systems[5]. The main contribution of this paper is to develop a control scheme for multiple adaptive Self-Tuning Pole-Placement controllers using both the classical technique via transfer function and the modern technique using discrete state-space framework. In order to assess the performance of the proposed scheme, it is applied to single-input-single-output of an antenna model.

2. A Servomechanism for an Antenna Elevation Control

It is desired to control the elevation of an antenna designed to track a geostationary satellite as sketched in Figure 1. The antenna and drive parts have a moment of inertia J' and damping B_r arising to some extent from bearings and aerodynamic friction, but mostly from the back emf (V) of the DC-drive motor [6,7,8].

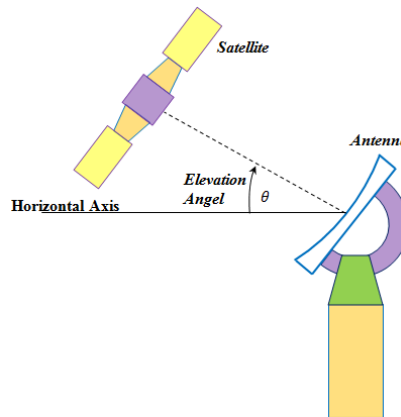


Figure 1: Schematic Diagram of Antenna System

Figure 2 shows the internal connection of DC-drive motor with the antenna system. Here, the armature inductance $L_a(H)$ is negligible because it is usually small. The continuous transfer function [7], [8] can be given by:

$$\theta(s) = \frac{a}{s(s+a)} [U(s) + \xi'(s)] \quad (1)$$

where $\xi'(s)$ is the torque disturbance due to wind, and $U(s)$ is the torque due to the DC motor.

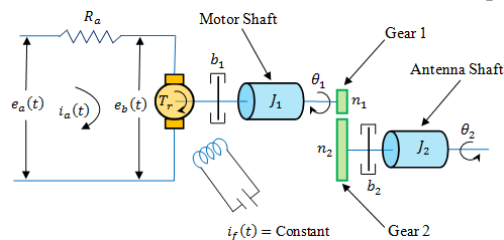


Figure 2: The Connection of DC-drive Motor with the Antenna System

The aim of the design is to measure the error between the angle of the satellite $\theta_s(t)(rad)$ and the antenna $\theta(t)(rad)$ and compute $u(t)$ so that the error e , i.e. equals to $(\theta_s(t) - \theta(t))(rad)$, is always less than $0.001 rad$ during tracking. The geostationary satellite angle that must be followed can be adequately approximated by a fixed velocity.

$$\theta_s(t) = (0.01 rad/sec) \times t(sec).$$

The discrete model of the Antenna system can be written as:

$$\theta(z) = \frac{(aT_s - 1 + e^{-aT_s})z + (1 - e^{-aT_s} - aT_s e^{-aT_s})}{a(z-1)(z - e^{-aT_s})} [U(z) + \xi'(z)] \quad (2)$$

A discrete state-space [9] of antenna tracking control model in which the time constant $a = 0.1$, and $T_s = 1$ sec is:

$$\begin{bmatrix} X_1(t+1) \\ X_2(t+1) \end{bmatrix} = \begin{bmatrix} 0 & 1 \\ -0.9048 & 1.905 \end{bmatrix} \begin{bmatrix} X_1(t) \\ X_2(t) \end{bmatrix} + \begin{bmatrix} 0.04837 \\ 0.13895 \end{bmatrix} u(t) + \begin{bmatrix} 0.04837 \\ 0.13895 \end{bmatrix} \xi' \quad (3)$$

$$y(t) = [1 \quad 0] \begin{bmatrix} X_1(t) \\ X_2(t) \end{bmatrix} \quad (4)$$

In (3), $X_1(t)$ is the position (rad) and $X_2(t)$ is the velocity (rad/sec) of the antenna.

3. Adaptive Control Algorithm

The Controlled Auto-Regressive Moving Average (CARMA) process model [10] is described as:

$$A(z^{-1})y(t) = z^{-k}B(z^{-1})u(t) + C(z^{-1})\xi'(t) \quad (5)$$

Assume that the polynomials $A(z^{-1})$ and $B(z^{-1})$ are co-prime, i.e. they do not have any common factors. Furthermore, $A(z^{-1}), C(z^{-1})$ are monic, i.e. the coefficient of the highest power is unity [11]. The classical pole-placement controller can be described by the following control-law:

$$q(z^{-1})u(t) = H(z^{-1})r(t) - F(z^{-1})y(t) \quad (6)$$

where $q(z^{-1}), F(z^{-1})$ and $H(z^{-1})$ are polynomials in the back shift operator z^{-1} .

The controller has two degrees of freedom, the first is a feed forward with the transfer operator $\frac{H(z^{-1})}{q(z^{-1})}$ and the second is a feedback with the transfer operator $\frac{F(z^{-1})}{q(z^{-1})}$. A block diagram of the closed-loop system is shown in Figure 3. The controller polynomials $H(z^{-1}), F(z^{-1})$ and $q(z^{-1})$ are designed to ensure fast output tracking of the reference signal $r(t)$.

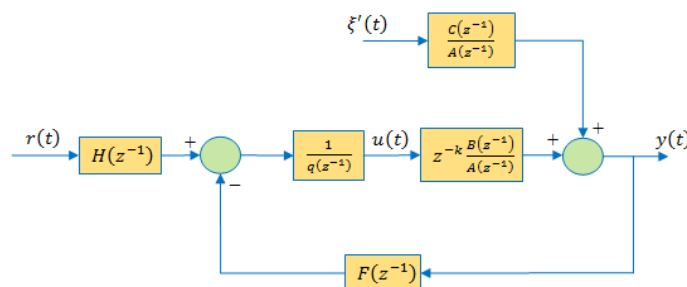


Figure 3: Classical Discrete Pole-Placement Controller

The closed-loop characteristic polynomial of the system (Diophantine equation) is [4]:

$$\mathbf{q}(\mathbf{z}^{-1})\mathbf{A}(\mathbf{z}^{-1}) + \mathbf{z}^{-k}\mathbf{B}(\mathbf{z}^{-1})\mathbf{F}(\mathbf{z}^{-1}) = \mathbf{T}_c(\mathbf{z}^{-1})\mathbf{C}(\mathbf{z}^{-1})$$

(7)

The main concept of the pole placement controller design is to specify the desired closed-loop poles polynomial $\mathbf{T}_c(\mathbf{z}^{-1})$ as a design parameter. By solving the Diophantine equation (7), the polynomials $\mathbf{q}(\mathbf{z}^{-1})$ and $\mathbf{F}(\mathbf{z}^{-1})$ can be obtained. The closed-loop poles polynomial $\mathbf{T}_c(\mathbf{z}^{-1})$ fundamentally determines the property and the performance of the closed system [11].

The desired closed loop poles polynomial $\mathbf{T}_c(\mathbf{z}^{-1})$ and the controller parameters polynomials $\mathbf{F}(\mathbf{z}^{-1})$ and $\mathbf{q}(\mathbf{z}^{-1})$ are expressed in terms of \mathbf{z}^{-1} as follows:

$$\mathbf{F}(\mathbf{z}^{-1}) = \mathbf{f}_0 + \mathbf{f}_1\mathbf{z}^{-1} + \dots + \mathbf{f}_{n_a-1}\mathbf{z}^{-n_f+1} + \mathbf{f}_{n_f}\mathbf{z}^{-n_f}$$

(8)

$$\mathbf{q}(\mathbf{z}^{-1}) = \mathbf{1} + \mathbf{q}_1\mathbf{z}^{-1} + \dots + \mathbf{q}_{n_q-1}\mathbf{z}^{-n_q+1} + \mathbf{q}_{n_q}\mathbf{z}^{-n_q}$$

(9)

$$\mathbf{T}_c(\mathbf{z}^{-1}) = \mathbf{1} + \mathbf{t}_1\mathbf{z}^{-1} + \dots + \mathbf{t}_{n_t-1}\mathbf{z}^{-n_t+1} + \mathbf{t}_{n_t}\mathbf{z}^{-n_t} \quad (10)$$

where, the parameters \mathbf{t}_1 and \mathbf{t}_2 are specified as following [11]:

$$\mathbf{t}_1 = -2\exp(-\zeta\omega_n T_s) \cos(T_s\omega_n\sqrt{1-\zeta^2})$$

$$\mathbf{t}_2 = -2\exp(-\zeta\omega_n T_s)$$

Where ζ and ω_n are respectively the damping ratio and natural angular frequency of the second order closed loop transient response and T_s is the sampling time. In order to have a unique solution, the polynomials $\mathbf{F}(\mathbf{z}^{-1})$, $\mathbf{q}(\mathbf{z}^{-1})$ and $\mathbf{T}_c(\mathbf{z}^{-1})$ in the equations (8), (9), and (10) are specified as follows:

$$\left. \begin{aligned} \mathbf{n}_q &= \mathbf{n}_b + \mathbf{k} - \mathbf{1} \\ \mathbf{n}_f &= \mathbf{n}_a - \mathbf{1} \\ \mathbf{n}_t &\leq \mathbf{n}_a + \mathbf{n}_b + \mathbf{k} - \mathbf{n}_c - \mathbf{1} \end{aligned} \right\}$$

(11)

Substituting Diophantine equation (7) into equation (6), the following equation is obtained:

$$\mathbf{y}(\mathbf{t}) = \frac{\mathbf{z}^{-k}\mathbf{B}(\mathbf{z}^{-1})\mathbf{H}(\mathbf{z}^{-1})}{\mathbf{T}_c(\mathbf{z}^{-1})\mathbf{C}(\mathbf{z}^{-1})}\mathbf{r}(\mathbf{t}) + \frac{\mathbf{q}(\mathbf{z}^{-1})}{\mathbf{T}_c(\mathbf{z}^{-1})}\xi'(\mathbf{t})$$

(12)

It can be seen from equation (12) that the closed loop poles are placed at their pre-specified positions given by the desired closed loop poles polynomial $\mathbf{T}_c(\mathbf{z}^{-1})$ which represents the design parameter. The controller algorithm explained above can be structured as a self-tuning controller as shown in Figure 4. Where, all of the controller's parameters are calculated depending on the change in plant parameters.

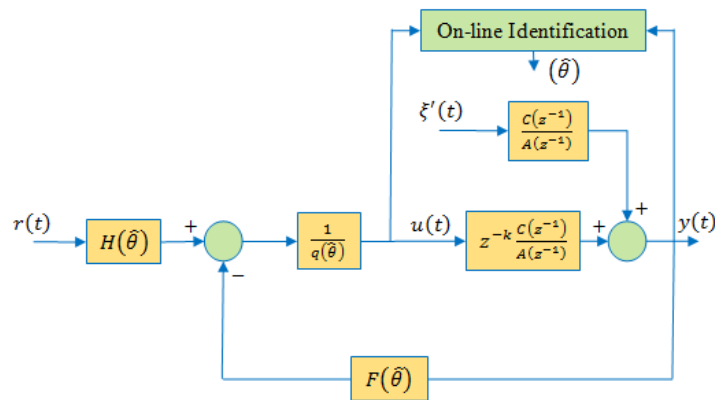


Figure 4: Classical Self-Tuning Pole-Placement Controller

The modern Self-Tuning Pole-Placement using discrete state-space control design algorithm is given in Figure 5, which is based on an on-line observer with a state feedback [6].

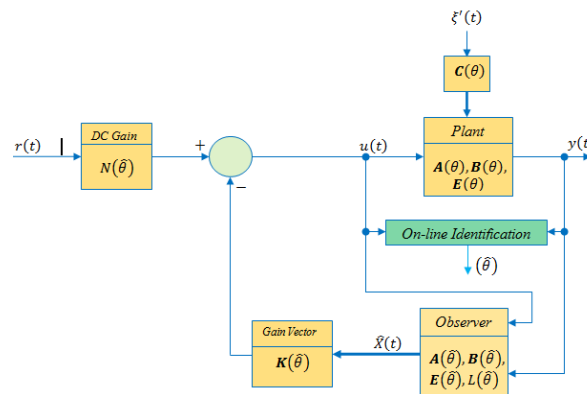


Figure 5: Shows the modern Self-Tuning pole-placement controller.

Both an on-line observer poles and the closed-loop system poles are placed based on the model parameters $\hat{\theta}$ obtained from the on-line identification scheme (RLS or ERLS estimators). In Figure 5, the proper dc gain $N(\hat{\theta})$ is introduced on-line into the design in the presence of reference signal $r(t)$ to eliminate the output steady state error. A discrete state-space model of any system can be derived and presented in discrete matrix-vector equation as follows:

$$\mathbf{X}(t+1) = \mathbf{A}\mathbf{X}(t) + \mathbf{B}\mathbf{u}(t) + \mathbf{C}\xi'(t) \quad (13)$$

$$\mathbf{y}(t) = \mathbf{E}\mathbf{X}(t) + \mathbf{b}_0\mathbf{u}(t) + \xi'(t) \quad (14)$$

The values of both control input signal $\mathbf{u}(t)$ and system output signal $\mathbf{y}(t)$ are read for every sampling instant; these values are used for on-line identification methods such as (RLS or ERLS estimators). An on-line identification method can be used to estimate plant parameters $\hat{\theta}$ which are then used to identify state-space model as:

$$\mathbf{X}(t+1) = \mathbf{A}(\hat{\theta})\mathbf{X}(t) + \mathbf{B}(\hat{\theta})\mathbf{u}(t) + \mathbf{C}(\hat{\theta})\xi'(t) \quad (15)$$

$$\mathbf{y}(t) = \mathbf{E}(\hat{\boldsymbol{\theta}})\mathbf{X}(t)$$

(16)

where, the estimated plant parameters $\hat{\boldsymbol{\theta}} = [-\hat{a}_1 - \hat{a}_2 \cdots - \hat{a}_{n_a} \hat{b}_0 \hat{b}_1 \hat{b}_2 \cdots \hat{b}_{n_b} \hat{c}_1 \hat{c}_2 \cdots \hat{c}_{n_c}]^T$. The matrices of equations (15) and (16) can be placed in either plant framework or observer framework [7].

The transparent controllable canonical form is illustrated as follows:

$$\mathbf{X}(t+1) = \mathbf{A}_c(\hat{\boldsymbol{\theta}})\mathbf{X}(t) + \mathbf{B}_c(\hat{\boldsymbol{\theta}})\mathbf{u}(t) + \mathbf{C}_c(\hat{\boldsymbol{\theta}})\xi'(t)$$

(17)

$$\mathbf{y}(t) = \mathbf{E}_c(\hat{\boldsymbol{\theta}})\mathbf{X}(t)$$

(18)

where:

$$\mathbf{A}_c(\hat{\boldsymbol{\theta}}) = \begin{bmatrix} \mathbf{0} & \mathbf{1} & \mathbf{0} & \cdots & \mathbf{0} \\ \mathbf{0} & \mathbf{0} & \mathbf{1} & \cdots & \mathbf{0} \\ \vdots & \vdots & \vdots & \ddots & \vdots \\ \mathbf{0} & \mathbf{0} & \mathbf{0} & \cdots & \mathbf{1} \\ -\hat{a}_{n_a} & -\hat{a}_{n_a-1} & -\hat{a}_{n_a-2} & \cdots & -\hat{a}_1 \end{bmatrix}, \mathbf{B}_c(\hat{\boldsymbol{\theta}}) = \begin{bmatrix} \mathbf{0} \\ \mathbf{0} \\ \vdots \\ \mathbf{1} \end{bmatrix},$$

$$\mathbf{E}_c(\hat{\boldsymbol{\theta}}) = [\hat{b}_{n_b} \quad \hat{b}_{n_b-1} \quad \cdots \quad \hat{b}_1] \text{ and } \mathbf{C}_c(\hat{\boldsymbol{\theta}}) = [\hat{c}_{n_c} \quad \hat{c}_{n_c-1} \quad \cdots \quad \hat{c}_1]$$

The transparent observable canonical form can be represented as:

$$\mathbf{X}(t+1) = \mathbf{A}_o(\hat{\boldsymbol{\theta}})\mathbf{X}(t) + \mathbf{B}_o(\hat{\boldsymbol{\theta}})\mathbf{u}(t) + \mathbf{C}_o(\hat{\boldsymbol{\theta}})\xi'(t)$$

(19)

$$\mathbf{y}(t) = \mathbf{E}_o(\hat{\boldsymbol{\theta}})\mathbf{X}(t)$$

(20)

Where

$$\mathbf{A}_o(\hat{\boldsymbol{\theta}}) = \begin{bmatrix} \mathbf{0} & \mathbf{0} & \cdots & \mathbf{0} & -\hat{a}_{n_a} \\ \mathbf{1} & \mathbf{0} & \cdots & \mathbf{0} & -\hat{a}_{n_a-1} \\ \vdots & \vdots & \ddots & \vdots & \vdots \\ \mathbf{0} & \mathbf{0} & \cdots & \mathbf{1} & -\hat{a}_1 \end{bmatrix}, \mathbf{B}_o(\hat{\boldsymbol{\theta}}) = \begin{bmatrix} \hat{b}_{n_b} \\ \hat{b}_{n_b-1} \\ \vdots \\ \hat{b}_1 \end{bmatrix}, \mathbf{C}_o(\hat{\boldsymbol{\theta}}) = \begin{bmatrix} \hat{c}_{n_c} \\ \hat{c}_{n_b-1} \\ \vdots \\ \hat{c}_1 \end{bmatrix} \text{ and}$$

$$\mathbf{E}_o(\hat{\boldsymbol{\theta}}) = [\mathbf{0} \quad \mathbf{0} \quad \cdots \quad \mathbf{0} \quad \mathbf{1}]$$

The on-line controller design in discrete state-space based on one framework allows calculating a matrix $\mathbf{T}(\hat{\boldsymbol{\theta}})$ that transforms between canonical frameworks, which is given as:

$$\mathbf{R}_c(\hat{\boldsymbol{\theta}}) = [\mathbf{E}_c(\hat{\boldsymbol{\theta}}) \quad \mathbf{E}_c(\hat{\boldsymbol{\theta}})\mathbf{A}_c(\hat{\boldsymbol{\theta}}) \quad \cdots \quad \mathbf{E}_c(\hat{\boldsymbol{\theta}})\mathbf{A}_c^{n-1}(\hat{\boldsymbol{\theta}})]$$

$$\mathbf{R}_o^{-1}(\hat{\boldsymbol{\theta}}) = \begin{bmatrix} \hat{a}_1 & \hat{a}_2 & \cdots & \hat{a}_{n-1} & \mathbf{1} \\ \hat{a}_2 & \cdots & \hat{a}_{n-1} & \mathbf{1} & \mathbf{0} \\ \vdots & \vdots & \mathbf{1} & \mathbf{0} & \mathbf{0} \\ \hat{a}_{n-1} & \mathbf{1} & \mathbf{0} & \mathbf{0} & \mathbf{0} \\ \mathbf{1} & \mathbf{0} & \mathbf{0} & \mathbf{0} & \mathbf{0} \end{bmatrix}, \mathbf{T}(\hat{\boldsymbol{\theta}}) = \mathbf{R}_o^{-1}(\hat{\boldsymbol{\theta}}) \times \mathbf{R}_c(\hat{\boldsymbol{\theta}})$$

(21)

where, $\mathbf{T}(\hat{\boldsymbol{\theta}})$ is the transformation matrix between transparent canonical frameworks, $\mathbf{R}_c(\hat{\boldsymbol{\theta}})$ is the observability matrix of transparent controllable canonical form and $\mathbf{R}_o^{-1}(\hat{\boldsymbol{\theta}})$ is the inverse observability matrix of transparent observable canonical form.

The estimated state vector $\hat{\mathbf{X}}_c(\mathbf{t})$ of an on-line observer of transparent controllable canonical form (plane framework) can be evaluated as follows:

$$\hat{\mathbf{X}}_c(\mathbf{t} + 1) = \mathbf{A}_c(\hat{\boldsymbol{\theta}})\hat{\mathbf{X}}_c(\mathbf{t}) + \mathbf{L}_c(\hat{\boldsymbol{\theta}}) \left(\mathbf{y}(\mathbf{t}) - \mathbf{E}_c(\hat{\boldsymbol{\theta}})\hat{\mathbf{X}}_c(\mathbf{t}) \right) + \mathbf{B}_c(\hat{\boldsymbol{\theta}})\mathbf{u}(\mathbf{t}) \quad (22)$$

The on-line observer gain matrix $\mathbf{L}(\hat{\boldsymbol{\theta}})$ can be easily calculated by using transparent observable canonical form [7], therefore, the on-line observer gains $\mathbf{L}(\hat{\boldsymbol{\theta}})$ is transformed to transparent controllable canonical form to be used in equation (22) as follows:

$$\mathbf{L}_c(\hat{\boldsymbol{\theta}}) = \mathbf{T} \times \mathbf{L}_o(\hat{\boldsymbol{\theta}}) = \mathbf{T} \times \begin{bmatrix} \mathbf{L}_{o_1}(\hat{\boldsymbol{\theta}}) \\ \mathbf{L}_{o_2}(\hat{\boldsymbol{\theta}}) \\ \vdots \\ \mathbf{L}_{o_n}(\hat{\boldsymbol{\theta}}) \end{bmatrix} = \mathbf{T} \times \begin{bmatrix} \hat{\mathbf{a}}_{n_a} - \boldsymbol{\sigma}_{o(n)} \\ \hat{\mathbf{a}}_{n_a-1} - \boldsymbol{\sigma}_{o(n-1)} \\ \vdots \\ \hat{\mathbf{a}}_1 - \boldsymbol{\sigma}_{o(1)} \end{bmatrix} = \begin{bmatrix} \mathbf{L}_{c_1}(\hat{\boldsymbol{\theta}}) \\ \mathbf{L}_{c_2}(\hat{\boldsymbol{\theta}}) \\ \vdots \\ \mathbf{L}_{c_n}(\hat{\boldsymbol{\theta}}) \end{bmatrix} \quad (23)$$

The equation of the transparent controllable canonical form gain $\mathbf{K}_c(\hat{\boldsymbol{\theta}})$ can be written as:

$$\mathbf{K}_c(\hat{\boldsymbol{\theta}}) = [\mathbf{K}_{c_1}(\hat{\boldsymbol{\theta}}) \quad , \quad \mathbf{K}_{c_2}(\hat{\boldsymbol{\theta}}) \quad \cdots \quad \mathbf{K}_{c_n}(\hat{\boldsymbol{\theta}})] \\ = [\hat{\mathbf{a}}_{n_a} - \boldsymbol{\alpha}_{c(n)} \quad , \quad \hat{\mathbf{a}}_{n_a-1} - \boldsymbol{\alpha}_{c(n-1)} \quad \cdots \quad \hat{\mathbf{a}}_1 - \boldsymbol{\alpha}_{c(1)}] \quad (24)$$

The proper dc gain \mathbf{N} can be calculated as follows:

$$(\mathbf{N}(\hat{\boldsymbol{\theta}}))^{-1} = -\mathbf{E}_c(\hat{\boldsymbol{\theta}})(\mathbf{A}_c(\hat{\boldsymbol{\theta}}) - \mathbf{B}_c(\hat{\boldsymbol{\theta}})\mathbf{K}_c(\hat{\boldsymbol{\theta}}) - \mathbf{I})^{-1}\mathbf{B}_c(\hat{\boldsymbol{\theta}}) \quad (25)$$

Referring to Figure (7), the control-law can be generated as follows:

$$\mathbf{u}(\mathbf{t}) = \mathbf{N}(\hat{\boldsymbol{\theta}})\mathbf{r}(\mathbf{t}) - \mathbf{K}_c(\hat{\boldsymbol{\theta}})\hat{\mathbf{X}}_c(\mathbf{t}) \quad (26)$$

The algorithm of Self-Tuning Observer Pole-placement with Reference Signal and Proper DC Gain can be summarized as follows:

Step 1: Select the desired control-law characteristic equation $\boldsymbol{\alpha}_c(\mathbf{z})$ and the desired observer characteristic equation $\boldsymbol{\sigma}_o(\mathbf{z})$.

Step 2: Read the new values of $\mathbf{y}(\mathbf{t})$ and $\mathbf{u}(\mathbf{t})$.

Step 3: Estimate the process parameters $\hat{\boldsymbol{\theta}}$ using recursive least squares estimator or extended recursive least squares estimator and formulate a state-space model of the plant $\{\mathbf{A}_c(\hat{\boldsymbol{\theta}}), \mathbf{B}_c(\hat{\boldsymbol{\theta}}), \mathbf{E}_c(\hat{\boldsymbol{\theta}}), \mathbf{C}_c(\hat{\boldsymbol{\theta}})\}$ using equations (17) and (18).

Step 4: Evaluate $\mathbf{L}_c(\hat{\boldsymbol{\theta}})$ using equation (23).

Step 5: Estimate the state vector $\hat{\mathbf{X}}_c(\mathbf{t})$ using equation (22).

Step 6: Calculate $\mathbf{K}_c(\hat{\boldsymbol{\theta}})$ using equation (24).

Step 7: Compute $\mathbf{N}(\hat{\boldsymbol{\theta}})$ using equation (25).

Step 8: Apply the control input signal using equation (26).

Step 2 to 8 are repeated for every sampling instant.

Both the modern self-tuning pole-placement, shown in Figure 6, and the classical controllers were programmed as multiple controller algorithms. The design provides a choice of using either classical

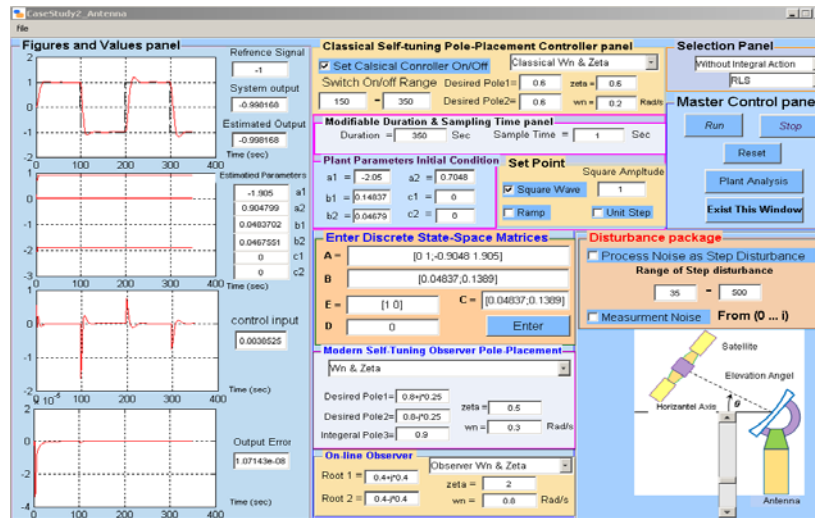


Figure 7: Multiple Controllers GUI

To study the response of the antenna output using multiple controllers, a simulation was carried out using the system described by the discrete state-space equations (8) and (9). The simulation was performed using recursive least squares estimator over 350 samples with a sample time of 1s (approximately 6 minutes) to track a rectangular signal (in dotted black line). The desired set point is a square wave signal that has peak values of 1 and -1 with a duration of 100 samples. The signal and the response using the Modern Self-Tuning Observer Pole-Placement controller is shown in the first 150sample instants in Figure 8-a. The response of the system using the Classical Self-Tuning Pole-Placement controller is used after the 150th sample. The control input for the two cases are shown in Figure 8-b. Figures 8-a shows that these controllers are matched without any transient behaviour during switching mode.

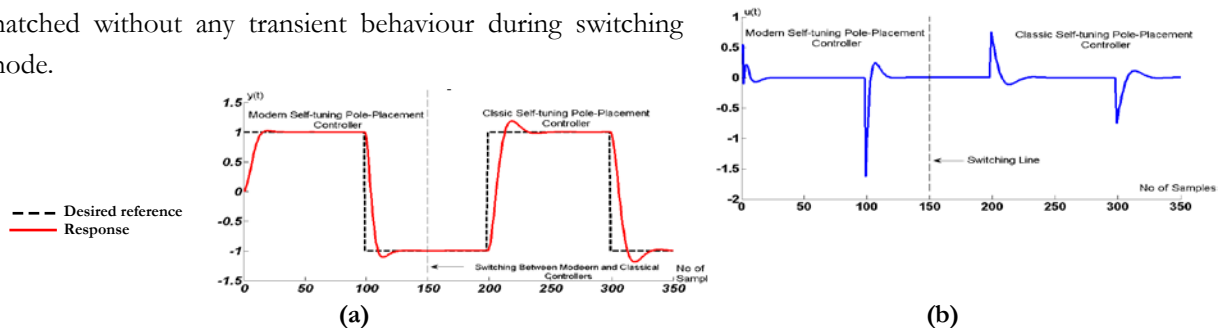


Figure 8: (a) Antenna outputs response for multiple controllers, (b) Multiple control input to the Antenna system
Another simulation was performed over 400 samples (approximately 7 minutes) using recursive least squares (RLS) estimator to track a triangular signal changes from 1 to 0 and from 0 to 1 every 100 samples instants. In this simulation, the classical self-tuning pole placement controller was switched on at 150th sampling instant, whereas the modern STOPPRI controller was used in first part of intervals as shown in Figure 8 and Figure 9.

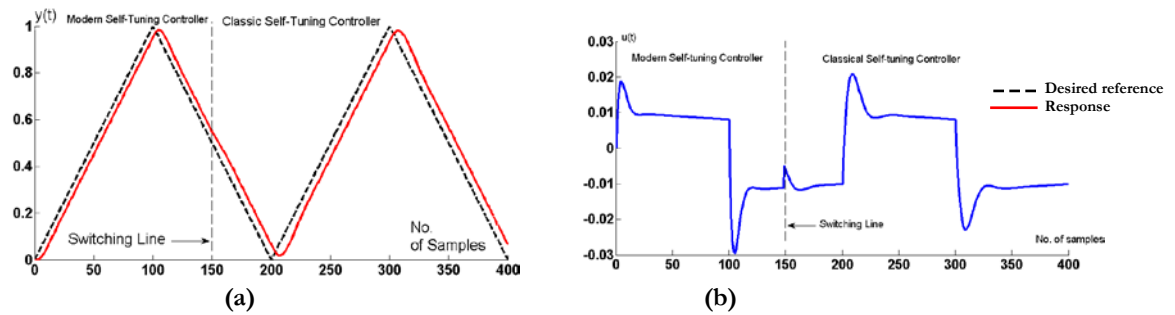


Figure 9: (a) Antenna System Output using modern and classical Controllers (b) Control Input of the Antenna System using classical and modern adaptive Controllers

In Figure 9-b, a small transient behaviour appeared at the 150th sampling instant during switching between modern and classical self-tuning controllers which does not affect the antenna response as shown in Figure 9-a and disappeared at steady-state region.

5. Conclusions

A multiple controller scheme incorporating an adaptive mechanisms using classical transfer function technique and modern discrete state-space technique was designed. The scheme was simulated with the application to antenna model controlling its elevation. This scheme enables the user to effectively switch between the classical and modern controllers. Once the desired controller is selected to be on-line, the other controller remains standby to ensure robust control performance in the presence of controller failure. Simulation testing the proposed method were carried out and shows the performance of the proposed technique.

6. Acknowledgment

The authors would like to thank Ausama Ahmed for his help in writing the manuscript.

References

- [1]. Karl and B. Wittenmark, Adaptive Control, Courier Corporation, 2013.
- [2]. D. W. Clarke, C. Mohtadi and P. S. Tuffs, "Generalized predictive control—Part I. The basic algorithm," *Automatica*, vol. 23, no. 2, pp. 137-148, 1987.
- [3]. Z. Gao, "Scaling and bandwidth-parameterization based controller tuning," in *Proceedings of the American control conference*, 2006.
- [4]. Narendra KS, Cheng Xiang, 2000, 'Adaptive Control of Discrete-time Systems using Multiple Models', *IEEE Transaction on Automatic Control*, 45, 1669-1686.
- [5]. P. N. Paraskevopoulos, 2002, 'Modern control Engineering', CRC Press Taylor & Francis Group.
- [6]. Gene F. Franklin, J. David Powell, Michael L. Workman, 1998, 'Digital Control of Dynamic Systems', 3rd ed., Addison-Wesley.
- [7]. Katsuhiko Ogata, 1992, 'System Dynamics', 2nd ed., Prentice Hall.
- [8]. Norman S. Nise, 2004, 'Control System Engineering', 4th ed., John Wiley & Sons.
- [9]. M. Gopal, 2003, "Digital Control and State Variable Methods", 2nd ed., Prentice Hall.



-
- [10]. Zhongshan Wu, 2001, 'Simulation Study And Instability Of Adaptive Control', MSc., The Department of Electrical and Computer Engineering, Louisiana State University, Louisiana, USA.
- [11]. P. E. Wellstead, M. B. Zarrop, 1991, 'Self-Tuning Systems: Control and Signal Processing', John Wiley & Sons.

Control of a Three-phase Off-Grid Inverter for Photovoltaic Systems Applications

Ali M A Almaktoof¹, Abdulsslam M Ashoor Shaouf², Abdulbaset A Salem Wddan³
1alialmaktoof@gmail.com, 2abedessalam@gmail.com, 3abdalbasitwadan29.3.1994@gmail.com
^{1,2,3}Department of Electrical and Electronic, Faculty of Engineering, Sabratha University, Libya

ABSTRACT

This paper presented a model predictive control (MPC) strategy as used in photovoltaic (PV) systems applications to control a three-phase off-grid inverter. The PV's model was used in this study to investigate the system performance when power is supplied to a resistive-inductive load (RL-load).

The proposed strategy is to handle the output current for the three-phase, off-grid inverter with an RL-load. An assessment is given of the robustness of the control strategy under variable DC voltages, and as required for photovoltaic systems applications, by measuring the Total harmonic distortion (THD) and tracking behaviour of the reference currents; this was done for all DC voltage values. The system is tested as well with different sampling times to check the tracking behavior at designed values. The simulations and result analyses are carried out using MATLAB/Simulink to test the effectiveness and robustness of MPC for three-phase off-grid inverter with resistive-inductive load supplied by a PV system. The simulation results indicated that the proposed control algorithms achieved both high performance and a high degree of robustness in photovoltaic systems applications.

Keyword— Finite State-Model Predictive Control, three-phase off-grid inverter, photovoltaic systems.

1. Introduction

In recent years the use of renewable energy systems has become very important due to environmental concerns and the increased demand for energy [1, 2]. Renewable energy resources like solar energy can be used with maximum efficiency by utilizing appropriate power converters. As the availability of this energy resource is greatly uncertain, the power conversion system must rely on a suitable power converter and controller unit [3, 4]. The urge to increase the energy efficiency of all energy related systems in combination with the need to support emerging technologies like sustainable energy sources, promotes the development of highly efficient, high-power converters. Three-phase off-grid inverters are widely used in industrial applications and renewable energy systems [2, 5].

Model predictive control (MPC) for power converters has been researched since the early 1980s [5]. MPC requires a high number of calculations as compared to classic control methods, but the fast microprocessors available today have made it possible to viably implement predictive control coupled with three-phase inverter with long prediction horizon [7]. Furthermore, MPC for power converters

has distinct advantages when compared to the traditional pulse width modulation (PWM) methods [8].

Since power converters have a finite number of switching states, the MPC optimization problem can be easily formulated, simplified and reduced to the prediction of the system behaviour specifically for those possible switching states. This control method is known as a finite state-model predictive control (FS-MPC) approach. Many studies have been conducted into the successful application of FS-MPC schemes incorporated in three-phase inverters and drive applications [9-12].

The paper starts with an overview of the system description which presented in Section 2. This paper presents one of the simplest predictive control schemes, which is current control for a three-phase inverter. A simple model of the converter and the load are presented in section 3 and 4 respectively. The model predictive control of off-grid inverter is developed in Section 5. Results and discussions are presented next, followed by a conclusion in the last section of the paper.

2. System Description Overview

A three-phase off-grid inverter for the commonly renewable energy source available in Libya(solar energy)subject to model predictive control strategy is shown in Figure 1. Considering that the two switches in each inverter phase operate in a complementary mode in order to avoid short circuiting the DC source, the switching state of the power switches S_x , with $x = 1, \dots, 6$, can be represented by the switching signals S_a , S_b , and S_c defined as follows:

$$S_a = \begin{cases} 1 & \text{if } S_1 \text{ on and } S_4 \text{ off} \\ 0 & \text{if } S_1 \text{ off and } S_4 \text{ on} \end{cases} \quad (1)$$

$$S_b = \begin{cases} 1 & \text{if } S_2 \text{ on and } S_5 \text{ off} \\ 0 & \text{if } S_2 \text{ off and } S_5 \text{ on} \end{cases} \quad (2)$$

$$S_c = \begin{cases} 1 & \text{if } S_3 \text{ on and } S_6 \text{ off} \\ 0 & \text{if } S_3 \text{ off and } S_6 \text{ on} \end{cases} \quad (3)$$

These switching signals define the value of the output voltages

$$V_{aN} = S_a V_{dc} \quad (4)$$

$$V_{bN} = S_b V_{dc} \quad (5)$$

$$V_{cN} = S_c V_{dc} \quad (6)$$

Where V_{dc} is the DC source voltage.

Considering all the possible combinations of the gating signals S_a , S_b , and S_c , eight switching states and consequently eight voltage vectors are obtained (see Figure 2). In Figure 2 note that $V_0 = V_7$, resulting in a finite state of only seven different voltage vectors in the complex plane.

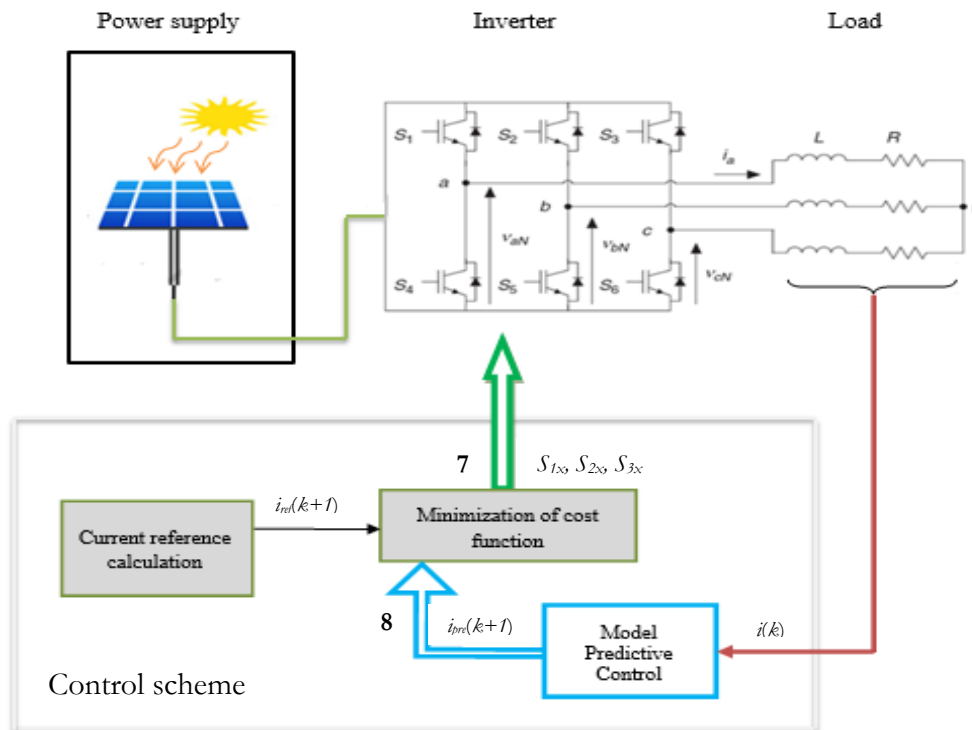


Figure 1: Inverter topology connected to the load and control block diagram

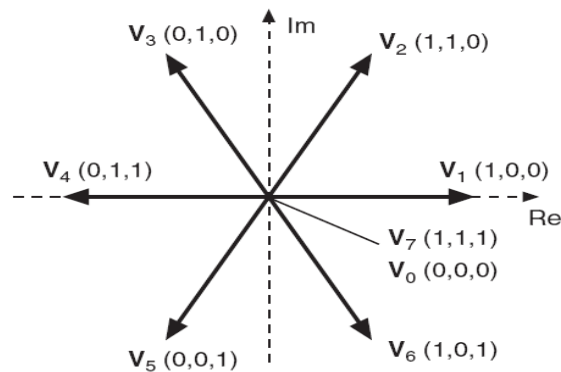


Figure 2: Voltage vectors in the complex plane.

3. Load Model

The differential equation of the load current for the inverter is applied to obtain the continuous-time state space equations of the load for each phase, the load current dynamics can be described by the vector differential equation

$$v_{DC}(t) = R_L \cdot i(t) + L_L \frac{di}{dt} \quad (7)$$

Where v is the voltage vector generated by the inverter, i is the load current vector. The load current derivative $\frac{di}{dt}$ is replaced by a forward Euler approximation[7]. That is, the derivative is approximated as follows:

$$\frac{di}{dt} \approx \frac{i(k+1)-i(k)}{T_s} \quad (8)$$

Which is substituted in (7) to obtain an expression that allows prediction of the future load current at time $k+1$, for each one of the seven values of voltage vector $v(k)$ generated by the inverter. This expression is

$$i^p(k+1) = \left(1 - \frac{RT_s}{L}\right) i(k) + \frac{T_s}{L} v(k) \quad (9)$$

Using the Clarke transformation, Clarke transformation is defined as following,

$$v_\alpha = 2/3 (Va - 0.5 Vb - 0.5 Vc) \quad (10)$$

$$v_\beta = 2/3 (0.5 \sqrt{3} Vb - 0.5 \sqrt{3} Vc) \quad (11)$$

Then, the discrete-time load model can be to:

$$\begin{pmatrix} i_\alpha(k+1) \\ i_\beta(k+1) \end{pmatrix} = \begin{pmatrix} 1 - T_s \frac{R_L}{L_L} & 0 \\ 0 & 1 - T_s \frac{R_L}{L_L} \end{pmatrix} \begin{pmatrix} i_\alpha(k) \\ i_\beta(k) \end{pmatrix} + \begin{pmatrix} \frac{T_s}{L_L} & 0 \\ 0 & \frac{T_s}{L_L} \end{pmatrix} \begin{pmatrix} v_\alpha(k) \\ v_\beta(k) \end{pmatrix} \quad (12)$$

Equation (12) is used to predict the load current for each switching possibility.

4. Cost Function

The objective of the current control scheme is to minimize the error between the measured currents and the reference values. This requirement can be written in the form of a cost function [7,8]. The cost function g is evaluated for each of the seven possible voltage vectors generated by this inverter to calculate the future value of the load current. The voltage vector that minimizes the cost function is selected and applied during the next sampling instant. The cost function is expressed in orthogonal coordinates and measures the error between the references and the predicted currents:

$$g = |i_\alpha^*(k+1) - i_\alpha^p(k+1)| + |i_\beta^*(k+1) - i_\beta^p(k+1)| \quad (13)$$

5. Model Predictive Control of Off-Grid Inverter

As presented early in Figure 1 a three-phase off-grid inverter for a PV system application subject to model predictive control strategy where i_{ref} represents the reference current for the predictive control, $i(k)$ is the measured variable current at time, k , and $i_{pre}(k+1)$ is the predicted current for n allowed switching states at time, $(k+1)$. The errors between the reference and predicted values are obtained to minimize the cost function, and the switching state that minimizes the cost function, is chosen. The switching signals, S , of the chosen state are then applied to the converter. To reduce the computational effort that arises from the switching possibilities (8 different switching possibilities for

one prediction step), the switching state that delivers the best voltage vector among 7 voltage vectors is determined; this was illustrated in Figure 2. The optimal switching state, which is the one that minimizes the simple cost function, is selected and applied at the next sampling instance when the time is $(k+1)$. The block diagram of the different tasks performed by the predictive controller is shown earlier in Figure 1. In general, the control algorithm, can be summarized by the following steps:

- (1) Measure the load currents and DC voltage.
- (2) Initialize the value of the optimum cost function.
- (3) For all permissible switching states, predict the load currents and capacitor voltages for the next sampling instant.
- (4) Evaluate the cost function for each prediction.
- (5) Select the optimal switching state that minimizes the cost function.
- (6) Apply the new switching state.

6. Results and Discussion

The simulations and result analyses are carried out using MATLAB to test the effectiveness and robustness of FS-MPC for a three-phase, two-level off-grid inverter with resistive-inductive load supplied by a photovoltaic system as shown in Figure 1. Table 1 shows the parameters used for the simulation.

Table 1: Parameters used for the co-simulations

Parameter	Value
Load resistance, R	10 Ω
Load inductance, L	35 mH
DC voltage, v_{DC}	300 V
Amplitude of the reference current, i_{ref}	8 A
Sampling time, T _s	100 μ s

The control algorithm was evaluated with regard to two performance indicators: Firstly, the robustness and variability of control strategy under variable input DC voltage is done, and secondly, with different sampling time, the system is investigated.

6.1. Control strategy robustness under variable DC voltages

In this simulation the system is designed at a voltage value is 300V at sampling time $T_s = 75 \mu s$. Figure 3 shows the output current i_α , magnitude value of output current and output voltage v_α by using Fast Fourier Transform (FFT) in MATLAB/SUMLINK.

To demonstrate the stability of the proposed control method under conditions of variable DC voltages; the system has been tested when the DC voltage was changed from 125 to 600 V with $T_s = 75 \mu s$. Figure 4 shows the output currents for different values of DC voltages. It can be observed that the proposed control algorithm has the ability to follow sinusoidal reference currents despite substantially changing the DC voltage from the desired voltage except Figure 4(a). These results of the simulation are in Table 2

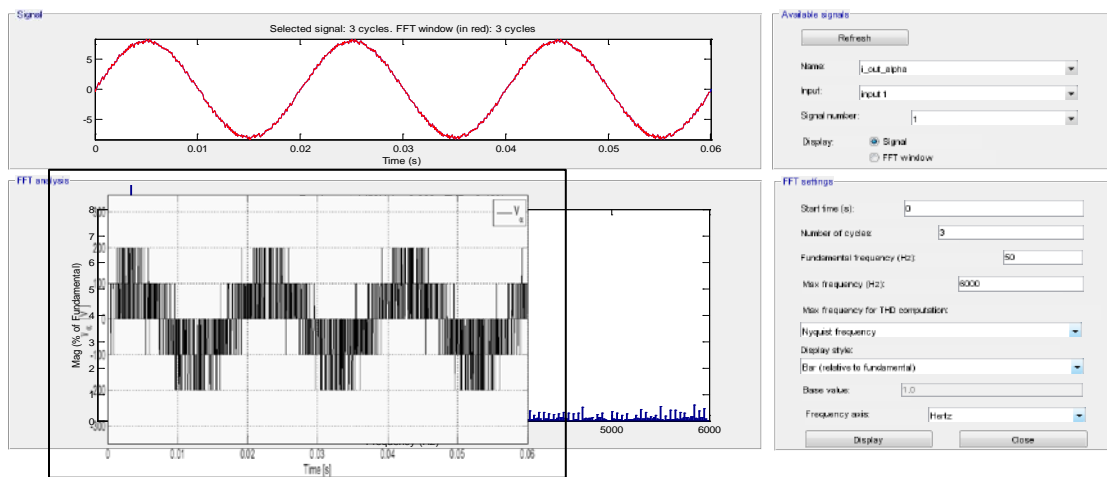


Figure 3: Output current and its magnitude value and output voltage at designed values.

Table 2: THD and output current for variable DC voltages

DC-Link value, [V]	Fund. current at 50 Hz, [A]	THD [%]
125	6.096	7.76
200	8.007	2.33
220	8.015	2.66
240	8.006	2.69
260	7.978	2.95
280	8.000	3.35
320	7.971	3.46
340	8.021	3.85
360	7.981	4.14
380	7.999	4.30
400	7.969	4.66
450	7.945	5.07
500	8.008	5.71

550	7.997	6.41
600	7.961	6.64

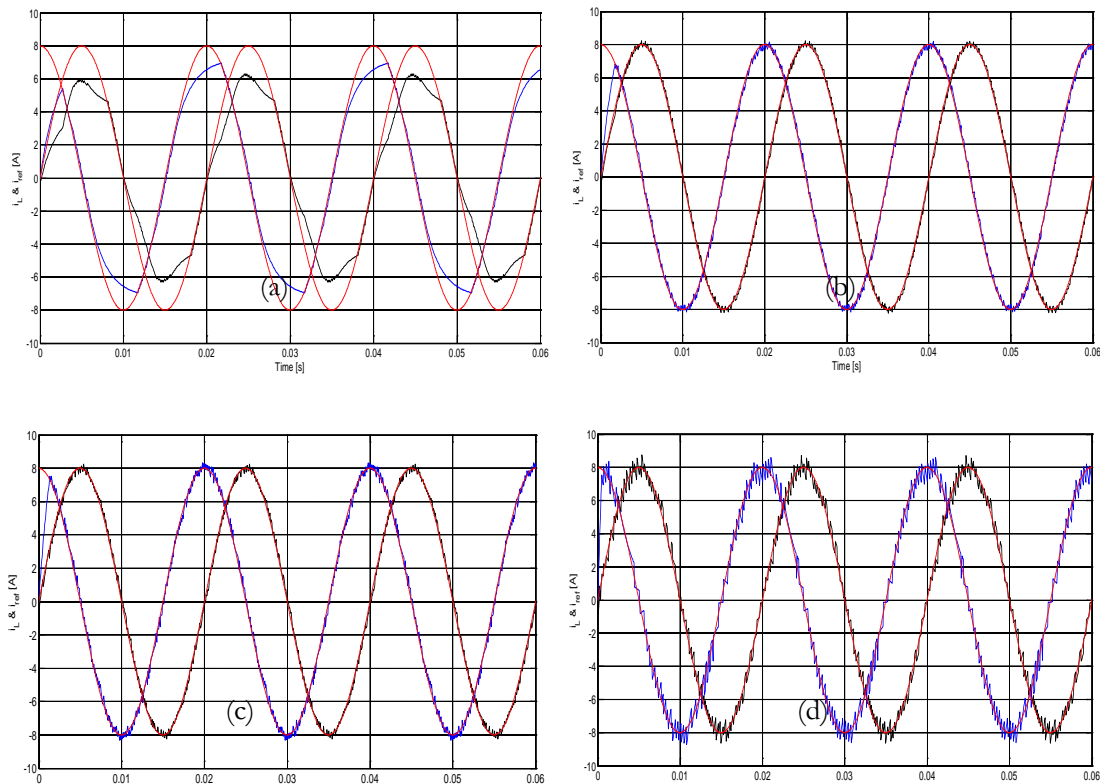


Figure 4: Output currents for different values of DC voltage at $T_s = 75 \mu s$. (a) $V_{DC} = 125V$, (b) $V_{DC} = 200V$, (c) $V_{DC} = 400V$ and (d) $V_{DC} = 600V$.

In Figure 4(a) is shown the output current of the DC voltage when it was set to 125V and the THD was 7.76% and the fundamental current at 50 Hz is 6.096. It is notable that the system was out of control at 125V with high THD and a high amplitude error was produced.

In Figure 4(b) is shown the results of the DC voltage when it was set to 260 V and the THD was 2.95%. Compare these results to those shown in Figure 4(c) when the DC voltage was set to 400 V and the THD 4.66%, as well as those shown in Figures 4(d) when the DC voltage was set to and 600 V and the THD was increased to 6.64%.

It is notable that voltages higher than the designed voltage value of 300 V produced a higher THD, while the amplitude of the output current was kept constant and tracked the reference current with a

small error. On the other hand, for DC voltage values smaller than the designed value, a lower THD with a relatively small amplitude error was produced.

6.2. Control strategy robustness under variable DC voltages

Depending on the complexity of the controlled system, the number of calculations can be significant and will limit the minimum sampling time. In the simplest case, predictive current control, the calculation time is small, but in other schemes such as torque and flux control, the calculation time is the parameter which determines the allowed sampling time.

This simulation demonstrated the effectiveness of the proposed control method under conditions of different sampling times; in particular when the sampling time was changed from 25 to 150 μs at the designed parameters values. Figure 4 shows the output currents for different values of sampling times. It can be observed that the proposed control algorithm has the ability to follow sinusoidal reference currents despite substantially changing the sampling time from the desired sampling time. These results of the simulation are in Table 3.

In Figure 5 is shown, the results of the output current and output voltages, where current and voltage in one phase of the load are shown in Figure 5(a) and Figure 5(b) for sampling time $T_s = 150 \mu\text{s}$ and $100 \mu\text{s}$ respectively. There is no steady state error in the current but there is a noticeable ripple. This ripple is reduced considerably when a smaller sampling time is used, as shown in Figure 5(c) and Figure 5(d) for a sampling time $T_s = 25 \mu\text{s}$ and $50 \mu\text{s}$ respectively. However, by reducing the sampling time, the switching frequency is increased as can be seen by comparing the load voltages in Figure 5.

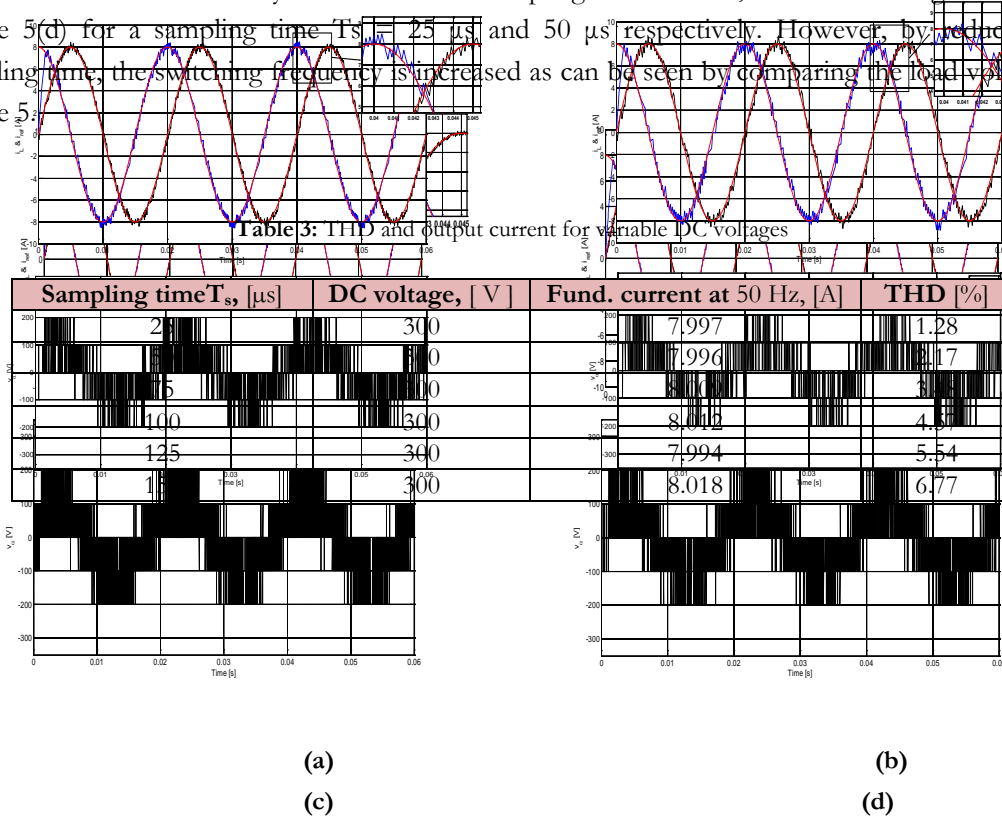


Figure 5: Output currents for different values of sampling time T_s

7. Conclusions

In this paper the MPC strategy for PV system applications has been presented to control the three-phase off-grid inverter. The PV model has been used in this paper to investigate the system performance when power is supplied to RL-load. The proposed control method does not require any kind of linear controller or modulation technique. The FS-MPC algorithm has been evaluated through simulation results. Firstly, the robustness of control strategy under variable DC for three-phase off-grid inverter for PV system application has been done in terms of the THD. Secondly, with different sampling time, the system has been investigated. The simulation results show that the predictive control method has the ability to track sinusoidal reference currents and show excellent tracking behavior with all DC voltage values. Although the theory of MPC was developed in the 1970s, its application in power converters is more recent due to the fast sampling times that are required. The fast microcontrollers available in these days have made it possible to implement the proposed control scheme to three-phase off-grid inverter for PV system application. Sampling time can critically affect the performance of a control system. selecting the best sampling time to execute the entire algorithm is depends on the switching frequency in the load voltages.

References

- [1]. Siemens, 2012. Energy Sector 2012, Erlangen (Germany), www.siemens.com/energy [20May2018].
- [2]. Nami & F. Zare. "Multilevel Converters in Renewable Energy Systems, Renewable Energy," T J Hammons (Ed.), ISBN: 978-953-7619-52-7, 2009. InTech, Available from: <http://www.intechopen.com/books/renewable-energy/multilevel-converters-in-renewable-energy-systems>.
- [3]. E. J.Bueno, S.Cobrecas, F. J. Rodríguez, A. Hernandez, &F. Espinosa, "Design of a back-to-back NPC converter interface for wind turbines with squirrel-cage induction generator," *IEEE Trans. on Energy Conversion*, Vol. 23 No.3, 2008. pp.932–45.
- [4]. L. M.Tolbert &F. Z. Peng, "Multilevel Converters as a Utility Interface for Renewable Energy Systems," *IEEE Power Engineering Society Summer Meeting*, Volume 2, 16–20 2000. pp. 1271-1274. Seattle, Washington.
- [5]. N. Mohan, T. M. Undeland, and W. P. Robbins, "Power Electronics: Converters, Applications and Design," (3rd edition). New York: John Wiley & Sons. 2003.
- [6]. R. Kennel and D. Schroeder, "Predictive control strategy for converters," in *Proc. the third IFAC Symposium*, pp. 415–422, Lausanne, 1983.
- [7]. M. Almaktoof, A. K. Raji and M. T. E. Kahn, "Performance Evaluation and Improvement of an FS-MPC for Two-Level VSI," *The International Conference on Electrical and Electronics Engineering, Clean Energy and Green Computing (EEECEGC 2013)*, United Arab Emirates, pp. 120–126. December 11–13, 2013.
- [8]. J. Rodríguez and C. Cortés, "Predictive control of Power Converters and Electrical Drives," UK: A Johan Wiley & Sons, Ltd., 2012.
- [9]. V. Yaramasu, M.Rivera, B. Wu, & J. Rodríguez, "Model Predictive Current Control of Two-Level Four-Leg Inverters—Part I: Concept, Algorithm, and Simulation Analysis," *IEEE Transactions on Industrial Electronics*, vol. 28 no. 7. July 2013, pp. 3459–3468.



- [10]. H. Abu-Rub, J. Guzinski, Z. Krzeminski, &H. A. Toliyat. "Predictive current control of voltage source inverters," *IEEE Trans. on Ind. Electron*, vol. 51 no. 3, 2004. pp. 585–593.
- [11]. J. Li, F. Zhuo, X. Wang, L. Wang, &S. Ni, "A grid-connected PV system with power quality improvement based on boost + dual-level fourleg inverter," in *Proc. IEEE Int. Power Electron. and Motion Control Conf.*, Wuhan, China, 2009. pp. 436–440.
- [12]. R. Vargas, P. Cortés, U. Ammann, J. Rodríguez, & J. Pontt, "Predictive control of a three-phase neutral-point-clamped inverter," *in IEEE Transactions on Industrial Electronics*, vol. 54, no. 5, Oct. 2007, pp. 2697-2705.

Excimer Laser Processing of IGZO Thin Films for Transparent TFTs

Khairi. M.Abuseabee¹, Khalid.M.Alajel², Salem O. Elhamali³

1kmabusabee@elmergib.edu.ly, 2aalajaly2005@gmail.com, 3s.elhmali@asmarya.edu.ly

¹Electrical and Computer Engineering Department, Faculty of Engineering, Elmergib University, Al-Khums, Libya

²School of Science and Technology, Nottingham Trent University, Clifton Lane, Nottingham NG11 8NS, UK

³Electrical and Computer Engineering Department, Faculty of Engineering, Al-Asmarya Islamic University, Zliten, Libya

ABSTRACT

The effects of post deposition annealing treatments on indium gallium zinc oxide IGZO thin films deposited by radio frequency RF magnetron sputtering at ambient temperature have been studied for application to thin film transistor TFT devices fabrication. Krypton Fluoride KrF ($\lambda=248$ nm) excimer laser annealing ELA and low-temperature thermal annealing (150°C) has been applied to IGZO films of 30nm and 50nm thickness as part of the fabrication process for TFT devices. The effect of annealing pre and post patterning of the IGZO channel layers was investigated. The results indicate that single pulse ultra rapid ELA is a viable technique for processing of the channel layers to provide TFT characteristics equivalent to or even better than that produced by a 150°C annealing for one hour. ELA treatment pre-patterning resulted in TFTs demonstrating a higher ON current and on/off current ratio relative to ELA treatment post-patterning. This could be attributed to surface defects introduced by the photolithographic patterning of the IGZO channel. In comparison, the thermally treated films exhibited better performance with the post-patterning thermal treatment.

Keyword— RF magnetron sputtering, excimer laser annealing, post patterning, pre patterning, thin film transistors, IGZO.

1. Introduction

Transparent amorphous oxide semiconductors TAOS are of a great importance in display technologies and are promising candidate materials for emerging applications in flexible transparent electronics. In particular, amorphous indium gallium zinc oxide based thin film transistors (IGZO TFTs) have attracted considerable attention [1,2], and have been demonstrated as switching devices in active matrix liquid crystal displays AMLCDs, and organic light emitting diode OLEDs based display panels[3, 4].

The first functional IGZO based TFTs reported in 2004 by Nomura et al, were fabricated on flexible substrates via pulsed laser deposition PLD. These devices were investigated as an alternative to amorphous silicon (a-Si) and poly silicon (poly-Si) TFTs, because of the high field effect mobility that was demonstrated in the amorphous state (>10 cm²/Vs) [1]. This mobility is attributed to the heavy metal cations with (n-1) d¹⁰ ns⁰(n \geq 5) electronic configuration leading to a large overlap between adjacent cations orbitals [5]. Since the first reports on IGZO TFT research, there has been an increasing interest in studying the effect of post deposition annealing as a mechanism to improve the

IGZO TFTs performance and stability. It has been reported that conventional post-deposition thermal annealing at ($\sim 400^{\circ}\text{C}$) is an effective method to improve the IGZO TFTs performance [6], and stability [7], and reducing the tail state defects in IGZO film [5]. However, post thermal annealing at temperature higher than the maximum allowable temperature for heat resistance of plastic substrates ($\sim 150^{\circ}\text{C}$) is undesirable when considering low cost and flexible substrate applications. As an alternative to thermal annealing, photonic processing using lamps or laser irradiation is a method of interest for a range of thin films' applications where highly localised annealing and surface modification is imposed [8 – 12]. For example, Nakata et.al reported utilizing excimer laser annealing (ELA) to process 20nm IGZO thin films for inverted-staggered bottom gate IGZO-TFTs deposited by RF magnetron sputtering, using two pulses from anXeCl excimer laser ($\lambda=308\text{nm}$) 25ns. IGZO-TFTs irradiated at laser fluences of $130\text{mJ}/\text{cm}^2$ exhibited ON current more than one order of magnitude higher than that of un-annealed devices [8]. Ahn et.al fabricated bottom gate IGZO-TFT, using a 50nm thick channel layer grown by RF magnetron sputtering at room temperature. The IGZO film was selectively laser annealed via a projection mask using anXeCl ($\lambda=308\text{nm}$) excimer laser in air ambient at ten pulses with a range of laser density from 0 to $250\text{mJ}/\text{cm}^2$. The electrical properties of the devices treated with laser energy density $130\text{mJ}/\text{cm}^2$ exhibited a channel mobility $21.79\text{ cm}^2/\text{Vs}$, on/off ratio of 1.2×10^8 , threshold voltage $\sim -0.15\text{V}$. As the laser fluences increased to $130\text{mJ}/\text{cm}^2$ the resistivity of IGZO film decreased from $10^4\ \Omega\ \text{cm}$ to $3.2 \times 10^{-3}\ \Omega\ \text{cm}$ with carrier concentration $1.3 \times 10^{20}\ \text{cm}^{-3}$, and hall mobility $15\ \text{cm}^2/\text{Vs}$ [11].

It has also been reported by Zan et al [13] that Nd(YAG) laser (266nm) or UV lamp irradiation (172nm) suppressed the instability of IGZO TFTs, and reduced the defects in IGZO film. Lim et.al demonstrated improvement of electrical properties of bottom gate ZnO TFT devices fabricated at low temperature (200°C) [14].

For the investigation presented here, we have undertaken a comparison of low temperature (150°C) thermal processing and the application of KrF photons with single pulse irradiation to study the effects on IGZO TFTs characteristics for devices utilising low temperature deposited IGZO thin films as the TFTs active layer. We are particularly interested in when the annealing treatment is applied in the fabrication process, pre or post IGZO channel patterning, and the effect this has on the resultant characteristics.

2. Experimental procedure

2.1. Film deposition

IGZO thin films of 30nm and 50nm thickness were deposited by RF magnetron sputtering from a ceramic target of $\text{In}_2\text{O}_3:\text{Ga}_2\text{O}_3:\text{ZnO}$ molar ratio (1:1:1) and (purity 99.99%) onto silicon dioxide coated silicon substrates. Deposition was performed at ambient temperature (with no intentional substrate heating) across a range of sputtering conditions by varying oxygen concentrations ($2\%\text{O}_2/\text{Ar}$, $5\%\text{O}_2/\text{Ar}$), and RF power (50W, 100W) with deposition pressure 1.33 Pa to optimise the IGZO films for use in TFT device fabrication.

2.2. Post- deposition annealing of IGZO thin films

Annealing by thermal treatment at 150°C for one hour on a hotplate was compared with excimer laser processing undertaken at ambient temperature in air using a Lambda Physik 305i 248nm, 20ns pulse KrF excimer laser, with a beam delivery system providing a homogenised 14mm x 14mm uniform irradiation at the sample plane. Processing was undertaken at fluences in the range of 0mJ/cm² to 175mJ/cm² (\pm 6mJ/cm²) using single pulse irradiation. The resultant IGZO thin films are characterised by four point probe (4PP) measurements, Hall Effect, and used in TFT test devices fabrication.

2.3. IGZO-TFT fabrication

Figure.1 shows the cross section of top gate bottom contacts IGZO-TFT device fabricated on SiO₂/Si substrates as per the following process: (i) chromium (Cr) and gold (Au) deposited by evaporation for source and drain electrode contacts with thicknesses of 5nm and 75nm respectively and patterned by photolithography and lift off techniques; (ii) IGZO active layer deposited by RF magnetron sputtering with no intentional heating of the substrate, from an IGZO ceramic source target with In₂O₃:Ga₂O₃:ZnO molar ratio of (1:1:1) 99.9% purity at RF power of 50W, oxygen concentration 2%O₂ /Ar , at 1.33 Pa working pressure. The devices were divided into two sets. One was laser annealed before IGZO patterning, while the second set was laser annealed after IGZO patterning (in both cases, the samples were laser annealed as described in section 2.2. prior to the gate dielectric deposition). The IGZO layer was patterned via photolithography and wet etching producing IGZO channels with width (W) and length (L) of 1000 μ m and 5 μ m respectively. Alumina (Al₂O₃) was deposited as the gate dielectric by atomic layer deposition ALD at 120°C, and pattern by photolithography and lift off. Finally, a bilayer gate electrode of (Cr/Au, 5/75nm) was deposited by evaporation.

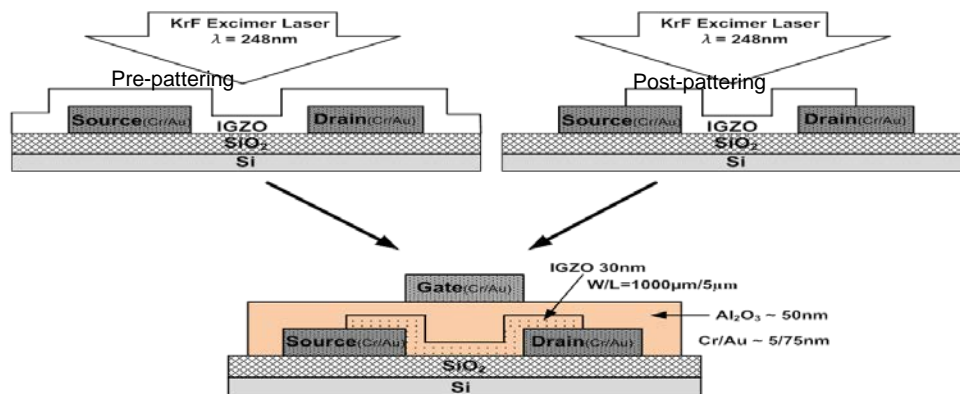


Figure 1: Schematic cross section of IGZO-TFT devices showing the concept of pre and post patterning laser anneal processing

3. Results

3.1. Electrical properties of IGZO thin films

Figure.2 illustrates the sheet resistance of IGZO films deposited at an applied RF power of 50W and various oxygen concentrations following laser annealing at various fluences using single pulse

irradiation. The as-deposited IGZO films were highly resistive and not measurable using the four point probe system (i.e. they have sheet resistances $> 5\text{M}\Omega/\text{sq}$) for all deposition conditions examined. A measurable sheet resistance was achieved at fluences of $\geq 75\text{mJ}/\text{cm}^2$, with the lowest sheet resistance of $1\text{k}\Omega/\text{sq}$ observed at a laser fluence of $100\text{mJ}/\text{cm}^2$ for all IGZO films studied. Processing at higher fluences led to an increase in sheet resistance coincident with visible damage of the film surface at these higher fluences. Similar trends were observed with films grown at RF power 100W .

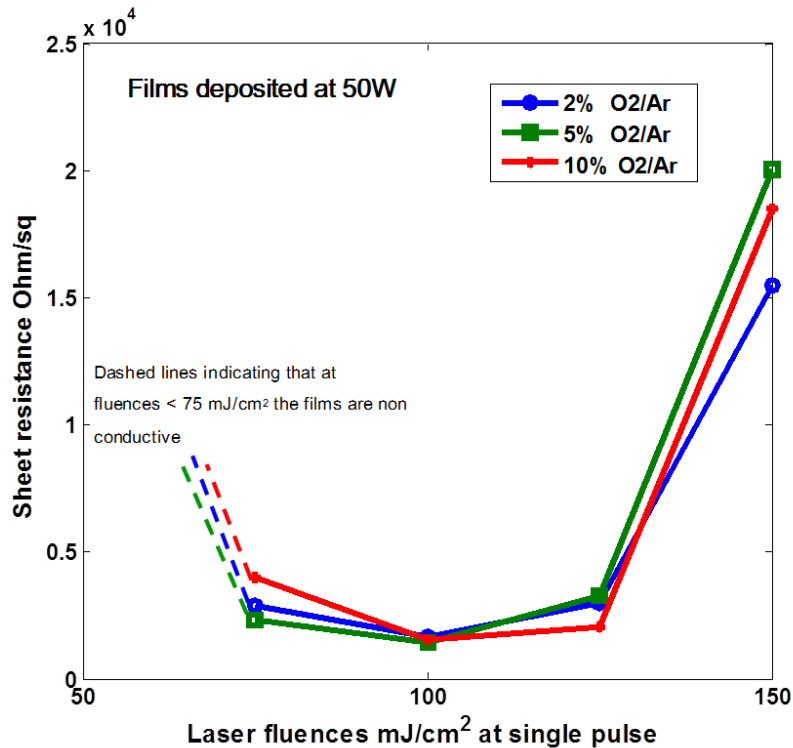


Figure 2: Sheet resistance of 30nm thick IGZO films deposited at 50W following laser processing irradiated at various fluences.

3.2. Hall Effect Characterisation

Figure.3 shows the electrical characteristics as determined via room temperature Hall Effect measurement of the laser processed IGZO thin films, deposited at 50W RF power, 2%O₂/Ar, 50nm, as a function of laser fluence. The as-deposited and samples irradiated at laser fluences of 25mJ/cm², and 50mJ/cm² were too resistive to be measured, consistent with the four point probe measurements. At the higher fluences investigated, of 75mJ/cm² and 100mJ/cm², results were obtained indicating an increase in Hall mobility at higher fluences from 11.1 cm²/Vs to 13.9 cm²/Vs. At 175mJ/cm², however, the mobility dropped to 1.67cm²/Vs, which again coincides with visible surface damage to the films. The drop in carriers mobility at higher fluences could be attributed to the onset of IGZO films crystallisation. The corresponding values of resistivity determined via Hall Effect measurement decreased from 5.92x10⁻² to 9.7x10⁻³ Ω.cm with fluence increasing from 75 to 125mJ/cm² due to a steady increase in carrier concentration that is reduced at higher fluences because

of samples damage. Regarding the thermally annealed samples, they were not measurable due to their high resistance to make contacts with the Hall effect equipment. However, the thermally annealed samples were suitable as the semiconducting channel layer in TFT fabrication, the results of which are described in section 3.3. Similarly, for TFT channel layer fabrication, the laser annealing fluences that produced functional TFT test devices were the lower fluence/higher resistance films processed at $\leq 75 \text{ mJ/cm}^2$.

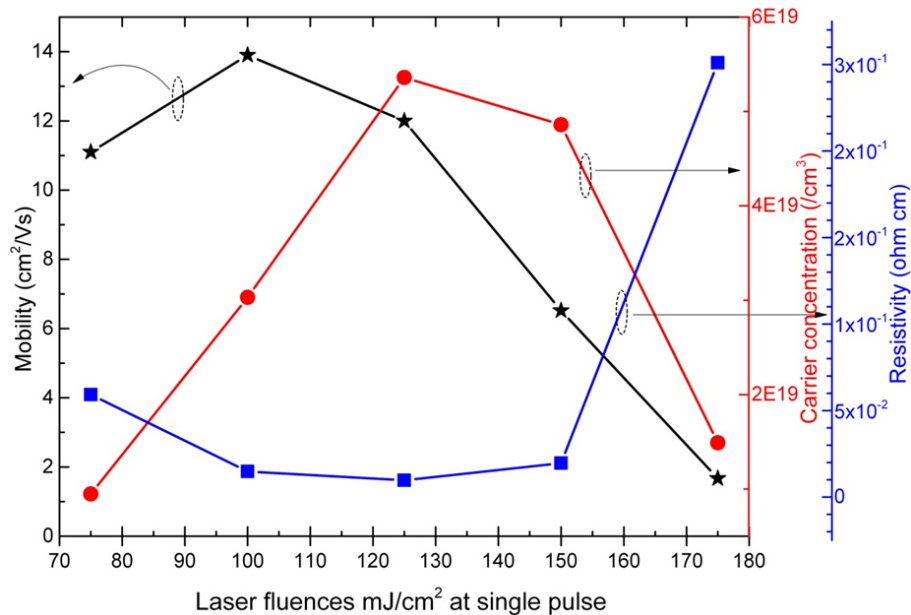


Figure3: Hall Effect characteristics, showing Hall mobility, carrier concentration, and resistivity of 50nm thick IGZO thin films as a function of applied laser fluence.

For IGZO films with thickness of 30 nm, no Hall mobility or conductivity could be detected for as-deposited films and laser irradiated films at various fluences. The high resistivity of laser annealed 30 nm film could be linked to the surface of the film being affected by atmospheric oxygen and changing the film properties and difficulties of achieving contacts with the Hall effect system. This is still a matter for investigation. However, it was reported by Nakata et.al in a comparison study, that the dependance of Hall mobility measurements and carrier density on laser fluence of laser annealed IGZO film by XeCl excimer laser ($\lambda=308 \text{ nm}$) deposited at 20 nm where the highest Hall mobility achieved was $\sim 17 \text{ cm}^2/\text{Vs}$ at laser energy density of about 180 mJ/cm^2 [16].

3.3. Thermal annealed IGZO – TFTs result

Figure 4 shows the transfer characteristics of IGZO-TFTs with the active channel is being IGZO films of 30 nm thick. The TFTs were thermally annealed at $150 \text{ }^\circ\text{C}$ in an air environment for 1 hour, before and after the channel layer patterning. The results are summarised in Table 1 as compared to the non-annealed device. There was a slight improvement in electrical performance of the thermally annealed IGZO TFTs pre IGZO patterning but with an increased OFF current. Whereas, thermally

annealed IGZO TFTs post IGZO patterning show significant improvement of transfer characteristics. In both cases there is a negative shift in the threshold voltage, an improvement in the ON current, and a significant improvement in the On/Off current ratio for the post pattern annealed sample. In general, for the thermally annealed devices, the improvement in performance was better when annealed post IGZO patterning. Similar result trends were observed upon repetition of this exercise.

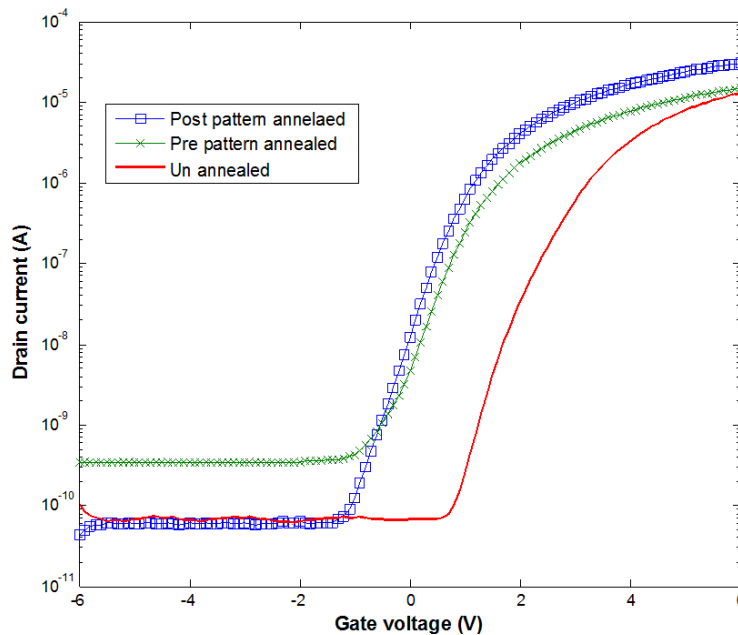


Figure 4: Transfer characteristics of IGZO-TFTs ($W/L = 1000\mu\text{m}/5\mu\text{m}$), $V_{DS} = 1\text{V}$ for samples that had been unannealed compared to samples thermal annealed at 150°C in air for 1 hour pre and post IGZO patterning.

Table 1: The effects of thermal annealing, at 150°C in air for 1 hour pre and post IGZO patterning, on IGZO –TFTs electrical properties.

Sample	V_{th} (V)	μ_{FE} (cm^2/Vs)	S (V/dec)	I_D Max (A)	I_{ON}/I_{OFF} ratio
Un-analed	3.52 ± 0.14	0.14 ± 0.04	0.41 ± 0.14	1.36×10^{-5}	1.48×10^5
150°C pre patterning	1.65 ± 0.28	0.10 ± 0.03	0.64 ± 0.11	1.54×10^{-5}	7.46×10^4
150°C post patterning	1.60 ± 0.23	0.16 ± 0.09	0.52 ± 0.08	2.75×10^{-5}	0.78×10^6

Results indicated that thermal annealing at low temperature after IGZO channel layer patterning is more effective than before, which could be attributed to the effect on the interface between the IGZO layer and the dielectric layer by the photoresist heat treatment at 100°C for 1 min and 20 s, since this would be a different effect when the photoresist is heated pre and post thermal anneal.

3.4. Excimer laser annealed IGZO – TFTs result

The TFT results for the laser processed samples are shown in Figure 5 which represents the characteristics from devices fabricated on the same substrate.

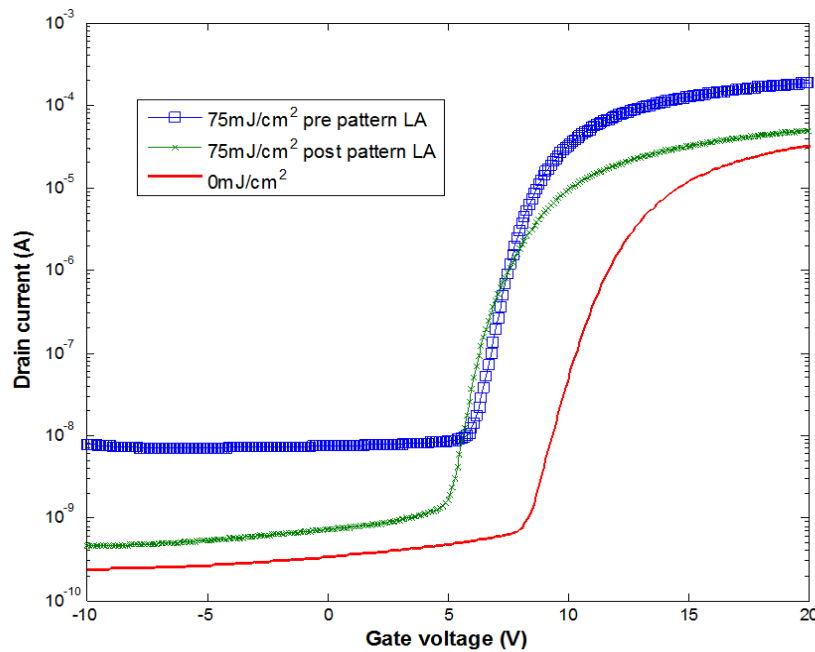


Figure 5: Transfer characteristics of IGZO-TFTs ($W/L = 1000\mu\text{m}/5\mu\text{m}$), $V_{DS} = 1\text{V}$, for samples un-annealed and laser annealed at a fluence of $75\text{mJ}/\text{cm}^2$ in air.

As with the thermally annealed samples, the laser treated TFTs at laser energy density of $75\text{ mJ}/\text{cm}^2$ with single pulse show a negative shift in threshold voltage and an increase of ON current. However, devices laser annealed pre IGZO pattern demonstrate higher ON and OFF current than the devices that were laser processed post to IGZO pattern. This could be assigned to surface defects introduced during photolithographic patterning deteriorating the performance of the laser annealed TFTs. The electrical properties of these devices are summarized in Table 2.

Table 2: Properties of IGZO -TFTs laser annealed pre and post patterning of the active layer 30 nm thick.

Sample	V_{th} (V)	$\mu_{FE}(\text{cm}^2/\text{Vs})$	S (V/dec)	I_D Max (A)	I_{ON}/I_{OFF} ratio
Un- annealed	12.1 ± 0.7	0.003 ± 0.005	0.70 ± 0.04	3.25×10^{-5}	1.58×10^5
$75\text{mJ}/\text{cm}^2$ pre pattern	8.15 ± 0.5	0.64 ± 0.69	0.71 ± 0.07	2.00×10^{-4}	8.47×10^7
$75\text{mJ}/\text{cm}^2$ post pattern	7.93 ± 0.5	0.25 ± 0.21	0.61 ± 0.17	5.01×10^{-5}	3.38×10^6

Laser annealed IGZO-TFT devices with a channel layer 30 nm thick demonstrating very low field effect mobility. This is consistent with the observation that no Hall Effect measurements could be performed on 30 nm thick IGZO films at different laser energy densities, while laser processed 50 nm thick IGZO film exhibited Hall mobility as high as $13.9\text{ cm}^2/\text{Vs}$.

4. Discussion

A significant drop in sheet resistance of IGZO thin films deposited without intentional substrate heating as a function of laser energy density for a single pulse is observed with a strong dependence

on deposition parameters. Post deposition annealing of IGZO films leads to removal of weakly bonded oxygen atoms or oxygen combination contributing to a new equilibrium changing the electrical properties of IGZO films [13, 15]. The lowest sheet resistance post laser processing was observed at deposition conditions of low deposition pressure, low oxygen concentration, and high RF power. This can be attributed to the sputtered atoms' kinetic energy and thus their surface mobility on the substrate is being controlled with the deposition parameters. Hence, the resulting film prosperities are dependent on the films deposition parameters [2, 5]. Upon ELA, the resistivity of IGZO films was considerably reduced and the free electron density as well as the Hall Effect mobility were effectively enhanced as a function of laser fluence. These observations could be attributed to local atomic rearrangement, the amorphous structure randomness relaxation, and trap states density reduction. The local atomic rearrangement and structure relaxation caused by ELA heating, provided that no crystallisation occurs, would enhance the overlap among ns orbitals of the contained metals leading to better carrier mobility [2, 11, 12]. The highest observed Hall effect mobility in this work was $13.9 \text{ cm}^2/\text{Vs}$ obtained by ELA with single pulse at $100 \text{ mJ}/\text{cm}^2$, which is very promising to apply laser treated IGZO to IGZO TFTs.

For IGZO-TFT devices, thermal and laser annealing IGZO channel layer patterns result enhanced electrical performance of IGZO TFTs. This is originated from induced changes in IGZO layers upon annealing including reduction of scattering or trapping defects density on the bulk IGZO or at its interface, enhanced atomic bonding, and amorphous structure relaxation leading to enhanced electrical prosperities of IGZO [2, 11, 12]. laser irradiation is also expected to reduce the contact resistance between the IGZO channel layer and the source/drain electrodes due to reduction of IGZO channels resistivity and increasing the carrier concentration upon ELA. This would move the Fermi level in IGZO to higher positions towards the conduction band i.e. decreasing IGZO work function leading to better electrical contact between IGZO layer and S/D electrodes and thus better IGZO TFTs performance [5, 11]. However, both annealing techniques resulted in negative shift in threshold voltage which could be attributed to the high defects density in the subgap density of states (DOS) pins the Fermi level, so no mobile carries. In addition, TFTs devices demonstrate high values of sub-threshold swing S which is related to trap density in the subgap. High sub-threshold swing S result in poor electrical properties such as, low speed and higher power consumption. Therefore, further investigations are needed to optimise the ELA application to IGZO TFTs fabrication using wide range of annealing parameters.

5. Conclusions

For the results presented here, the room temperature Hall Effect mobility of IGZO (50 nm thick) was effectively enhanced as the laser fluence was increased from $75 \text{ mJ}/\text{cm}^2$ to $100 \text{ mJ}/\text{cm}^2$ (single pulse) reaching values of $11.1 \text{ cm}^2/\text{Vs}$ and $13.9 \text{ cm}^2/\text{Vs}$ respectively.

Laser annealing of IGZO-TFT pre IGZO channel patterns result in relatively higher ON current than post pattern while thermally annealing post IGZO pattern demonstrate higher ON current. Hence, these results demonstrate that laser annealing is a powerful technique to modify the electrical properties of IGZO films grown at room temperature for TFTs applications.

Acknowledgment

We would like to acknowledge the UK Technology Strategy Board for support for this work as part of the SKTP project.

References

- [1]. W. S. Author, K. Nomura, H. Ohta, A. Takagi, T. Kamiya, M. Hirano and H. Hosono, "Room-temperature fabrication of transparent flexible thin-film transistors using amorphous oxide semiconductors," *Nature*, vol. 432, pp. 488-492, 2004.
- [2]. H. Yabuta, M. Sano, K. Abe, T. Aiba, T. Den, H. Kumomi, K. Nomura, T. Kamiya and H. Hosono, "High-mobility thin-film transistor with amorphous InGaZnO channel fabricated by room temperature RF-magnetron sputtering," *Appl. Phys. Lett.*, vol. 89, pp. 112123, 2006.
- [3]. J. Y. Kwon, K. S. Son, J. S. Jung, T. S. Kim, M. K. Ryu, K. B. Park, B. W. Yoo, J. W. Kim, Y. G. Lee and K. C. Park, "Bottom-gate gallium indium zinc oxide thin-film transistor array for high-resolution AMOLED display," *Electron Device Letters, IEEE*, vol. 29, pp. 1309-1311, 2008.
- [4]. C. J. Kim, D. Kang, I. Song, J. C. Park, H. Lim, S. Kim, E. Lee, R. Chung, J. C. Lee and Y. Park, "Highly stable Ga₂O₃-In₂O₃-ZnO TFT for active-matrix organic light-emitting diode display application," in *Electron Devices Meeting, 2006. IEDM'06. International, 2006*, pp. 1-4.
- [5]. H. Hosono, K. Nomura, Y. Ogo, T. Uruga and T. Kamiya, "Factors controlling electron transport properties in transparent amorphous oxide semiconductors," *J. Non Cryst. Solids*, vol. 354, pp. 2796-2800, 5/1, 2008.
- [6]. K. Nomura, T. Kamiya, H. Ohta, M. Hirano, H. Hosono, "Defect passivation and homogenization of amorphous oxide thin-film transistor by wet O₂ annealing," *Appl. Phys. Lett.* 93 (2008) 192107.
- [7]. K. Nomura, T. Kamiya, Y. Kikuchi, M. Hirano, H. Hosono, "Comprehensive studies on the stabilities of a-In-Ga-Zn-O based thin film transistor by constant current stress," *Thin Solid Films*, 518 (2010) 3012.
- [8]. M. Nakata, K. Takechi, K. Azuma, E. Tokumitsu, H. Yamaguchi and S. Kaneko, "Improvement of InGaZnO₄ thin film transistors characteristics utilizing excimer laser annealing," *Applied Physics Express*, vol. 2, pp. 1102, 2009.
- [9]. N. Mitsuru, T. Kazushige, Y. Shinya, T. Eisuke, Y. Hirotaka and K. Setsuo, "Effects of Excimer Laser Annealing on InGaZnO₄ Thin-Film Transistors Having Different Active-Layer Thicknesses Compared with Those on Polycrystalline Silicon," *Jpn J Appl Phys.* 48 (2009) 115505.
- [10]. Y. Yang, S. S. Yang and K. Chou, "Characteristic Enhancement of Solution-Processed In-Ga-Zn Oxide Thin-Film Transistors by Laser Annealing," *Electron Device Letters, IEEE*, vol. 31, pp. 969-971, 2010.
- [11]. B. Du Ahn, W. H. Jeong, H. S. Shin, D. L. Kim, H. J. Kim, J. K. Jeong, S. H. Choi and M. K. Han, "Effect of excimer laser annealing on the performance of amorphous indium gallium zinc oxide thin-film transistors," *Electrochemical and Solid-State Letters*, vol. 12, pp. H430-H432, 2009
- [12]. C. Tsakonas, V. Kuznetsov, W. Cranton, N. Kalfagiannis, K. Abusabee, D. Koutsogeorgis, N. Abeywickrama and P. Edwards "Low temperature sputter-deposited ZnO films with enhanced Hall mobility using excimer laser post-processing," *J. Phys. D: Appl. Phys.* vol.50, pp. 485306 (15). 2017
- [13]. H. W. Zan, W. T. Chen, C. W. Chou, C. C. Tsai, C. N. Huang and H. W. Hsueh, "Low temperature annealing with solid-state laser or UV lamp irradiation on amorphous IGZO thin-film transistors," *Electrochemical and Solid-State Letters*, vol. 13, pp. H144-H146, 2010.



- [14]. S. Lim, J. M. Kim, D. Kim, C. Lee, J. S. Park and H. Kim, "The Effects of UV Exposure on Plasma-Enhanced Atomic Layer Deposition ZnO Thin Film Transistor," *Electrochemical and Solid-State Letters*, vol. 13, pp. H151-H154, 2010.
- [15]. Suresh, P. Gollakota, P. Wellenius, A. Dhawan and J. F. Muth, "Transparent, high mobility InGaZnO thin films deposited by PLD," *Thin Solid Films*, vol. 516, pp. 1326-1329, 2008
- [16]. M. Nakata, K. Takechi, S. Yamaguchi, E. Tokumitsu, H. Yamaguchi and S. Kaneko, "Effects of excimer laser annealing on InGaZnO₄ thin-film transistors having different active-layer thicknesses compared with those on polycrystalline silicon," *Jpn J Appl Phys*, vol. 48, pp. 115505-115505-6, 2009.

Loss of Load Expectation of Alkhoms Generating Units

Mohamed Altaher Ben Mouhsen¹, Ali A. Tamtum²

1md.mohsen.ly@gmail.com, 2aamtatum@yahoo.com

^{1,2}Department of Electrical and Computer Engineering, Elmergib University, Libya

ABSTRACT

Alkhoms generating power station is one of the largest stations in the Libyan generation system. It consists of eight units represent approximately 18% of the Libyan generation capacity. Hence, it is chosen to perform the reliability study presented in this paper. Generation system reliability is an important aspect in the planning for the future system capacity expansion since it provides a measurement to make sure that the total generation system capacity is sufficient to provide adequate electricity when needed. There are two approaches used for generating units reliability, deterministic and probabilistic approaches. The probabilistic approach branches into Monte Carlo simulation and analytical methods which include loss of load expectation (LOLE). The LOLE is the most widely used index in generation adequacy evaluation; it indicates the expected time for which the available generation will not be sufficient to meet the demand. In this paper, a reliability study is performed on Alkhoms generating units. Forced outage rates (FOR) is calculated, annual load data is analyzed, annual load duration curve is constructed and convolved with the generation model, and the (LOLE) is evaluated. The effect of load growth and FOR variation are also considered. A computer program is written in MATLAB as a tool for this purpose and used to construct the annual load duration curve and capacity outage probability table (COPT). The importance of this study comes from the fact that the system consists from non-identical units since the eight units has a different FOR which complicate the evaluation; as well as the fact that the binomial distribution cannot be applied directly while most published studies simplify the evaluation by grouping up identical units

Keyword— Reliability study; loss of load expectation (LOLE); Forced outage rates (FOR); Load duration curve.

1. Introduction

The fundamental aim of any power utility is to satisfy the system load and energy requirement of its customers at the lowest operating cost with an acceptable level of continuity and quality of electricity supply. In Libya, the General Electric Company of Libya (GECOL) is the power utility responsible for generation, transmission and distribution of the electric power for the whole country. The total installed capacity of the generating units was 6200MW in 2008 which is not sufficient to meet the present peak load.

Alkhoms generating station is one of the biggest stations in the Libyan generation system, it consists of eight generating units with total generating capacity of 1080 MW which represents about 18% of the Libyan gross capacity. Moreover, its data is available at the station office. Hence, it was chosen to perform this study.

Many papers throughout the world related to LOLE has been published, such as [1], in which the impact of aging characteristics of components on the calculation of reliability indices such as LOLE was described. In [2] the LOLE was evaluated for a proposed test system of six generating units is used, some units has identical FOR and identical capacities with 64 states of available capacity. In [3] a

method for generation reliability assessment using intelligent systems was proposed. The effect of varying the load and failure rates on reliability indices was analysed in [4] . The relationship between LOLE and reserve margin was discussed in [5] where the peak load variation curve (DPLVC) with 365 point is used instead of load duration curve for a modified Peninsular Malaysia system consisting of 22 generating units and the LOLE was evaluated in days/year.

In [6], LOLE has been discussed for Alkhoms gas and steam units as two individual subsystems each of them consists of four identical units with 16 states of available capacity.

The object of this paper is to develop techniques to evaluate LOLE for Alkhoms generating system consisting of eight units having different capacities and different FOR with 256 states of available capacities and using a generation model based on a wide range of actual history including 2015 and 2016.

2. Generation System Reliability.

Generally; reliability can be defined as the probability of device (or system) performing its purpose adequately for the period of time intended under the operating conditions[7]. Reliability evaluation of a complete power system including generation, transmission, station and distribution facilities is an important in overall power system planning and operation[8]. Due to the enormity of the problem, reliability analysis of each level is performed independently.

Generation system reliability is concerned only to the generating units reliability, assuming that other levels are 100% reliable. The first techniques of generation system reliability were all deterministic. The most common deterministic approaches are the reserve margin and the largest set in the system[9]. Probabilistic methods can provide more meaningful information to be used in the sign and resources in planning and allocation. There are two main approaches for probabilistic evaluation of power system reliability; analytical methods and Monte Carlo simulation. Analytical techniques represent the system by mathematical methods and use direct analytical solutions to evaluate a priori reliability indices from the model, it includes loss of load expectation (LOLE), loss of energy expectation (LOEE) and frequency and duration method. Monte Carlo simulation estimates the actual random behaviour of the system[10].

The basic approach for the generating system adequacy consists of three parts as shown in Figure 1.

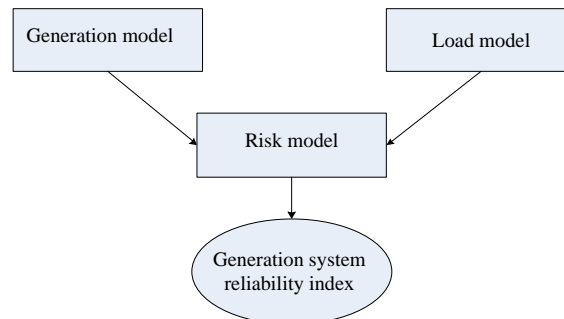


Figure 1: Generating system adequacy

The generation model and the load model are convolved to give the risk model which represent the risk of generation capacity less than load. The adequacy evaluation of the generation system consists of three steps :

create a general capacity model based on the operating characteristics of the generating units .

build an appropriate load model .

combine the generation capacity model with the load model to obtain the risk model.

2.1. Generation Model (State Space Representation)

For simplicity, with no derated states considered, generating unit can be reside only in up or down (repair) state as shown in Figure 2.

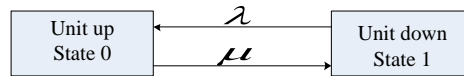


Figure 2: State space diagram of a generating unit

Where: λ is the expected failure rate.

μ is the expected repair rate.

m is the mean time to failure.

r is the mean time to repair.

T is the cycle time = $m + r$

The term unavailability (forced outage rate) can be defined as the probability of finding the unit on forced outage at a certain time in future.

$$Unavailability = U = FOR = \frac{\Sigma(down\ time)}{\Sigma(down\ time) + \Sigma(rep\ time)}$$

(1)

$$U = \frac{\lambda}{\lambda + \mu} = \frac{r}{r + m}$$

(2)

The total number of available (or unavailable) capacity states of an n units system is 2^n

2.2. Capacity Outage Probability Table (COPT)

In the analytical method, generation model is based on capacity outage probability table which lists system capacity states in increasing order of capacity outage, together with the probability of occurrence of each of these states [11].

If all units have identical capacity and FOR then the COPT can be constructed directly using binomial distribution in the following form:

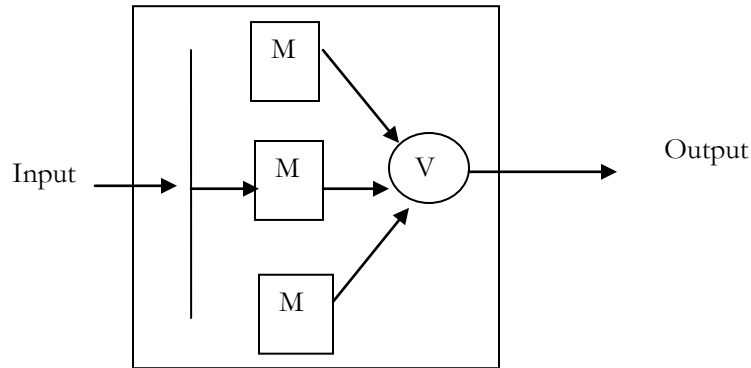
$$(p + q)^n$$

(3)

Where: p is the availability.

q is the unavailability.

n is the number of units.



If all units haven't identical capacity but have identical FOR, binomial distribution cannot be applied directly but we should classify units in groups of tables according to their capacities and FOR and combine identical units using binomial distribution; then combine together one at a time that groups of tables. If the units have different FOR, then the expression of equation (3) becomes as follow:

$$(p_1 + q_1)(p_2 + q_2) \dots \dots \dots (p_n + q_n) \quad (4)$$

2.3. Load Model

The load model used in an analytical approach is usually either the daily peak load variation curve (DPLVC) or the load duration curve (LDC). The DPLVC includes only the peak load of each day for the period being considered, whereas the LDC includes the hourly variation of the load in this period [8]. Figure 3 shows a typical LDC.

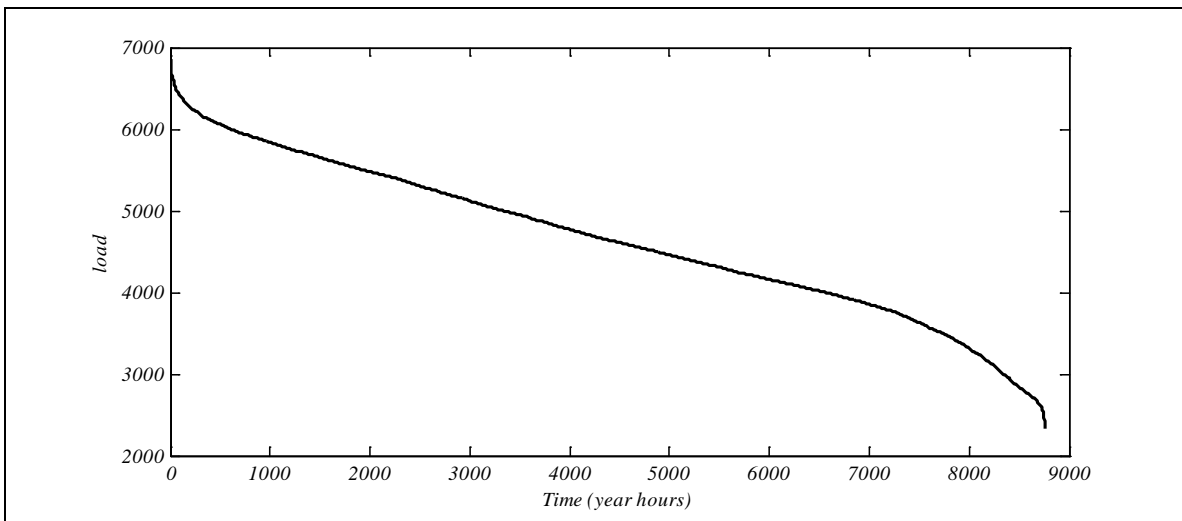


Figure 3: A typical load duration curve

3. Loss Of Load Expectation (LOLE)

The term ' capacity outage ' indicates a loss of generation which may or may not result in a loss of load. This condition depends up on the generating capacity reserve margin and the system load level . A loss of load will occur only when the capability of the generating capacity remaining in service is

exceeded by the system load level [11]. The LOLE indicates the expected time for which the available generation will not be sufficient to meet the demand [12].

After combining the generation capacity model with the load model, then the loss of load expectation can be evaluated from the following formula :

$$LOLE = \sum P_k(Q_k) \cdot t_k \quad (5)$$

Where: P_k is the individual probability of capacity outage of Q_k .

Q_k is the magnitude of the outage in the system capacity outage probability table.

t_k is the number of time units in the study interval than an outage magnitude of Q_k would result in loss of load.

n is the number of states of the capacity outage probability table.

4. Numerical Results

1. Case study

Alkhoms generation station consisting of eight units of a total generating capacity of 1080 MW, the FOR is based on two years' operating cycle data. Table (1) illustrates the generation system data [13].

Table 1: generating system data

Unit number	Capacity (MW)	FOR
1	150	0.012
2	150	0.023
3	150	0.149
4	150	0.029
5	120	0.046
6	120	0.083
7	120	0.024
8	120	0.085

2. Simulation Results

Simulation is carried out using M-File/Matlab software to construct the capacity outage probability table (COPT) of 256 states of available (or unavailable) capacity, load duration curve (LDC) and evaluate the LOLE index. The capacity outage probability table is given in table (2).

Table 2: Capacity outage probability table of Alkhoms generating units

Capacity out of service (MW)	Probability	Cumulative probability
0	0.623144721257247	1.000000000000000
120	0.159660214366457	0.376855278742753
150	0.149954450175113	0.217195064376296

240	0.014299685339326	0.067240614201183
270	0.038420865720981	0.052940928861857
300	0.007994557339277	0.014520063140876
360	0.000516996133141	0.006525505801599
390	0.003441097035067	0.006008509668458
420	0.002048340770630	0.002567412633391
450	0.000152806235759	0.000519071862761
480	0.000006212499829	0.000366265627002
510	0.000124410699863	0.000360053127173
540	0.000183456026312	0.000235642427310
570	0.000039151541409	0.000052186400998
600	0.000000931712604	0.000013034859590
630	0.000001494984976	0.000012103146986
660	0.000006632737291	0.000010608162010
690	0.000003506538714	0.000003975424719
720	0.000000238720523	0.000000468886005
780	0.000000079702490	0.000000230165482
810	0.000000126776703	0.000000150462991
840	0.000000021380582	0.000000023686289
930	0.000000001523416	0.000000002305706
960	0.000000000773002	0.000000000782290
1080	0.000000000009289	0.000000000009289

The Libyan network load data of 2016 (8760 hours are only considered) with a peak load of 6861 MW is collected from GECOL, and since Alkhoms generating units represents 17.4% of the Libyan generating capacity, it is assumed that it is loaded by 17.4% of the Libyan hourly gross load, this assumption is considered because no specific unit in the Libyan generating system supplies a specific load but all units participate in the supply of Libyan gross load. The load model for the base case is the load duration curve of 2016 and the LOLE is evaluated in hours/year.

Figures 4, 5 and 6 show the LDC of the years 2016, 2017 and 2018 respectively.

Case 1 (Base case):

For the year of 2016, with a peak load of 1195 MW and the FOR of table (1), the LOLE is 1159 hours /year.

Case 2:

With an annual load growth of 6% [14], the peak load is 1266 MW, the LOLE of 2017 is 1893 hours /year.

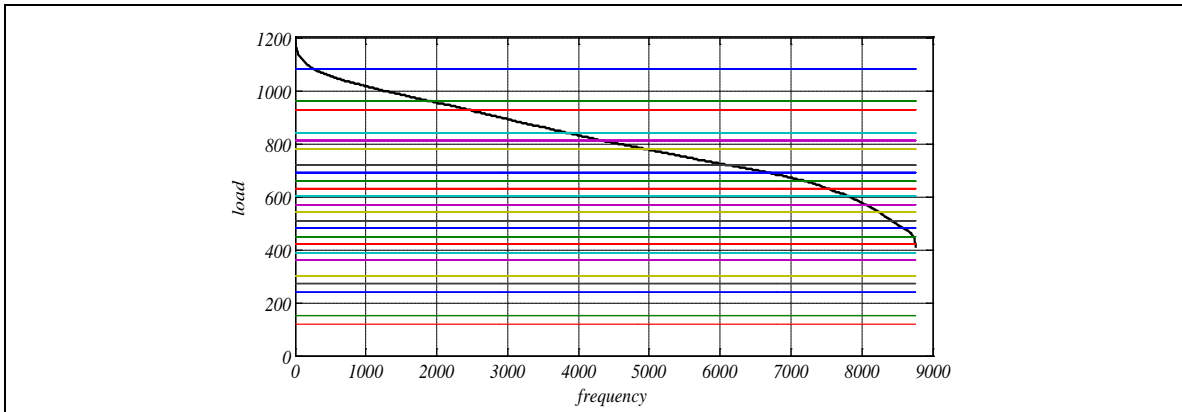


Figure 4: Load duration curve of 2016

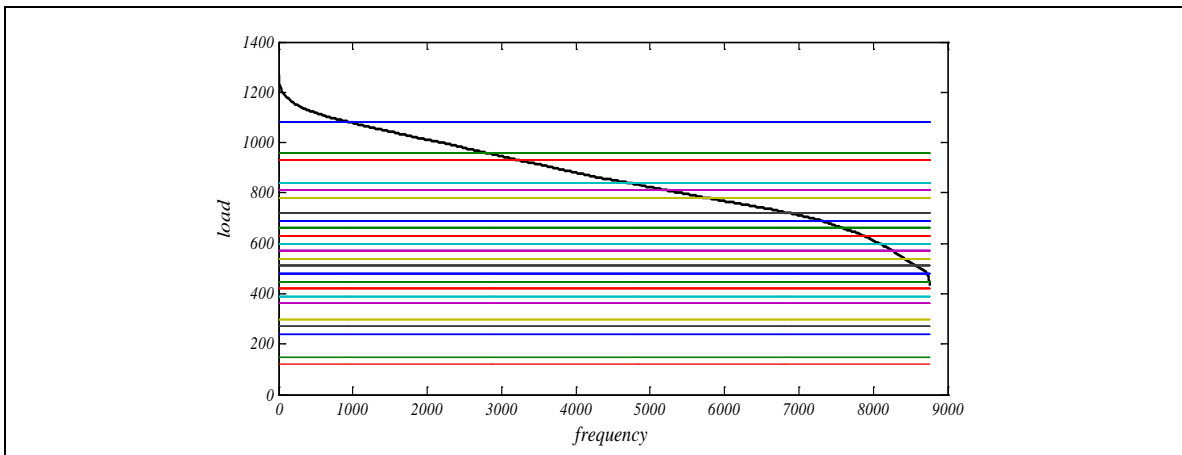


Figure 5: Load duration curve of 2017

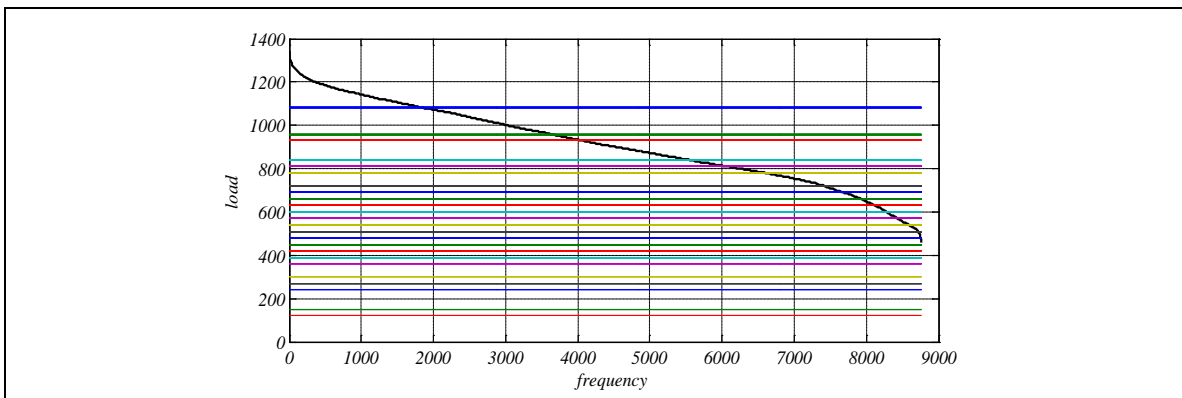


Figure 6: Load duration curve of 2018

Case 3:

With an annual load growth of 6% , the peak load is 1342.86 MW and the LOLE of 2018 is 2806 hours /year.

Case 4:

Again , for 2018 with the same assumption of case 3 , but considering a reduction of FOR of all units to 0.01,we obtain the modified COPT shown in table (3) , and the LOLE of 2018 is 2024 hrs/year.

Table 3:Capacity outage probability table of Alkhoms generating units with FOR=0.01

Capacity out of service (MW)	Probability	Cumulative probability
0	0.922744694427920	1.000000000000000
120	0.037282613916280	0.077255305572080
150	0.037282613916280	0.039972691655800
240	0.000564888089641	0.002690077739521
270	0.001506368239042	0.002125189649880
300	0.000564888089641	0.000618821410839
360	0.000003803960200	0.000053933321198
390	0.000022823761198	0.000050129360998
420	0.000022823761198	0.000027305599801
450	0.000003803960200	0.000004481838603
480	0.000000009605960	0.000000677878404
510	0.000000153695362	0.000000668272443
540	0.000000345814564	0.000000514577082
570	0.000000153695362	0.000000168762518
600	0.000000009605960	0.000000015067157
630	0.000000000388120	0.000000005461197
660	0.000000002328718	0.000000005073077
690	0.000000002328718	0.000000002744359
720	0.000000000388120	0.000000000415642
780	0.00000000005881	0.000000000027522
810	0.00000000015682	0.000000000021642
840	0.00000000005881	0.000000000005960
930	0.000000000000040	0.000000000000079
960	0.000000000000040	0.000000000000040
1080	0.000000000000000	0.000000000000000

5. Conclusions

Already it is known that the Libyan generation system has no reserve margin, its capacity is less than the present peak load, and it is unreliable. This paper presents a quantitative measure of the risk related to a part of Libyan generation system. The reliability study of Alkhoms generating system was performed using the available data from GECOL. The LOLE index is evaluated for different cases. Cases 1 and 2 showed that the load growth of 6% leads to increasing LOLE by 734 hour/year (63.33 %); whereas cases 3 and 4 showed that the reduction of FOR of all units to 0.01 reduces the LOLE by 782 hour/year (27.8 %). For all cases, it is clear that the values of LOLE are very high and violates the acceptable level, this is a direct result of the high loading considered for the units of interest (17.4 % of the Libyan gross load) and dependent on the used data imported from GECOL. To overcome this bad situation, it is recommended to complete the under construction projects of the Libyan generation system to meet the present load and the future load growth.

References

- [1]. Hagkwen Kim, Chanan Singh, "Reliability modeling and Simulation in power systems with aging characteristics", *IEEE transactions on power systems*, Vol.25, Issue 1, Feb. 2010, P: 21-28.
- [2]. Mehdi Nikzad, Shoorangiz Shams Shamsabad Farhani, Mohammad Bigadi Tahar, Hossein Tourang, Behrang Yousefpour, "Calculation of generation system reliability index : loss of load expectation", *Life Science Journal*, 2012,9, (4).
- [3]. H. Haroonabadi, M. R. Haghifam, "Loss of load expectation assessment in deregulated power system using Monte Carlo simulation and intelligent systems", *International Journal of Smart Electrical Engineering*, Article 3, Vol.01, Issue 01, Winter 2012, Page:17-25.
- [4]. C. R. Sharada Prasad, Shiddaling appa Ajjampur, Santhosh Raikar M, Prakash MN, "To study the adequacy assessment of generation system", *International Journal of advanced research in electrical, electronics and instrumentation engineering*, Vol.3, Issue 1, January 2014.
- [5]. Siti Rasheeka Muhamad Zafir, Noor Miza Muhamad Razali ,Tengku Juhana Tenngku Hashim, "Relationship between loss of load expectation and reserve margin for optimal generation planning", *Jurnalteknologi (Sciences & Engineering)*, 78:5-9 (2016) 27-33.
- [6]. Marwan M. Alturshany , Loss of load expectation for Alkhoms gas and steam units, "B.Sc graduation project 2017 ",*Faulty Of Engineering –Elmergib University*.
- [7]. Roy Billinton , Ronald N., "Reliability evaluation of engineering systems: concepts and techniques", *Plenum Publishing (New York)*, 1984 .
- [8]. R. Billinton , L . Goel, "Adequacy assessment of an overall electric power system analysis", *IEEE proceeding*, Vol.139,No.1, Jan 1992 pp 57-63 .
- [9]. Chanan Singh, "Power system reliability analysis", *Texas A,M University*.
- [10]. Jose Faernandoprada , "The value of reliability in power systems", *Massachusetts institute of technology*, Report no. EL 99- 005 WP, July 1999
- [11]. Ronald N, Allan , Roy Billinton, "Probabilistic assessment of power systems ",*Proceedings of the IEEE*,Vol.88 ,No.2 , PP 140 – 162 , February 2000
- [12]. Roy Billinton ,Ronald N, Allan, "Reliability evaluation of power systems", *Plenum publishing (New York)*, 1984 .
- [13]. *GECOL* "technical reports" 2015-2016 .
- [14]. Fathi Mohamed , Haddoud Abdulnabi Haddod , Bashir Mohamed Jumaa , "Planning of Electrical Networks in GECOL ",*Energy and Life magazine* , No.14 , September 2001.